Towards a relaxation-based MR-oximetry technique for the measurement of tumour hypoxia

Renée-Claude Lacoste Bider

Medical Physics Unit

McGill University

Montréal, Québec, Canada

July 8, 2024

A thesis presented for the degree of Masters of Science in Medical Radiation Physics

Contents

Abstract

Hypoxia, a common feature of solid tumors, is typical of aggressive cancers and leads to poorer outcomes in radiation therapy and some types of chemotherapy. Imaging tumour hypoxia would, therefore, provide medical teams with important insights to tailor treatment approaches and improve outcomes. Magnetic ressonance imaging (MRI)-based oximetry with endogenous contrast relies on the sensitivity of the R_2^* relaxation rate to changes in blood oxygenation and of the R_1 relaxation rate to changes in tissue oxygen.

To this end, our group has proposed the use of the Fat DESPOT technique, a multiparametric model that simultaneously fits R_2^*, the R_1 of fat, R_{1f}, advantageous due to the higher solubility of oxygen in fat, in addition to the R_1 of water, R_{1w} and proton density fat fraction (PDFF) to a variable flip angle, multi-echo gradient echo acquisition. In its conventional form, the Fat DESPOT model fits the magnitude of the mGRE signal. Fitting the complex signal would fully exploit the available data, potentially improving accuracy and precision while reducing acquisition time by approximately 30%.

The complex approach to Fat DESPOT (Fat DESPOT$_c$) was rigorously compared to the

conventional approach (Fat DESPOT$_m$). This was done in simulation, in a phantom with variable fat fraction, and in an in vivo measurement of the lower leg of a healthy participant. In simulations, Fat DESOT$_m$ had a higher precision and accuracy when the initial phases of the fat and water components of the signal were assumed to be the same, but was more vulnerable to fit errors compared to Fat DESPOT$_c$ when the fat and water components of the signal did not share a common initial phase. This vulnerability may have contributed to experimental results, as in phantom, Fat DESPOT$_c$ has a slightly higher goodness of fit compared to Fat DESPOT$_m$. Likewise, the accuracy of PDFF estimates compared to a reference technique, and overall precision, were slightly higher for Fat DESPOT$_c$ compared to Fat DESPOT$_m$. in vivo, both appraoches returned estimates of PDFF, R_2^*, R_{1f}, and R_{1w} that were plausible when compared to literature, though Fat DESPOT$_c$ again tended to have a slightly higher precision. Though both techniques performed well, the higher precision and accuracy of Fat DESPOT$_c$ compared to Fat DESPOT$_m$, paired with time-saving, make it a valuable asset for future work in MRI multiparametric assessment of tumour hypoxia.

Abrégé

L'hypoxie, un trait commun des tumeurs solides, est indicateur de cancers agressifs et réduit l'efficacité de la radiothérapie et certaines formes de chimiothérapie. L'imagerie de l'hypoxie tumorale fournirait aux équipes médicales des informations clés pour adapter leur approche de traitement menant à une amélioration des résultats. L'oxymétrie par l'imagerie par résonance magnétique (IRM) utilise la sensibilité du taux de relaxation R_2^* au changement d'oxygénation sanguin et du taux de relaxation R_1 au changement d'oxygénation tissulaire comme mode de contraste endogène.

Ainsi, notre groupe a proposé l'utilisation de la technique *Fat DESPOT*, qui applique un modèle multiparametrique à une séquence à échos de gradiants multiples (*mGRE*, en anglais), permettant la mesure simultanée de R_2^*, de R_1 du gras, R_{1f} (exploitant la plus grande solubilité de l'oxygène dans le gras comparé à l'eau), ainsi que le R_1 de l'eau, R_{1w} et la fraction de graisse en densité de protons (*PDFF* en anglais). Dans sa forme conventionnelle, le modèle *Fat DESPOT* utilise l'amplitude du signal *mGRE*. Toutefois, adapter le modèle au signal complexe exploiterait pleinement les données acquises et pourrait améliorer l'exactitude et la

précision des paramètres estimés tout en réduisant le temps d'acquisition par environ 30%.

Dans ce mémoire de maitrise, l'approche complexe (Fat DESPOT$_c$) a été rigoureusement comparé à l'approche conventionnelle (Fat DESPOT$_m$). Cette comparaison a été complétée en utilisant des simulations, et en effectuant des mesures dans un fantôme à fraction grasse variable et in vivo dans la jambe inférieure d'un sujet sain. En simulation, Fat DESPOT$_m$ a démontré une plus grande exactitude et précision lorsque les composantes du signal appartenant au gras et à l'eau partageaient une phase initiale commune. Toutefois, Fat DESPOT$_m$ était plus vulnérable aux erreurs lorsque ces deux composantes du signal avaient des phases initiales différentes. Ceci pourrait être un facteur dans les résultats expérimentaux. En effet, le modèle Fat DESPOT$_c$ était légèrement mieux ajusté pour les mesures dans le fantôme et produisant une mesure plus exacte et légèrement plus précise de la *PDFF* lorsqueles deux approahces ont été comparées à une technique de référence. in vivo, les deux approches ont fourni des estimés plausible de la *PDFF*, R_2^*, R_{1f} et R_{1w} lorsque comparés à la littérature. Fat DESPOT$_c$ avait encore tendance à fournir des estimés plus précis. Sur le tout, la plus haute précision et exactitude de Fat DESPOT$_c$, en comparaison avec Fat DESPOT$_m$, ainsi que les gains de temps potentiels, font de cette technique une avancée intéressante pour les futurs travaux en évaluation multiparamétrique de l'hypoxie tumorale.

Acknowledgements

First and foremost, I am grateful for Prof. Ives Levesque's guidance and mentorship from my very first day in this program and onwards, and for the supportive research group he has created. Jorge Campos, for all the help along the way, Véronique Fortier and Cristian Ciobanu for the incredible work on which this thesis is built, and Jules Faucher and Evan McNabb for their thoughtful comments and questions at every step of the way.

I am also grateful to the people who made coming to work a great part of my day. My office mates and lunch crew, Sarah, Kayla, Mélodie, Jules, Gab, Trey, Felix, and Jorge, and the other members of my first-year cohort, Maude, Maryam, Odette, and Ruby, who tolerated my chit-chat and brought levity to my day when graduate school felt daunting.

The constant support of my friends and family has allowed me to reach for the stars at every step of my personal and professional journey. I am especially grateful to Masha and Kevin, roommates who have, more than anyone, made Montréal feel like home. Janine, Tim, Pascale, je vous dois un remercîment à l'échelle de ma vie. C'est votre amour, votre sagesse, et vos encouragements qui m'ont placés ici et me permettent de poursuivre mes rêves.

I would also like to acknowledge financial support from the Research Institute of the McGill University Health Centre who awarded me a research scholarship and the Natural Sciences and Engineering Research Council of Canada (NSERC) who awarded me a Canadian Graduate Scholarship at the master's level (CGSM).

Contribution of authors

As the first author, I performed the literature review, simulations, phantom, and in vivo experiments presented in this thesis. I also performed all the presented analyses.

For simulations and analysis, I modified and expanded upon code provided by Prof. Véronique Fortier, Cristian Ciobanu, and Jorge Campos.

Throughout this project, I received guidance from Véronique Fortier, Evan McNabb, and Jorge Campos, who also assisted with phantom and in vivo experiments.

Prof. Ives Levesque provided continual guidance and advice on the work presented in this thesis and invaluable feedback on its writing.

List of Figures

List of Tables

List of Acronyms

^{1}H	Hydrogen nucleus.
Ang-2	Angiopo ıetin-2.
ATP	Adenosine triphosphate.
BOLD	Blood oxygen-level dependant.
CO_2	Carbon dioxide.
CSC	Cancer Stem Cells.
DCE MRI	Dynamic contrast-enhanced MRI.
DESPOT	Driven equilibrium single pulse observation of T_1.
EPR	Electron paramagnetic resonance.
FA	Flip angle.
Fat DESPOT$_c$	The complex approach to Fat DESPOT.
Fat DESPOT$_m$	The magnitude approach to Fat DESPOT.
FID	Free induction decay.
FOV	Field of view.

GC	Graph cut.
GRE	Gradient Echo.
Hb	oxy-hemoglobin.
HBO2	hemoglobin.
HIF	Hypoxia-Inductible Factors.
IDEAL	Iterative decomposition of water and fat with echo asymmetry and least-squares estimation.
IR	Inversion Recovery.
LL	Locker Locker.
MEGRE	Multiple Echo Gradient Echo.
MOBILE	Mapping oxygen by imaging lipids relaxation enhancement.
MRI	Magnetic Resonance Imaging.
MS TSE	Multi slice turbo spin echo.
NIR	Near-infrared spectroscopy.
NSA	Number of signal averages.
O_2	Oxygen.
OE	Oxygen enhanced.
PAT	Photoacoustic tomography.
PDFF	Proton Density Fat Fraction.
PE	Phase encode.

PET	Positron Emission Tomography.
pO_2	partial oxygen pressure.
RF	Radio frequency.
RO	Read out.
SNR	Signal to noise ratio.
SPECT	Single-photon emission computed tomography.
TE	Echo time.
TOLD	Tissue oxygen-level dependant.
TR	Repetition time.
VFA	Variable Flip Angle.
VGEF-a	Vascular endothelial growth factor-A.

Chapter 1

Introduction

1.1 Motivation

Hypoxia, an insufficient oxygen supply to tissues, is a prevalent feature in several diseases, impacting prognosis and treatment. Indeed, hypoxia plays a role in diseases such as fatty liver disease [6, 7], diabetes [8], and solid cancers [9] and can lead to various effects including inflammation, fibrosis, and, in severe cases, necrosis [9]. Hypoxia has been correlated with poor treatment outcomes in several solid tumors including head and neck cancers, prostate cancer, liver metastases, and breast cancer [9, 10]. This is likely in part due to changes to gene expression and immune response mediated by hypoxia-inducible factors (HIF), which results in more aggressive cancer phenotypes [9, 11]. Furthermore, oxygen plays a key role in preventing damage repair in radiation therapy and some types of chemotherapies. As such,

hypoxia reduces the efficacy of these treatments [12]. Imaging of hypoxia could, therefore, allow for treatments to be tailored in the hopes of improving patient outcomes.

Several approaches have been proposed for hypoxia measurement in tumors, though their limitations are significant. The polarographic electrode probe is considered a gold standard for oximetry, but is highly invasive and only offers point measurements [13]. Imaging techniques, like Positron emission tomography (PET) and Single-photon emission computed tomography (SPECT), require ionizing radiation and have low resolution [10, 14]. In MRI, blood oxygen level-dependent (BOLD) measurements rely on oxygen-induced changes in the R_2^* relaxation rate of blood [15] and tissue oxygen level-dependent (TOLD) measurements rely on the oxygen-induced change in the R_1 relaxation rate of tissue [16] to produce endogenous, non-invasive contrast [17–20]. However, R_2^* is an indirect measure of tissue oxygen and is affected by other factors such as blood flow and volume changes [21], while R_1 measurements of change in oxygen are often challenged by low sensitivity [22]. The measure of a fat-only R_1, R_{1f}, has been proposed to mitigate this low sensitivity, as oxygen is significantly more soluble in fat than in water, but techniques used to achieve this rely on suppressing the water signal [23] or simplifying the fat MR spectrum. [24]. Hence, our group has proposed using the Fat separated Driven equilibrium single pulse observation of T_1 (Fat DESPOT) to measure hypoxia in tumours [25].

In addition to R_{1f}, Fat DESPOT models the magnitude of a multi-echo gradient echo (mGRE) acquisition to estimate the R_1 of water, R_{1w}, R_2^* and proton density fat fraction

(PDFF) [25, 26]. This would allow for simultaneous observation of oxygenation in blood and tissue and preserve the ability to use R_{1w} in low-fat environments. However, in the conventional approach, the Fat DESPOT model is fit to the magnitude of the mGRE signal, only using part of the available data. Our group has previously suggested incorporating the complex signal into the Fat DESPOT model, fully exploiting the signal data. This would reduce the echo requirements for fitting, driving down acquisition times and potentially increasing accuracy and precision. While this approach proved advantageous in simulations, this did not hold in retrospective data studies and it has yet to be tested in prospective experiments [3]. Hence, open questions as to the validity and resistance to experimental factors such as field inhomogeneities of the complex approach remain.

1.2 Objectives

First, this thesis aimed to further develop the Fat DESPOT technique, reevaluating the Fat DESPOT workflow and complex model. For both approaches to fat DESPOT, the algorithms used to provide initial guesses to the Fat DESPOT model were modified to improve fitting. The complex Fat DESPOT model was also expanded to include separate initial phase estimates for fat and water and Flip-angle specific estimations of the B_0 field.

This thesis is focused on its second objective: a rigorous comparison of the complex and magnitude approaches to Fat DESPOT. Approaches were first compared in simulation, assessing the respective resistance of the complex and magnitude approaches to phase

differences in fat and water. A variable fat fraction phantom was used to compare models experimentally over a wide range of fat fractions. Finally, an in vivo pilot measurement was conducted to compare approaches to compare the performance of both techniques in human tissue. This work aimed not only to compare techniques for precision and accuracy but also to determine the feasibility of the Fat DESPOT approach for tumour MR oximetry, to guide the approach of this group and others in the field of MR oximetry.

1.3 Thesis outline

Chapter 2 provides context and background information relevant to this thesis. This includes an overview of vasculature, hypoxia, and existing techniques for hypoxia imaging, a review of the fundamentals of MRI, and the state of the science of the Fat DESPOT technique. Chapter 3 of this thesis contains an original manuscript comparing the magnitude and complex approaches to Fat DESPOT in simulations, phantom, and in vivo. This manuscript builds on previous work by our group [3, 25], and includes technique advancements and experiments conducted throughout this project. Chapter 3 contains a scholarly discussion of the work presented in this thesis in relation to imaging tumour hypoxia. Chapter 4, contains a summary of the work presented and outlines future work. Finally, Chapter 6 contains appendices offering supplemental information on work mentioned in this thesis including phantom construction, the evolution of the complex approach to Fat DESPOT, and additional work in accelerating Fat DESPOT acquisitions.

Chapter 2

Background

2.1 Vasculature, perfusion, and hypoxia

Hypoxia plays an important role in many diseases, including fatty liver disease, diabetes, and solid cancers [8, 27–30]. In this section, the underlying principles of tissue oxygenation, hypoxia, and the effects of hypoxia in disease will be explored, with an emphasis on its role in solid tumour outcomes and treatment.

2.1.1 Healthy vasculature

The cardiovascular system ensures that organs receive the necessary metabolites and nutrients for proper function while eliminating waste products and toxins. This complex system comprises various organs, such as the heart, arteries, capillaries, and veins. The

heart plays a central role in ensuring oxygenation and circulation by pumping deoxygenated blood from the body through the pulmonary artery to be reoxygenated in the lungs and propelling the oxygen-rich blood into the aorta. The aorta branches into smaller arteries and arterioles, distributing oxygenated blood through the body [31]. These blood vessels have a thick layer of smooth muscle and are elastic, allowing them to withstand high pressures [31]. The exchange of metabolites between the blood and tissues occurs in the capillaries, small, single-cell walled vessels. Small, water-soluble compounds such as salts and glucose can diffuse through pores in the vessel wall, while lipid-soluble compounds, such as oxygen, diffuse directly through the lipid bi-layer of the capillary cells [32]. Following the capillaries, the blood collects in larger veins. Subject to lower blood pressure than the arteries, veins have a thinner muscle wall and unidirectional valves to prevent backflow as the blood is pumped back towards the heart [31].

Due to its relatively low solubility in water, 98% of oxygen contained in blood is found in the red blood cells (RBCs), where it is associated with the hemoglobin protein (Hb) [33]. This protein consists of two α and two β units, each of which is bound to a heme molecule coordinated with a ferrous iron. When in the oxygen-favourable relaxed (R) state, the ferrous iron atoms can bind with an O_2 molecule, allowing each Hb to transport up to four O_2 molecules. Conversely, in the (T) tense state, the Hb has a low affinity for oxygen and remains in its deoxygenated form [1]. At a given oxygen partial oxygen (pO_2), typically reported in mmHg, the deoxygenated form of Hb, deoxyhemoglobin, and its oxygenated

form, oxyhemoglobin (HbO_2) establish an equilibrium. At high pO_2s, such as in the lungs, the oxygen saturation of Hb is near 100%. However, as the blood travels away from the lungs and through the body, pO_2 drops, oxygen dissociates from Hb and diffuses into the surrounding tissue [33]. The oxygen equilibrium curve of Hb can represent this behaviour, shown in Figure 2.1 along with the structure of the Hb molecule. The stability of the T and R formes of Hb can be affected by several factors including pH, temperature, and partial pressure of carbon dioxide (pCO_2). This can result in a left or right shift of the equilibrium curve [1].

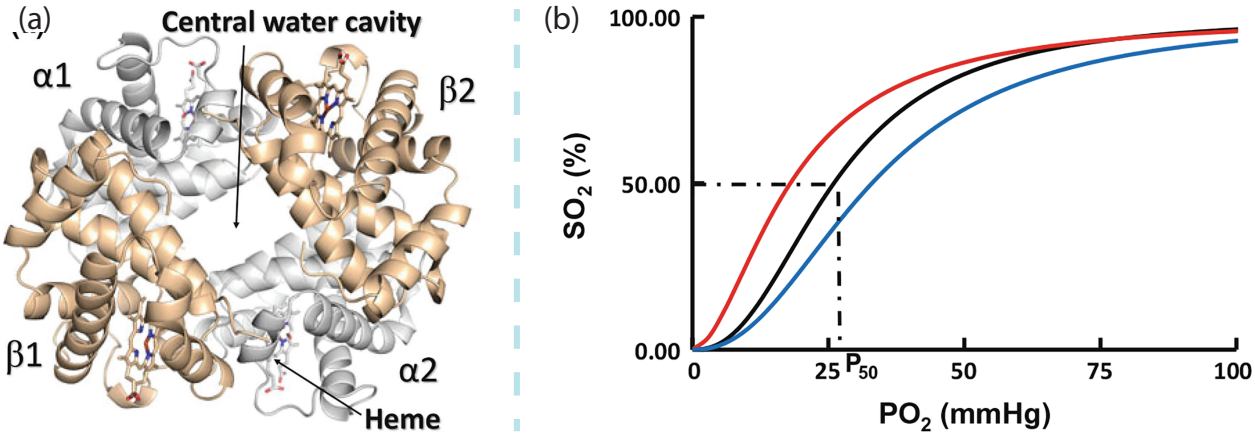

Figure 2.1: Images from Ahmed *et al.* depicting (a) The structure of the hemoglobin (Hb) molecule consists of two α and two β units arranged around a central water cavity. Each unit is bound to a heme, which centers around a ferrous iron that binds with oxygen. (b) The oxygen equilibrium curve of Hb shows the change in Hb oxygen saturation (SO_2) as a function of partial oxygen pressure reflecting its changing affinity to O_2. This curve can be left-shifted (red) or right-shifted (blue) due to pH, pCO_2 or other factors [1].

The circulatory system must meet the metabolic needs of organs and tissues. Organs

are connected in parallel, such that they receive equal metabolite concentrations and that perfusion, or the passage of blood through their vasculature, can be independently controlled. The metabolic exchange rate between a tissue or organ and the bloodstream is determined by the vascular resistance, which is related to the size of the vascular lumen in that particular organ or tissue [32]. Hence blood flow is regulated through vasodilation and vasoconstriction to meet metabolic demand [31]. Vasodilation and constriction also increase and decrease the number of anatomically present capillaries [32].

2.1.2 Hypoxia and disease

Hypoxia can alter cellular metabolism and gene expression and, in cases of prolonged or extreme oxygen deprivation, will cause cellular death. Hypoxia has a bidirectional relationship with chronic inflammation, fibrosis, and angiogenesis [27] and is a common trait of several diseases, including fibrogenic liver disease [27], diabetes [8, 30], kidney disease [28] Alzheimer's disease [29], and solid tumours [9–11]. Indeed, hypoxic cells upregulate the production of Hypoxia-inducible factors HIF-1α and HIF-2α, which trigger immune and cellular responses including further angiogenesis and inflammation [8]. In some diseases such as diabetes, the HIF response is impaired, leading to cellular dysregulation and disease exacerbation [8]. In solid tumours, hypoxia negatively affects cancer progression, treatment outcomes, and prognosis [9].

2.1.3 Anatomy and physiology of tumour hypoxia

While existing vasculature may initially sustain the growing tumour, its high cellular proliferation, and metabolic activity requires additional blood flow [34, 35]. Tumour angiogenesis is thought to be triggered by the upregulation of HIF and subsequent synthesis of hormones such as vascular endothelial growth factor-A (VEGF-A) and angiopoïetin-2 (Ang-2) [36]. In the first step of angiogenesis, abnormally thin, wide, and highly porous "mother vessels" form. They then differentiate into capillaries, glomeruloid microvascular proliferations, disorganized vessel structures with an appearance similar to that of renal glomeruli, and vascular malformations, abnormally large vascular structures stabilized by a thin and irregular layer of smooth muscle [37]. In parallel, host arteries become abnormally thin, dilate, and lose vasomotion, the ability to contract.

Where normally oxygenated subcutaneous tissue has oxygen pressure of between 40 and 60 mmHg, tumours have, on average, much lower oxygen pressure at 10 mmHg, reflecting the presence of hypoxia [12]. Tumour hypoxia is categorized by its cause and the effect on cells [34]. Chronic, or diffusion-limited hypoxia is the result of the heterogeneous distribution of tumour vasculature, resulting in areas of under-perfused tissue. Acute, or perfusion-driven hypoxia stems from structural and functional changes in vasculature such irregular branching, tortuosity, and wide lumens, leading to transient changes in perfusion and limiting the exchange of gases and nutrients [9, 34, 37]. In other areas the geometry or size of vessels permits the flow of plasma but not of cells, resulting in what is known as partial or hypoxemic

hypoxia. Here, hypoxia quickly becomes severe as only the cells at the start of such vessels receive any oxygen [9, 34].

2.1.4 Tumour hypoxia and treatment outcomes

Hypoxia is a biomarker for tumour progression, poorer treatment outcomes, and prognoses in various solid tumours. Indeed, hypoxia is a marker of locally advanced solid tumours for over 15 cancer types including cancers of the breast, uterus, cervix, head and neck, prostate, pancreas, and metastatic liver tumours [9] . Hypoxia and the expression of hypoxia-related proteins such as HIF, is also related to adverse outcomes, poorer survival, and poorer local tumour control in various cancer types, such as head and neck, breast, and ovarian cancers [9].

While anoxia, severe hypoxia, triggers immediate cellular arrest or apoptosis leading to areas of necrosis, HIF expression in mild and chronic hypoxic volumes regulates over 70 known genes, including genes for erythropoisesis, angiogenesis, glycolysis, proliferation, cell survival, and apoptosis [38]. These changes in the cell's genomic and proteomic expression often result in more aggressive or resistant phenotypes [9, 11].

Hypoxia affects tumour response to chemotherapy due to both structural limitations to drug delivery and the interaction of chemotherapy compounds with hypoxic cells. First, just as diffusive and perfusive hypoxia limit the delivery of oxygen and nutrients to tissue, poor tumour perfusion limits the dose of chemotherapy compounds delivered to targeted cells [12]. Second, H1F-induced changes to gene and protein expression also affect the efficacy of some

types of chemotherapy [39]. For example, while some chemotherapy compounds target the expression of p53, a protein regulating cell division, hypoxic tumours are often resistant to p53-induced apoptosis [12].

Hypoxia also reduces the efficacy of radiation therapy, which relies on free-radical-induced DNA damage. Free radicals are produced when high-energy photons, electrons, or, in some emerging treatments, protons, interact directly with DNA strands or ionize water molecules in the nucleus of the cell. Unstable hydrogen free radicals then interact with DNA, breaking the strand. In normoxic cells, oxygen fixes the free radical to the DNA and prevents repair. However, in hypoxic cells, free radicals can be removed by scavenger proteins, allowing for repair to occur and reducing net damage [9, 12, 34]. While both acute and chronic hypoxic tumour volumes experience a lower rate oxygen fixation, nutrient deficiencies may impact the repair ability of tumour cells. Acutely hypoxic areas, however, experience a temporary reduction in radiation damage fixation and benefit from sufficient nutrient availability to repair the damage, making these areas particularly resistant to radiation therapy [34].

2.2 Approaches to in vivo hypoxia imaging

The ability to image hypoxia as part of a typical clinical workflow would provide medical teams with important prognostic information, allow for compound-based therapies to be tailored to the hypoxic tumour environment, and allow for radiation treatments to be tailored to the distribution of hypoxia in the tumour volume [11, 34]. The ideal measurement of

hypoxia should be non-invasive, reproducible, cost-efficient [14], rapid, measures the tumour tissue oxygen directly, and sensitive to a range of hypoxia levels. However, current hypoxia measurement techniques fall short of these requirements and have failed to be integrated into the clinical workflow.

Several non-imaging methods for hypoxia measurement have emerged. Polarographic electrode probes are considered the gold standard for oximetry and have been used to measure hypoxia in tumours for over two decades [13]. Though these probes provide a direct measurement of tumour tissue oxygen, this method is highly invasive and delivers point measurements of pO_2, making it difficult to determine the distribution of hypoxia in the tumour [10]. Phosphorescence quenching, electron paramagnetic resonance (EPR) oximetry, and ^{19}F-magnetic resonance spectroscopy follow a similar principle, measuring oxygen-induced changes in the spin-lattice relaxation rate of a probe inserted in the tumour, offer direct measurements of pO_2 but invasively and with little to no spatial information [11].

Near-infrared spectroscopy (NIRS) and photoacoustic tomography (PAT) offer non-invasive alternatives to these techniques, both based on the different photon absorption spectra of hemoglobine and deoxyhemoglobine. However these techniques probe blood oxygen, offering an indirect measure of tissue hypoxia. Additionally, NIRS has limited tissue penetration and sensitivity. Conversely, photoacousic tomography has high tissue penetration and resolution, but a narrow field of view [10, 11].

Exogenous contrast-based imaging techniques have also been harnessed for tumour oxygen quantification. Notably, PET with contrast agents such as F18-EF5 and SPECT with contrast agents such as I123-IAZA can track tumour oxygen consumption. However, PET compounds for oxygen tracking have a low yield and resolution, while SPECT compounds for this purpose are unstable, have a slow clearance, and a high background signal [10, 40].

Various contrast-based MRI techniques offer a non-radiation-based alternative to imaging hypoxia. These approaches include ^{19}F MRI (using perfluorocarbons (PFCs) and fluorinated nitroimidazoles contrast agents), Overhauser-enhanced MRI (OMRI), and DCE-MRI. However, in addition to involving the use of an injectable contrast agent, these MRI techniques have several limitations. ^{19}F MRI, is highly sensitive to flow artifacts, temperature, dilution, pH, and blood proteins, making it challenging to reliably implement [10, 11], OMRI suffers from low resolution and high cost [40, 41], and DCE MRI measures tissue oxygenation indirectly via perfusion, and has low resolution [11, 40].

BOLD and TOLD -based MRI techniques with endogenous contrast have also emerged for tumour hypoxia mapping. These techniques rely on the change in R2* of blood and R_1 of tissue in response to an oxygen challenge to identify hypoxic tumour volumes [18, 21] and will be described in greater detail in section 2.3.5.

It should be noted, that in addition to having significant drawbacks, current hypoxia measurement technique are rarely used clinically in the cancer treatment workflow [41, 42].

This could be due to implementation challenges such as a lack of personnel with the expertise to run these exams and time constraints, emphasizing the importance of a rapid, easily implemented technique that easily integrates into current treatment planning protocols.

2.3 MRI oximetry

MRI has emerged as a powerful imaging technique for anatomic and functional imaging of soft tissue. This modality has numerous advantages; high soft tissue contrast, non-reliance on ionizing radiation, and high spatial resolution. This section delves into the fundamental concepts of MRI and current MRI applications for endogenous contrast of tumour hypoxia.

2.3.1 Nuclear magnetic resonance and excitation

In quantum mechanics, spin ($\vec{s}$) describes the intrinsic angular momentum of subatomic particles. Baryons, such as protons, neutrons, and electrons have a spin 1/2. In the nucleus, protons and neutrons will arrange themselves such that net spin is minimized. It follows that nuclei with odd mass numbers have a net half-integer spin. Though spin mechanics are explained by quantum physics, they can also be approached through a classical mechanics lens where the nucleus is considered as a charged sphere spinning on itself, resulting in a magnetic moment, $\vec{\mu}$, and angular momentum, $\vec{L}$, related to each other through the gyromagnetic ratio, γ, as seen in equation 2.1 [43, 44]. γ is a quantity specific to the nuclei. For the hydrogen nucleus H_1, it is equal to $267.5 \times 10^6 rad/s \cdot T$ [45].

$$\gamma = \frac{\vec{\mu}}{\vec{L}} \tag{2.1}$$

When placed in an external magnetic field, $\vec{B}$, generally measured in tesla (T), the nuclear magnetic moment experiences a torque, $\vec{T}$, corresponding to equation 2.2 [44].

$$\vec{T} = \vec{\mu} \times \vec{B} \tag{2.2}$$

Given the relationship between $\vec{\mu}$ and $\vec{L}$, this results in a rate of change of $d\vec{\mu}/dt$ corresponding to equation 2.3 and an angular velocity given by equation 2.4. This is the Larmor frequency, ω_0 the precession or resonance frequency of a nucleus in a given magnetic field, as represented in Figure 2.2 [43, 44].

$$\frac{d\vec{\mu}}{dt} = m\vec{u} \times \gamma\vec{B} \tag{2.3}$$

$$\vec{\omega_0} = \gamma\vec{B} \tag{2.4}$$

The interaction between the magnetic moment and external magnetic field is the basis for nuclear magnetic resonance (NMR) and magnetic resonance imaging (MRI). In MRI, the nucleus most often of interest is the hydrogen nucleus, a single proton with spin 1/2, due to its being nearly ubiquitous in living organisms, notably present in water molecules, proteins,

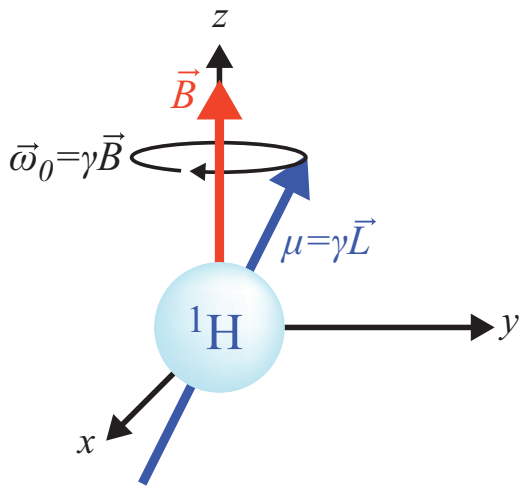

Figure 2.2: The ^{1}H nucleus has a magnetic moment, $\vec{\mu}$, resulting from its non-zero spin and electric charge. In an external magnetic field, $\vec{\mu}$ precesses at the Larmor frequency, $\vec{\omega_0}$ in the left-hand direction.

and triglycerides. X-nuclei MRI interest itself in imaging other nuclei with non-zero spin with magnetic moments such as ^{35}Cl, ^{17}O, and ^{23}Na [46].

In the absence of a magnetic field, the magnetic moments of hydrogen atoms are randomly oriented. However, when placed in an external magnetic field, B_0, quantum mechanics dictate that the potential energy of the magnetic moment is quantized in one of two states: a ground state, $E_+ = -\gamma\hbar B_0/2$, parallel to $\vec{B_0}$, or an antiparallel excited state, $E_- = \gamma\hbar B_0/2$. For an ensemble of spins, the ratio between the number of nuclei in the ground state, N_+, and the excited state N_- is described by Boltzmann statistics, as seen in equation 2.5, where T is temperature and $\hbar$ is Plank's constant over by 2π, k is Boltzman's constant [43, 44].

$$\frac{N_+}{N_-} = \frac{e^{E_+/kT}}{E_-/kT} = e^{-\gamma\hbar B_0/kT} \tag{2.5}$$

While the ratio between states will change with temperature, the number of nuclei in the excited state will never outnumber the number of nuclei in the ground state. Hence, the net magnetization, $\vec{M}$, will always be parallel to $\vec{B_0}$. When $\hbar\omega_0 << kT$, the approximative net magnetization is given by equation 2.6 [43, 44]. By convention, $\vec{B_0}$ is always oriented in the z dimension.

$$\vec{M_0} \approx \rho_0 \frac{s(s+1)\gamma^2\hbar^2}{3kT}\vec{B_0} \tag{2.6}$$

Excitation describes tilting the net magnetization away from the $\vec{B_0}$, by applying a second, smaller field B_1 through an RF pulse, delivered by RF coils, at the Larmor frequency. This effectively applies a torque to the magnetic moment of the hydrogen protons with the rate of change equal to equation 2.7. The angle of the net magnetization relative to $\vec{B_0}$ is dictated by the intensity and length of the B_1 field [43, 44].

$$\frac{d\vec{M}}{dt} = \gamma\vec{M} \times \vec{B_1} \tag{2.7}$$

As previously discussed, the resulting net magnetization will precess around $\vec{B_0}$ and have a transverse and longitudinal component. Following the B_1 excitation pulse, this net magnetic moment will return to its equilibrium state, in a process called relaxation. Free induction

decay (FID) is relaxation without the additional application of fields. The relaxation rate depends on interactions specific to the nuclear environment and changes from tissue to tissue. Just as an RF pulse induces a precession in the proton magnetic moments during excitation, the proton's precession during relaxation induces an RF current in a second set of receive coils during relaxation, also at the Larmor frequency. The resulting signal is then spatially encoded and used to construct MR images [43, 44]. As such, relaxation is at the basis of MRI contrast. Two types of relaxation are considered, Longitudinal, or spin-lattice, and transverse, or spin-spin relaxation [43, 44].

Longitudinal relaxation describes the return of the net magnetization along the z dimension (M_z) due to transitions between spin energy levels and is described by equation 2.8, where T_1 is the longitudinal relaxation time, corresponding to the time at which 63% of the M_z magnetization is recovered, and t is time [43, 44].

$$M_{z'}(t) = M^0_{z'}(1 - e^{-t/T_1}) + M_{z'}(0_+)e^{-t/T_1} \tag{2.8}$$

Transverse, or spin-spin relaxation describes the loss of the net magnetization in the transverse plane (M_{xy}) due to the loss of phase coherence of individual hydrogen atoms and is described by equation 2.9, where T_2 is the transverse relaxation time, corresponding to the time at which 63% of the M_{xy} magnetization is lost [43, 44].

$$M_{x'y'}(t) = M_{x'y'}(0_+)e^{-t/T_2} \tag{2.9}$$

Loss of phase coherence, or nuclei de-phasing due to interactions between neighbouring magnetic moments and random fluctuations in the transverse component of the magnetic field is responsible for the T_2 relaxation time. These fluctuations in the B_0 field can also cause energy level transitions, contributing to T_1. Effects from additional fluctuations in the B_0 field are due to imperfections in the NMR instrument, variations in the properties of the sample, and the chemical environment of the sample, such as the presence of electrons from metal ions are encompassed by T_2'. The total relaxation time, T_2^* is given by a combination of the "pure" T_2 and T_2', as shown in equation 2.10. T_2^* is always shorter than T_2. While T_2' effects are constant over time, such that they can be reversed, T_2 effects are not [43, 44].

$$\frac{1}{T_2^*} = \frac{1}{T_2} + \frac{1}{T_2'} \tag{2.10}$$

Relaxation can also be described with relaxation rates R_1, R_2 and R_2^*, relating to T_1, T_2 and T_2^* through equation 2.11. Relaxation rate and relaxation time are often used interchangeably.

$$R_1 = \frac{1}{T_1}, R_2 = \frac{1}{T_2}, R_2^* = \frac{1}{T_2^*} \tag{2.11}$$

2.3.2 Basic pulse sequences

While the FID is the result of precession paired with T_1 and T_2^* relaxation, RF pulses can be combined in various pulse sequences to allow for the differentiation of T_1, T_2, and T_2^*

decays [43].

The spin echo sequence, described in Figure 2.3 involves a 90° FA pulse, placing the macroscopic magnetic moment entirely in the transverse plane. Subsequently ^{1}H protons precess at slightly different frequencies and begin dephasing as per T_2^* decay. At time TE/2, a second pulse with a 180° FA is applied, flipping each magnetic moment into its opposite quadrant and inverting the M_z signal component. Effectively, faster-precessing protons are now "behind" in their precession compared to slower-moving protons. Since T_2' effects are constant over time, this creates a refocusing of the ^{1}H magnetic moments at the echo time TE, called an echo. Furthermore, TE corresponds to the time at which the magnetization crosses 0 in the z direction, putting $\vec{M}$ entirely in the xy plane. However, T_2 effects are inconsistent over time and cannot be recovered. Hence the signal reduction at time TE can be entirely attributed to T_2 through equation 2.12 and 2.13, where M_{xy0} and S_0 are the magnetization and signal immediately following excitation [47].

$$M_{xy,SE}(t) = M_{xy0}e^{-t/T_2} \tag{2.12}$$

$$S_{xy,SE}(t) = S_{xy0}e^{-t/T_2} \tag{2.13}$$

Saturation recovery is a simple sequence to measure T_1 or T_2^*. In this sequence, a 90° RF pulse is used to tilt $\vec{M}$ into the transverse plane. After a recovery time TR, the following 90°

RF pulse is applied to the system. The resulting M_{xy} and MR signal are given by equations 2.14 and 2.15 respectively, provided TR is long enough for transverse magnetization to decay to 0, as described by e^{-t/T_2*} [43].

$$M_{xy,SR}(t) = M_{xy0}(1 - e^{-TR/T_1})e^{-t/T_2*} \tag{2.14}$$

$$S_{xy,SR}(t) = S_{xy0}(1 - e^{-TR/T_1})e^{-t/T_2*} \tag{2.15}$$

T_1 can therefore be measured by repeating this sequence while maintaining the same measurement time, t, and modulating TR, While T_2^* measurements are obtained by measuring the signal at different measurement times with a fixed TR.

2.3.3 Signal localisation

To achieve an MR-based image, the MRI signal must be localized in space. This is done by establishing a relationship between spatial coordinates and signal frequency, in the Fourier domain, commonly referred to as k-space. To establish this relationship, magnetic gradient fields, generated by gradient coils, are applied to the volume of interest [43, 44].

A gradient field applied during or following an excitation linearly modulates the B0 field along a given axis. This establishes a relationship between spatial position along this axis, Larmor frequency during the gradient pulse, and dephasing of the signal relative to

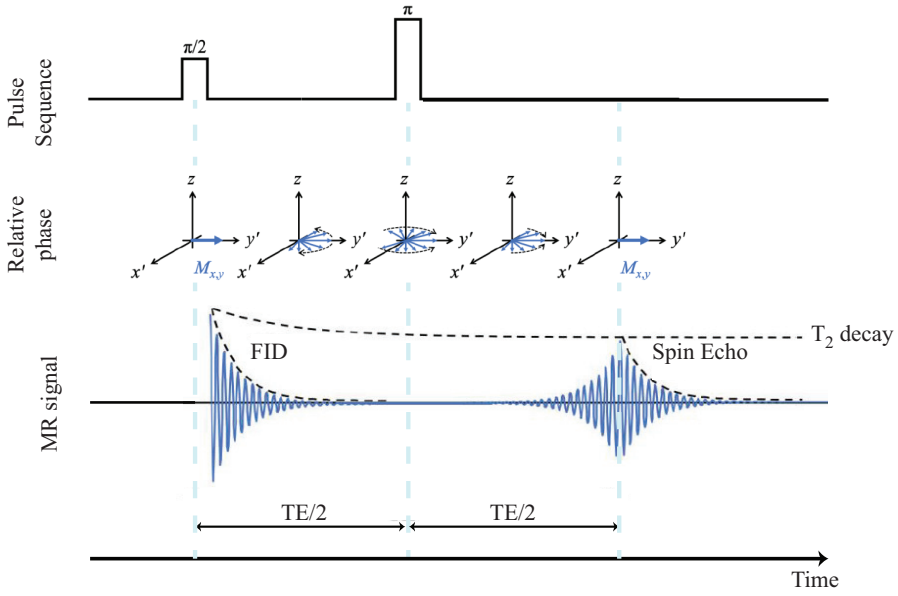

Figure 2.3: A schematic representation of the spin echo pulse sequence, its effect on relative phase, and the MR signal. Figure adapted with permission [2]

a reference phase ϕ_0 following the gradient pulse, described by equations 2.17 and 2.16 respectively for the case of a gradient along the z-axis, G_z, turned on for a time T_{PE}. In the simplest cases, gradients are used to perform slice selection, frequency, and phase encoding [43, 44].

In slice selection, a gradient is applied during the excitation, modulating the Larmor frequency such that only a slice of the volume has a Larmor frequency within the bandwidth of the excitation pulse. This effectively results in the excitation of a slice of the volume of interest and simplifies the imaging problem from a 3D problem to a 2D problem. However, the phase shift induced by the slice-selective gradient also results in signal loss. To mitigate this, a post-excitation rephasing gradient must be applied to the system [43, 44].

$$\omega(z) = \omega_0 + \gamma G_z z \tag{2.16}$$

$$\phi(z) = -\gamma G_z z T_{PE} \tag{2.17}$$

Applying a gradient along a given axis also establishes a relationship between the time integral of the gradient and the frequency coordinate in k-space and the MRI signal. A gradient along a given axis, a, can be seen as moving the sampling point in k-space in the k_a direction, and the distance traveled in k-space is proportional to the strength and duration of the applied gradient. Phase and frequency encoding are used to trace sampling trajectories in k-space [43, 44].

A simple example of frequency and phase encoding consists of exploring k-space in a Cartesian grid trajectory. Frequency encoding is conducted in the read-out (RO) direction. In this case, following excitation and before the signal readout a first gradient, -G_{RO}, is applied. Effectively linearly dephasing the macroscopic magnetic moment along the RO direction and moving in K-space along in the -k_{RO} axis. A second gradient, G_{RO}, is then applied during readout. This selectively rephases the macroscopic magnetic moment along the RO axis, creating an echo, or moves the MR signal back in the k_{RO} direction. For a monopolar acquisition, the pulse sequence is designed so that the signal is only collected during the positive lobe of the G_{RO} while bipolar acquisitions are designed to collect signals

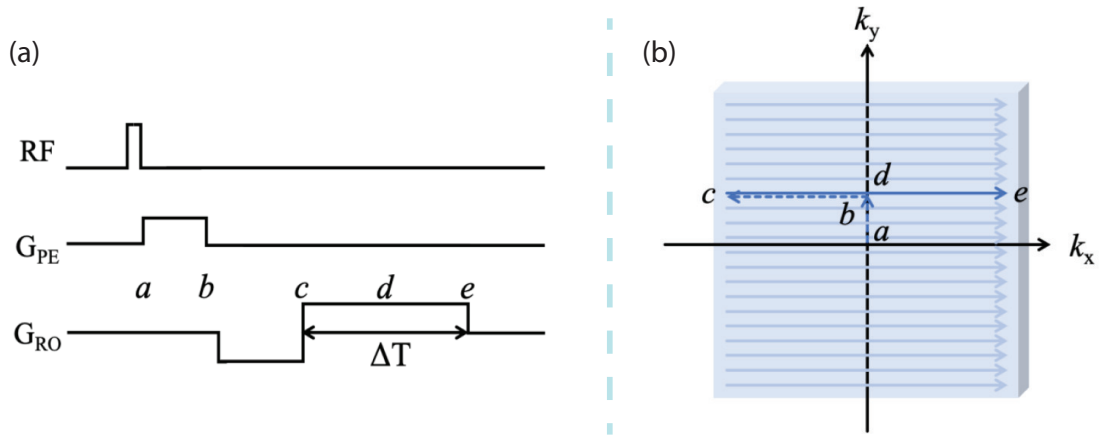

Figure 2.4: (a) A pulse sequence imaging a single line of k-space in a cartesian grid and (b) resulting k-space trajectory. Figure adapted with permission [2]

in both the positive and negative lobe are collected for a bipolar acquisition [43, 44].

To achieve 2-D imaging, a second Gradient, is applied before readout in the Phase-encode (PE) direction, orthogonally to G_{RO}, allowing the MR signal to move in k-space along the k_{PE} direction. Consequentially, During readout, a single line through k-space is measured. A schematic of this frequency and phase encoding process for a case in which the RO direction is in x and the phase-encode direction is in y can be seen in Figure 2.4. These gradient encoding steps must be repeated at time intervals TR, with varying strengths of G_{PE} such that all of k-space is sampled. It follows that the number of TR repetitions corresponds to the number of voxels in the PE direction. Likewise, the number of signal samples taken at each TR corresponds to the number of voxels in the RO direction. This is demonstrated in Figure 2.5 [44].

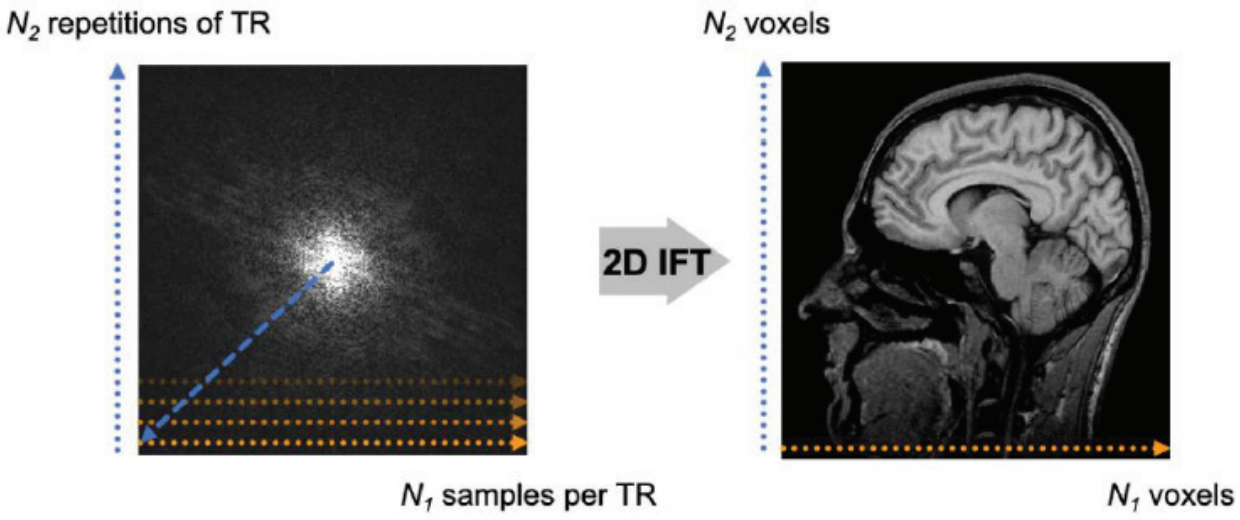

Figure 2.5: The relationship between k-space sampling and the resulting voxelized image. Figure reproduced with permission [2]

The relationship between k-space and image-space dictates that the sampling intervals are inversely proportional to the field of view in the RO and PE directions, while the voxel size is inversely proportional to the coverage of k-space [44]. As an alternative to slice selection in 3D MRI, an additional phase-encoding step can be completed in the remaining dimension of k-space. Furthermore, in addition to cartesian sampling, other k-space trajectories, such as radial or spiral readouts, can be used to explore k-space [48].

The spoiled multi echo gradient echo (mGRE) technique, showed in Figure 2.6 is highly relevant to this thesis. It combines multiple repeat RF excitations, each followed by multiple gradient echoes. Between excitations and following readout, RF spoiling is used to eliminate remaining magnetization. The resulting signal can be modeled by equation 2.18 and sequence

parameters can be adjusted to create different contrasts [49]. For example, the variable flip angle (VFA) approach to T_1 mapping keeps TR and TE constant and measures the signal with n≥2 FAs taken in successive acquisitions. The signal equation can then be rearranged into equation 2.19 and fit with a non-linear least-squared approach [50]. Conversely, a T_2^* fitting can be achieved by using a single TR, and FA while measuring the signal at several TEs [51].

$$S(TR, TE, \theta) = S_0 \left[\frac{(1 - e^{-R_{1f} TR}) sin(\theta_n)}{1 - e^{-R_{1f} TR} cos(\theta_n)} \right] e^{-R_{2*} TE} \tag{2.18}$$

$$\frac{S_n}{sin(\theta_n)} = \frac{S_n}{tan(\theta_n} e^{-TR/T1} + constant \tag{2.19}$$

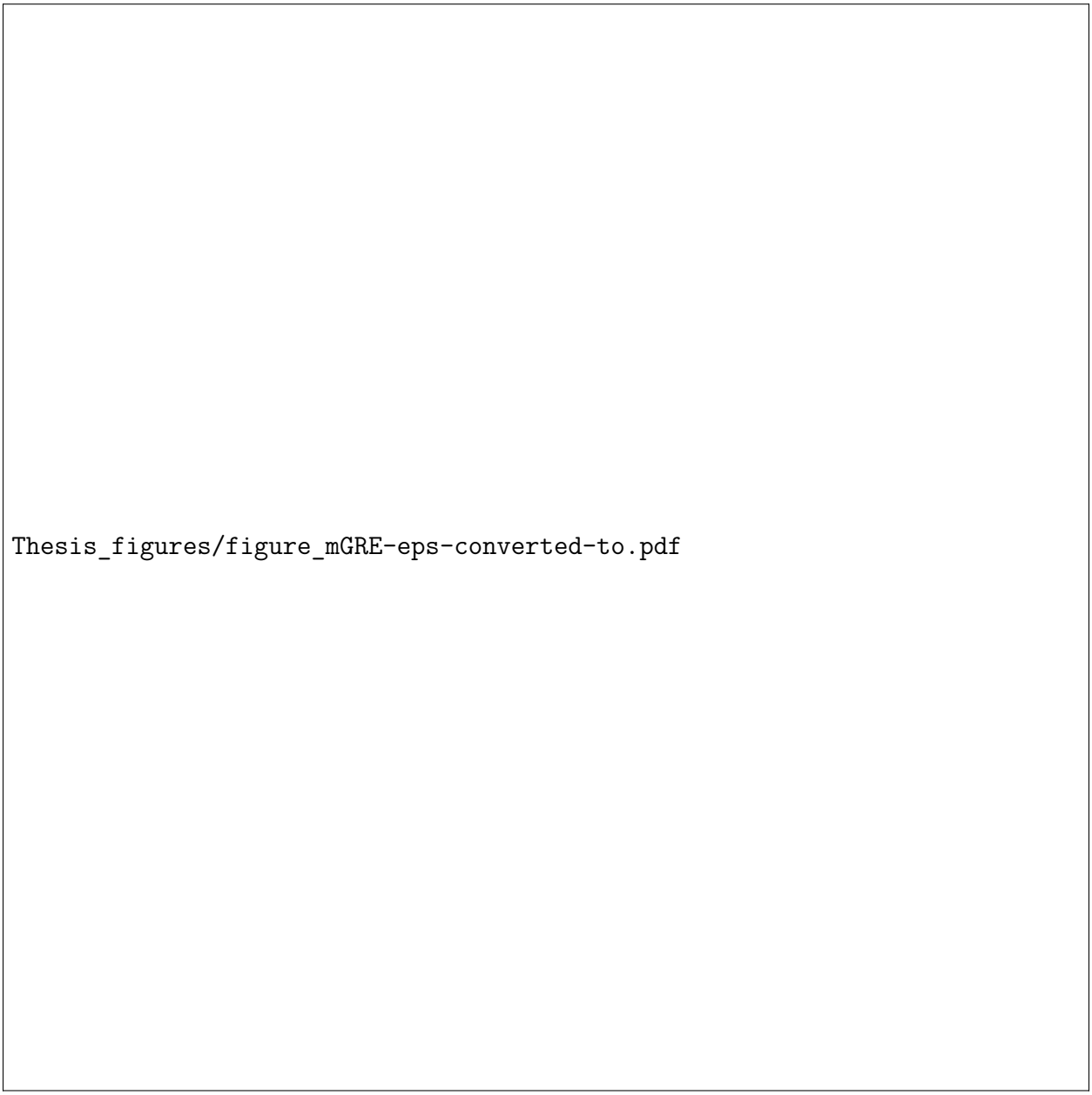

Figure 2.6: Schematic of a monopolar mGRE sequence sequence parameters, consisting of an RF pulse with FA θ repeated at an interval TR, with phase encode gradients G_{PE1} and G_{PE2}. Within each TR, a readout gradient G_{RO} produces N gradient echoes separated by a time ΔTE, following initial echo time TE_1. Between each RF repeat, spoiling gradients eliminate any remaining signal. Figure adapted with permission [3].

2.3.4 Image quality and acquisition time

The signal-to-noise ratio (SNR) is an important consideration in all imaging modalities. In MRI, the main source of noise is from Brownian motion of electrons in conductive materials, which generate electrical fluctuations. For the complex signal, this noise is modeled as a Gaussian distribution and is additive, produced both in the imaged volume and the RF coils. SNR is proportional to several acquisition parameters including, B_0, $\sqrt{TR}$, voxel size, and $\sqrt{NSA}$, where NSA is the number of signal averages [44].

Scan time, given by equation 2.20 is determined by TR, the number of desired phase encode steps, N_{PE}, and the NSA acquired. As such, increasing FOV and resolution will increase scan time. Likewise, sequences requiring longer TRs to accommodate longer echo trains or contrast requirements, for example, have longer scan times. Finally, increasing SNR by increasing the NSA will in turn increase scan time [49].

$$scan\ time = TR \times N_{PE} \times NSA \tag{2.20}$$

2.3.5 R_1 and R_2^* endogenous oxygen contrast

The sensitivity of tissue R_1 and blood R_2^* offers the potential for non-invasive MR oximetry with endogenous oxygen contrast [16].

Oxygen is a paramagnetic molecule, hence, it causes local distortions in the magnetic field. Spin-lattice interactions between oxygen and surrounding water molecules shorten the

T_1 relaxation time in plasma and tissue [16]. Therefore, there is a linear relationship between tissue T_1 and oxygen partial pressure, PO_2 [24, 25, 52]. This relationship is referred to as the TOLD effect [17]. TOLD contrast imaging is commonly achieved through a variety of quantitative T_1 (or R_1) MRI sequences, the most common of which include the previously discussed VFA and IR approaches in addition to the Locker-Locker (LL) approach [50].

While oxygenated hemoglobin is diamagnetic and does not distort the magnetic field, deoxyhemoglobin is paramagnetic, acting on the magnetic field in a way similar to dissolved oxygen. Unlike the case of dissolved oxygen, however, Hb is contained in the RBCs and therefore sequestered from tissue. Furthermore, the configuration of Hb and the dynamics of water exchange between RBC and plasma reduce the number of spin-lattice interactions, and the field distortion effects of hemoglobin on T_2^* become predominant [15, 16]. At a given pO_2, an equilibrium is reached between Hb and HbO_2, forming a correlation between T_2^* and pO_2 [21, 53]. This is the BOLD effect, where T_2^* (or R_2^*) contrast images are typically taken with GRE sequences [54]. However, it should be noted that blood T_2^* is also impacted by blood flow and volume changes and pH, factors which may also fluctuate with blood pO_2 [21].

TOLD and BOLD contrast can be generated by gas challenges aimed at modulating blood and tissue pO_2. A gas challenge typically consists of two MRI measurements, one at a baseline oxygen concentration, and one at a modified oxygen concentration. Gas challenges can be hyperoxic, where pure oxygen or an oxygen-rich gas is administered to the patient

to increase pO_2, or hypoxic, where oxygen-poor gasses, are administered to reduce pO_2 [17, 18, 20, 55–58]. Whereas most normoxic tissues tend to show an R_2^* and R_1 change in response to a gas challenge [59–61], researchers have shown that hypoxic tumour volumes would exhibit a reduction or lack of response, serving as a basis for hypoxia imaging.

Indeed, several studies have shown links between ΔR_1 and or ΔR_2* in response to oxygen challenges consistent with physiological markers for hypoxia such as tumour size both in pre-clinical [58] and clinical [62–65] studies. Several groups also compared BOLD and/or TOLD-based tumour hypoxia maps with other techniques such as histological staining and PET and found a significant correlation between techniques [20, 57, 66–68]. Furthermore, ΔR_1 and or ΔR_2* measurements in response to gas challenges were found to change in response to therapy [17, 56, 69, 70], and to be predictive of treatment outcomes [18, 71, 72].

While promising, both clinical and pre-clinical research has also underlined limitations in BOLD and TOLD approaches to tumour hypoxia. First, BOLD measures blood oxygenation, and is limited by its non-specificity to tumour hypoxia [73]. Furthermore, several groups have found TOLD response to change following treatment while BOLD does not, suggesting TOLD is a more robust tracker of tumour response [17, 56, 69]. Nonetheless, BOLD imaging provides important complementary information to tumour hypoxia imaging and should not be discounted entirely. Indeed, the BOLD sensitivity to oxygen challenges is often stronger than the TOLD sensitivity, making TOLD a less reliable marker for hypoxia in some tumour models [20, 55, 58].

The limited R_1 response to a respiratory challenge is likely due to the low solubility of oxygen in water. However, oxygen has a six-fold increase in solubility in fat compared to water [74], and isolating the T_1 of fat (T_{1f}) has been shown to increase T_1 sensitivity to changes in pO_2 [22, 25]. Furthermore, one T_{1f} imaging technique, mapping of oxygen by imaging lipids relaxation enhancement (MOBILE), has been shown to increase R_1 sensitivity to changes in oxygen in mammary tumours in mice [23]. This technique, however, uses water suppression and is, therefore, unsuitable for low-fat fraction environments [25].

2.3.6 Fat suppression and imaging

Capitalizing on T_{1f} for tumour hypoxia imaging hinges on understanding the role of fat and water in the MRI signal, which can be seen as the sum of the signals generated by the various materials present in the voxel. Given that fat and water are responsible for the bulk of the MRI signal, it can be represented mathematically by equation 2.21, where S_w and S_f are the fat and water components of the signal.

$$S_0 = S_w + S_f \tag{2.21}$$

Separating or suppressing the fat and water signals can be achieved by capitalizing on differences in R_1 between fat and water or chemical shift [75, 76].

R_1-based fat or water suppression techniques exploit the higher fat R_1 to selectively

excite one signal component. In the short TI inversion recovery (STIR) approach to fat suppression, for example, an initial 180° flip is applied to the volume of interest. The greater R_1 of fat results in quicker signal recovery. A second 90° excitation is applied at $T_{1f}\log(2)$ when the fat signal is entirely in the transverse plane and therefore has a net magnetization of zero, such that only the water protons are excited [76].

Chemical shift refers to a change in the Larmor frequency due to the chemical environment of the nuclei making it more or less susceptible to the magnetic field compared to a reference material. In water, the strong electronegativity of oxygen compared to hydrogen pulls the hydrogen electron away from the ^{1}H nucleus. This leaves the ^{1}H less "shielded" from the B_0 field compared to a less polar bond, such as that of hydrogen and carbon in a triglyceride chain. This results in a slight change in the Larmor frequency between these two chemical environments. This change ω_σ, for a given shielding parameter σ, is given by equation 2.22. In practice, this frequency change for a given sample, ω_{ref} is measured as the chemical shift, δ, relative to a reference frequency, typically considered to be water, in ppm, as in equation 2.23 [44]. The MOBILE technique for mapping R_1 of fat, R_{1f}, uses a narrow RF bandwidth to selectively excite the fat ^1H [23].

$$\omega_{ref} = (1 - \sigma)\omega_0 \tag{2.22}$$

$$\delta = \frac{\omega_{sample-\omega_r ef}}{\omega_r ef} * 10^6 (ppm) \tag{2.23}$$

While the fat resonance frequency is often simplified to a single peak, it should be noted that ^{1}H in fat experiences an array of chemical environments, resulting in a spectrum of chemical shifts, rather than a single peak. [77].

Chemical shift can also be used to separate the fat and water components of the signal. The difference in Larmor frequency, and therefore, precession frequency, between fat and water gives rise to a time-dependent relative phase difference. When in phase, fat and water signals are additive, and when out of phase, phase shifted by 180°, they are subtractive. Out-of-phase images can increase signal contrast in tissues where fat and water content are similar [76]. Furthermore, some imaging approaches measure the signal at three or more echo times to solve for the fat and water signals separately in addition to the B_0 field. Examples of this approach include the iterative decomposition of water and fat with echo asymmetric and least-squares estimation (IDEAL) [78], three-point Dixon approach, which combines region growing algorithm to determine the correct analytical solution to its signal model [79, 80], and the Graph Cut algorithm, which transforms the fitting problem into an optimal segmentation problem [81]. The ratios of these signals are then used for quantitative proton density fat fraction images.

2.3.7 Fat DESPOT

While BOLD, TOLD, and MOBILE MRI techniques have been shown to provide promising insights into tumour hypoxia, as previously mentioned, they are imperfect techniques. BOLD measurements probe tissue oxygen indirectly through measurements of blood oxygen [21]. While TOLD measurements probe tissue oxygen directly, they can suffer from low sensitivity [23]. MOBILE has been suggested as a remedy to TOLDs sensitivity issues, by suppressing the water signal and isolating the T_{1f}, however, this method is limited to a high-fat fraction environment, as it does not measure T_{1w} or global T_1, $T_{1glaobal}$ [26].

Our research group has suggested applying the Fat-separated Driven Equilibrium Single Pulse Observation of T_1, fat DESPOT, technique to MRI oximetry. This is a multiparametric mapping technique that returns maps of PDFF, R_2^*, and R_1 of fat and water separately by fitting the Fat DESPOT signal model to a VFA mGRE acquisition [26]. By simultaneously obtaining R_2^*, R_{1f}, and R_{1w}, changes in both blood oxygen and tissue oxygen can be observed. Furthermore, by conserving the R_1 of fat and water, either or both metrics can be used, depending on the fat fraction, as determined by the PDFF estimate, thereby not limiting the technique to high-fat tissues.

The conventional approach to Fat DESPOT, as presented by Le Ster *et al.*, proposes a fat-water separate model for the magnitude of the mGRE signal acquired at two or more FAs, as seen in equation 2.24, where the fat and water signals are given by equation 2.25 and 2.26 respectively [26]. This model fits the magnitude of the MRI signal and will be referred

to in this thesis as Fat DESPOT$_m$, such that B_0 field inhomogeneity (ΔB_0) and initial phase (Φ_0) can be ignored as they do not affect the magnitude of the signal. It should be noted that this simplification assumes that the fat and water components of the signal have the same ϕ_0. Given the complexity of this signal model, a 3-point DIXON estimate of PDFF and a DESPOT $R_{1global}$ measurement are used to provide initial guesses to the Fat DESPOT fitting algorithm [25].

Using this approach, our group has previously conducted phantom-based oximetry validation studies, showing that the R_{1f} is indeed more sensitive than R_{1w} or $R_{1global}$ to changes in pO_2 [25]. However, the clinical translation of this approach is challenged by long imaging times, due to Fat DESPOT requiring two six-echo acquisitions to achieve a 12-echo dataset with artificially short TEs, increasing accuracy of the fat-water separation, and four FAs to cover a wide range of expected R_1 values [25].

$$S_{meas}(TE, TR, \theta) = S_0 \left[(1-f)W + fF \sum_{n=1}^{N} A_n e^{\Delta w_n TE} \right] e^{-R_2^* TE}; \tag{2.24}$$

$$F = \left[\frac{(1 - e^{-R_{1f}TR}) sin(\theta_n)}{1 - e^{-R_{1f}TR} cos(\theta_n)} \right] \tag{2.25}$$

$$W = \left[\frac{(1 - e^{-R_{1w}TR}) sin(\theta_n)}{1 - e^{-R_{1w}TR} cos(\theta_n)} \right] \tag{2.26}$$

To reduce imaging times and improve the quality of the subsequent fit, our group proposes

a complex approach to Fat DESPOT, referred to in this thesis as Fat DESPOT$_c$, be taken. By fitting the complex signal, the available data can be fully exploited. In a practical sense, this means that for each echo, two data points, corresponding to the real and the complex components of the signal, can be used, compared to a single magnitude data point in Fat DESPOT$_m$ and fewer echoes are required to complete Fat DESPOT fitting. Fat DESPOT$_c$, as proposed by our research group therefore fits data to the model presented in equation 2.27 [3, 25]. In simulations, Fat DESPOT$_c$ was optimized to a single 8-echo acquisition at each FA. Theoretically, these 8 echoes could be contained in a single TR of the same length as the TR used in the conventional approach, effectively reducing the acquisition time by 50% [3]. However, modeling the complex signal requires a model that accounts for the ϕ_0 and ΔB_0. Introducing these additional parameters to the signal model makes it vulnerable to phase errors [82]. Both approaches must therefore be rigorously compared.

$$S_{meas}(TE, TR, \theta) = S_0 \left[(1-f)W + fF \sum_{n=1}^{N} A_n e^{-i\Delta w_n TE} \right] e^{R_2^* TE} e^{-i(2\pi\gamma \Delta B_0 TE)} e^{-i\phi_0} \quad (2.27)$$

Simulations previously conducted by our research group have indicated that Fat DESPOT$_c$ outperforms the Fat DESPOT$_m$ returning higher estimates of R_{1f} with higher precision and accuracy over a wider range of fat fractions [3]. Yet, when compared in retrospective data, Fat DESPOT$_c$ behaved significantly more poorly than Fat DESPOT$_m$,

and achieved lower goodness of fit. However, this retrospective analysis was flawed, as complex fitting was performed on the six echo acquisitions obtained for the magnitude approach, and therefore not optimized for the complex model [3]. To conduct a fair comparison, new phantom data must therefore be collected.

Chapter 3

Comparing the magnitude and complex approaches to Fat DESPOT multiparametric mapping

This chapter consists of a preliminary version of a manuscript to be submitted to the journal Magnetic Resonance in Medicine. The goal of this study was to compare the precision and accuracy of the magnitude and complex approaches to Fat DESPOT in simulations, in phantom and in vivo, and their consistency with other published multiparametric MRI approaches. This work will guide the decision on which approach will be used by our research group and others in future MR oximetry of tumours.

In the Fat DESPOT processing pipeline described in section 2.3.7, the 3-point DIXON

algorithm was used to obtain initial guesses for PDFF and B_0, while a rapid R_2* algorithm, which fits the exponential of the decay curve, was used for the R_2^* initial guess [1]. In the work presented in this chapter, the Gaph Cut (GC) algorithm was used to obtain more robust initial guesses for PDFF and R_2^*. Furthermore, the GC fat-water separated complex signal outputs allowed for the estimation of ϕ_0, where a different initial phase for fat and water was observed. Hence, the model used to fit the mGRE data in the Fat DESPOT$_c$ approach differs from that presented in equation 2.27 in section 2.3.7, due to the inclusion of separate initial phases, ϕ_{0f} and ϕ_{0w}. FA-specific B_0 fields, $B_{0\theta}$ were also included in the model, following the observation that the B_0 field differed between FAs for some measurements. The evolution of the Fat DESPOT model and pipeline is detailed in Appendix 2 (section 6.2) of this thesis.

Additional work on accelerating the Fat DESPOT acquisition time was completed but outside of the scope of the study presented in this manuscript. However, this work provides valuable insights into Fat DESPOT acceleration which would benefit future experiments. Hence, it has been detailed in Appendix 3 (section 6.3) for future reference. Likewise, high-fat fraction phantoms proved difficult to achieve. As such a detailed set of instructions on phantom preparation is presented in Appendix 1 (section 6.1) as a resource for future work with variable fat-fraction phantoms.

Comparing the magnitude and complex approaches to Fat DESPOT multiparametric mapping

Renée-Claude Bider[1], Cristian Ciobanu[1], Jorge Campos Pazmiño[1,2], Véronique Fortier[1,3,4,5], Evan McNabb[3,4], Ives Levesque[1,2,4,5,6,7*]

1 Medical Physics Unit, McGill University, Montréal, QC, Canada

2 Department of Physics, McGill University, Montréal, QC, Canada

3 Medical Imaging, McGill University Health Center, Montréal, QC, Canada

4 Department of Diagnostic Radiology, McGill University, Montréal, QC, Canada

5 Gerald Bronfman Department of Oncology, McGill University, Montréal, QC, Canada

6 Research Institude of the McGill University Health Centre, Montréal, QC, Canada

7 Biomedical Engineering, McGill University, Montréal, QC, Canada

***Corresponding author:

Name	Ives Levesque
Department	Medical Physics Unit
Institute	McGill University
Address	Cedars Cancer Centre, DS1.9326 1001 boul Décarie, Montréal, Québec, Canada, H4A 3J1
E-mail	ives.levesque@mcgill.ca

Manuscript word count: 5092
Abstract word count: 227

Abstract

Purpose: Fat DESPOT is a multiparametric mapping technique that provides R_{1f}, and R_{1w}, the fat- and water-specific estimates of R_1, in addition to the estimation of Proton Density Fat Fraction (PDFF), and R_2^* which could valuable insights into various diseases. However, in its conventional form, Fat DESPOT fits the magnitude of a variable flip angle (VFA) multi echo gradient echo (mGRE) signal, only using part of the available data. Fitting to the complex signal would fully exploit the signal information, potentially allowing for higher accuracy and precision in shorter acquisition times. **Methods**: In this work, the magnitude and complex approaches to Fat DESPOT were compared in simulations and experiments at 3 T in a variable fat fraction gel phantom and in vivo in the lower leg of a healthy participant. **Results**: In phantom, the complex approach showed better agreement with reference values of PDFF. In the phantom and in vivo, the complex approach also fit the data better and had higher overall precision. These observations were partially explained by simulations, where the magnitude approach to Fat DESPOT was more vulnerable to fit errors due to differences between the initial phases of the fat and water signal components. **Conclusion**: With a higher precision and accuracy, and a shorter acquisition time than the magnitude approach, this work demonstrates the advantages of complex fitting in Fat DESPOT multiparametric imaging.

Keywords Multiparametric imaging, Relaxation mapping, Fat-water separation, gel phantom, in vivo, Fat relaxation rate, Water relaxation rate,

Introduction

Quantitative MRI mapping of proton density fat fraction (PDFF) and relaxometry parameters, R_1, R_2, and R_2^* offer promising insights into disease. Notably, mapping R_2^* and PDFF in the pancreas has offered insights into the iron overload in patients with a variety of diseases including thalassemia major [2, 3]. Meanwhile, mapping PDFF, R_1, and R_2^*, could differentiate between types of liver disease [4, 5] and correlate with treatment outcomes [5–7]. Finally, joint mapping of R_2^* and R_1 have offered valuable insights into tumour hypoxia [8]. However, when separate acquisition protocols are required for each measured parameter, imaging time can become a challenge, as long acquisition times are taxing on patients, increase the risk of motion artifacts, and make dynamic imaging impossible. Multiparametric mapping, where a single acquisition protocol obtains maps for several parameters, can significantly reduce acquisition times [7, 9].

The conventional approach to Fat DESPOT, referred to in this work as Fat DESPOT$_m$, [9, 10] is a multiparametric fitting technique, which models the magnitude of a variable fip angle (VFA) multi echo gradient echo (mGRE) signal to obtain maps for PDFF, R_2^*, the R_1 of water, R_{1w}, and the R_1 fat, R_{1f}, simultaneously. This method proposes several advantages. Notably, the number of fitted parameters makes it versatile in its application. For example the isolated R_{1w} is frequently used in MRI-based assessments of liver disease [11, 12], while R_{1f} mapping has been proposed to increase the sensitivity of R_1 based MR oximetry [1, 13] due to the increased solubility of oxygen in fat relative to water. Indeed, our group has

validated the Fat DESPOT approach for oximetric measurements in phantom [1].

In contrast with other multiparametric approaches to mapping R_{1f} and R_{1w} [10], our group's previously published implementation of the Fat DESPOT technique used in this study has a larger number of Flip angles (FAs) to accommodate a wide range of anticipated R_1 values and more echoes to improve fat-water separation. This comes at the cost of imaging time. Due to requirements for shorter echo spacing (ΔTE), our implementation of Fat DESPOT also involves two mGRE acquisitions for each FA to create artificially short ΔTE, for a total of 8 acquisitions [1]. Modifying the Fat DESPOT technique to model the complex mGRE signal would fully exploit the available data from the mGRE sequence by fitting the real and imaginary components of the signal. This provides additional information on the off-resonance behaviour of the water-fat shift, reducing the amount of data required for the subsequent Fat DESPOT fitting. This, paired with more flexible echo selection, would allow Fat DESPOT to be performed in a single acquisition per FA, enabling a reduction in imaging time. Additionally, the more complete picture of the data provided by the complex fitting, referred to in this manuscript as Fat DESPOT$_c$, might increase the quality of the resulting estimates. Indeed, in fat-water separation approaches, using the complex signal has increased precision of PDFF, R_{1f}, and R_{1w} and accuracy of PDFF estimates [14], suggesting Fat DESPOT may see the same benefits. However, complex models have also made fat-water separation more vulnerable to phase errors [15]. Hence, a rigorous assessment of the magnitude and complex approaches to Fat DESPOT is required.

In this work, we introduce the Fat DESPOT$_c$ model and conduct a systematic comparison of Fat DEPOT$_m$ and Fat DESPOT$_c$, in simulation, in a phantom, and in vivo, to assess their performance across a wide range of fat fractions.

Methods

All simulations and data processing were completed in MATLAB (Mathworks, USA, R2023a).

The Fat DESPOT approach

In the Fat DESPOT$_m$ approach, the model presented in equation 3.1 is fit to the magnitude of the mGRE data, where f is the fat fraction, F and W are the fat and water signal components, given by 3.3 and 3.4 respectively. The Fat DESPOT$_m$ assumes that the initial phases of fat and water are identical (ϕ_{0f}=ϕ_{0w}), such that ϕ_0 falls out of the model as it does not impact the magnitude of the mGRE signal. However, phase information is retained when fitting the complex signal in the Fat DESOT$_c$ approach. Hence, in Fat DESPOT$_c$, a modified Fat DESPOT model (equation 6.1) can be fitted to the real and imaginary parts of the mGRE acquisition. In the complex case, the initial phases ϕ_{0f} and ϕ_{0w} are modeled separately to improve goodness of fit [16]. Additionally, the B_0 field inhomogeneity, ΔB_0 must also be considered due to its effect on phase progression. In the experiments presented in this work, the B_0 field map was observed to vary between flip angle acquisitions, and so

an FA-specific ΔB_0, denoted $\Delta B_{0,\theta}$, was used to account for these changes in the B_0 field between acquisitions.

$$S_{meas}(TE,TR,\theta) = S_0\left[(1-f)W + fF\sum_{n=1}^{N} A_n e^{\Delta w_n TE}\right] e^{-R_2^* TE} \tag{3.1}$$

$$S_{meas}(TE,TR,\theta) = S_0\left[(1-f)We^{-i\Phi_{0w}} + fF\sum_{n=1}^{N} A_n e^{-i\Delta w_n TE}e^{-i\Phi_{0f}}\right] e^{R_2^* TE}e^{-i2\pi\gamma\Delta B_{0,\theta}TE} \tag{3.2}$$

$$F = \left[\frac{(1-e^{-R_{1f}TR})sin(\theta_n)}{1-e^{-R_{1f}TR}cos(\theta_n)}\right] \tag{3.3}$$

$$W = \left[\frac{(1-e^{-R_{1w}TR})sin(\theta_n)}{1-e^{-R_{1w}TR}cos(\theta_n)}\right] \tag{3.4}$$

Simulations

To investigate the effect of assuming equal initial phases for fat and water on the Fat DESPOT$_m$ fit, two scenarios were investigated in simulation, using $\phi_{0w} = \phi_{0f}$ and $\phi_{0w} \neq \phi_{0f}$ in the input to the simulations.

A synthetic signal was generated with R_{1f}, R_{1w}, and R_2^* values based on reported values from in-vivo measurements of the liver [17, 18] and ϕ_{0w}, ϕ_{0f}, and ΔB_0 values based

on our experiments. A single value for ΔB_0 was used for all flip angles in the simulated signal and in the Fat DESPOT model. PDFF was modulated in 5% increments from 5% to 95% to assess the performance of the magnitude and complex approaches to Fat DESPOT across fat fractions. A six peak model of the chemical shift spectrum of peanut oil, with chemical shift (ω) = [0.80 ppm, 1.20 ppm, 2.00 ppm, 2.66 ppm, 4.21 ppm, 5.20 ppm,] and amplitude (a) = [0.087, 0.694, 0.128, 0.004, 0.039, 0.048], was borrowed from experimental measurement [19]. Noisy realizations were generated by adding Gaussian-distributed noise adjusting the noise amplitude to reach a Signal-to-noise Ratio (SNR) of 100 calibrated to the first echo, and largest FA acquisition, as described by equation 3.5, where N is a normal distribution, centered around either the real part of the standard noises signal, $R(S_{noisless})$ or the imaginary part of the noiseless signal, $J(S_{noisless})$, with a standard deviation (σ) = $\sqrt{(|S_{noisless}|^2)/(SNR^2)}$. 1000 realizations of the noisy mGRE signal were calculated for each fat fraction increment.

Imaging parameters for the synthetic mGRE signal were selected to match experimental values. For the Fat DESPOT$_m$ simulation, a 12-echo sequence with echo spacing (ΔTE) = 1.2 ms, and repetition time (TR) = 18 ms were generated at each FA. This TR is the shortest possible given the echo requirements.

Incorporating complex data into the Fat DESPOT model reduces the required number of echoes and allows for more flexibility in the echo time selection given the bandwidth voxel parameters from experiments (Table 3.3). Hence, the mGRE sequence was previously re-

Parameter	Value	
Iterations		1000
SNR		100
R_{1w} (s^{-1})		1.25
R_{1f} (s^{-1})		3.33
R_2* (s^{-1})		36.50
S_0		1000
ϕ_{0f}/π		0.5, 0.8
ϕ_{0w}/π		0.5
ΔB_0(Hz)		10
	Fat DESPOT$_m$	Fat DESPOT$_c$
TR (ms)	18	24
FAs (\degree)	3,6,15,34	3,7,17,49
TE_1 (ms)	1.5	1.9
ΔTE (ms)	1.2	1.8
# echoes	12	8

Table 3.1: Signal generation and imaging parameters for Fat Despot simulations comparing Fat DESPOT$_m$ and Fat DESPOT$_c$ approaches.

optimized by our group for Fat DESPOT$_c$ in simulation, using a simplified complex signal model with a shared phase for fat and water and single B_0 . In these optimizations, a noisy complex Fat DESPOT signal (SNR=100) was generated for combinations of TE_1 between 1.3 ms and 2.7 ms and ΔTE between 1.2 ms and 2.8 ms and PDFF values between 10% and 90%. The echo number was set to the maximum number of echoes able to fit in a TR=18 ms. The Fat DESPOT multi-parametric estimates were then calculated, along with error and standard deviation compared to the ground truth. Acceptable TE combinations were determined based on R_{1f} error $< 20\%$ and $R_1 f$ standard deviation $< 20\%$ for all fat fractions. This optimization resulted in an 8 echo measurement with ΔTE = 1.8 ms, and TE_1 = 1.9 ms for the Fat DESPOT$_c$ experiments [20]. To match the achievable TR on our

MRI system, which had a lower bound of 24 ms when collecting 8 echoes with these echo times.

FAs in simulations were also selected to match phantom experiments, where they were optimized for R_1 range from 0.54–2.9 s^{-1}, and for their respective TRs [21, 22]. For the magnitude approach with TR=18 ms, selected FAs were 3, 6, 15, and 34°. For the complex approach with TR=24 ms, selected flip angles were 3, 7, 17, and 39°. Synthetic signal and mGRE simulation parameters are summarized in table 3.1.

$$S_{noisy} = N\left(R(S_{noisless}), \frac{|S_{noiseless}|^2}{SNR^2}\right) + iN\left(J(S_{noisless}), \frac{|S_{noisless}|^2}{SNR^2}\right) \tag{3.5}$$

To obtain initial guess values and fit the Fat DESPOT$_m$ and Fat DESPOT$_c$ models, processing of the synthetic mGRE signal followed the same procedure as the processing of the phantom and in-vivo data, outlined in the data processing section of the methods, excluding image registration and B_1 correction as B_1 field inhomogeneity was not introduced in the model.

Phantom construction

To compare the magnitude and complex approaches to Fat DESPOT experimentally across a range of fat fractions, a phantom was constructed following the protocol outlined by Bush *et al.* [23]. Five emulsions of peanut oil (JVF Canada inc), and a 3% agar by weight (agar powder, MilliporeSigma Canada Ltd) solution were prepared in ratios of 5%, 25%,

50%, 60%, and 75% nominal fat fraction. Before combining,sorbitan monooleate (span 80, MilliporeSigma Canada Ltd), a surfactant, and sodium benzoate (MilliporeSigma Canada Ltd) were added to the agar solution. Likewise, the surfactant polyethylene glycol sorbitan monolaurate (Tween 20, MilliporeSigma Canada Ltd) was added to the peanut oil. Gadobutrol (Gadovist, Bayer Healthcare) was added as a relaxation agent, at a concentration of $[Gd^+]$= 0.2 mM in the agar gel preparation before mixing it into the emulsion. Each emulsion was placed in a 50 mL conical polypropylene tube (Corning® 50 mL centrifuge tubes). Two additional tubes, one containing peanut oil only and one containing the agar solution only were also prepared, for a total of seven nominal fat volume fractions ranging from 0 to 100%. The tubes were then suspended on a plastic and polystyrene rig placed in a cylindrical acrylic phantom container (Magphan ®SMR170, The Phantom Laboratories, Salem, USA), which was then filled with a solution of distilled deionized water with gadobutrol ($[Gd^+]$=0.3 mM) and sodium chloride (Windsor Salt Ltd) ([NaCl]=24 mM) to approach the conductivity of human tissue [24].

Phantom data acquisition

All MRI measurements were performed at room temperature in a 3 T MRI scanner (Ingenia, Philips Healthcare) using a vendor-provided 15-channel head coil for the phantom measurements. The phantom was left to rest for at least 30 minutes before all measurements to eliminate flow artifacts. For Fat DESPOT measurements, a 3D mGRE

sequence with monopolar readout and default spoiling was employed with parameters specific to each approach. Measurements for both the Fat DESPOT$_m$ and Fat DESPOT$_c$ approach were collected at four excitation pulse FAs. A summary of all sequence parameters used in these experiments can be seen in Table 3.3.

In the magnitude approach outlined by Fortier *et al.* [1], two 6-echo sequences, with ΔTE = 2.4 ms and TR = 18 ms were acquired at each FA. For the first acquisition, the initial echo time (TE$_1$) = 1.5 ms, and for the second acquisition, TE$_1$ = 2.7 ms. TE$_1$s were selected such that the two acquisitions could be combined in post-processing to create a 12-echo train with shorter apparent ΔTE (= 1.2ms). For Fat DESPOT$_c$, a single 8-echo measurement with ΔTE = 1.8 ms, TE$_1$ = 1.9 ms, and TR = 24 ms at each FA, matching the simulations. In both the magnitude and complex approaches to Fat DESPOT, eight signal averages were acquired for each measurement and parallel imaging was not used.

As discussed in the simulations section of the methods, in phantom measurements, flip angles were optimized for their respective TRs and for the lower and upper limits of an R_1 range from 0.54 -2.9 s^{-1} [1,25] and combined for a set of four FAs [21,22]. For the magnitude approach with TR = 18 ms, selected flip angles were θ=[3°, 6°, 15°, 34°]. For the complex approach with TR = 24 ms, selected flip angles were θ=[3°, 7°, 17°, 39°].

For accurate R_1 measurements, the signal was corrected with a B_1 map. The B_1 map acquisition was done using a multi-slice turbo spin-echo (MS TSE) acquisition at two angles (FA = 60, 120°) [1].

	Fat DESPOT$_m$	Fat DESPOT$_c$	B_1 mapping	Unipolar FW separation
Acquisition type	mGRE	mGRE	MS TSE	mGRE
TR (ms)	18	24	1000	18
TE$_1$ (ms)	1.5, 2.7	1.9	9	1.1
ΔTE	2.4	1.8	–	1.7
# TE	6× 2	8	1	6
NSA	8	8	1	8
FA - Phantom (°)	3, 6, 15, 34	3, 7, 17, 39	60, 120	3
FA - in vivo (°)	3, 8, 19, 45	4, 10, 22, 51	60, 120	3
BW(Hz/px)	1360	1360	1360	1360
Voxel Size - Phantom (mm^3)	210×210×100	210×210×100	210×210×90	210×210×100
Voxel Size - in vivo (mm^3)	1.875×1.875×5	1.875×1.875×5	1.875×1.875×5	1.875×1.875×5
FOV - Phantom (mm^3)	192.5×192.5×100	192.5×192.5×100	192.5×192.5×90	192.5×192.5×100
FOV - in vivo (mm^3)	192.5×160.4×100	192.5×160.4×100	192.5×160.4×90	192.5×160.4×100
Scan Time - Phantom (min)	5.05	6.87	3.3	5.61
Scan Time - in vivo (min)	3.47	5.15	2.3	3.88

Table 3.3: Sequence parameters for complex and magnitude Fat DESPOT, B_1 mapping, and referencePDFF measurement in phantom and in vivo.

An additional unipolar mGRE sequence (TE_1 = 1 ms, # of echoes = 6, ΔTE=1.7 ms, FA=3°) was acquired to obtain a reference measurement for PDFF.

All measurements had an acquired voxel size of 1.875×1.875×5.0 mm^3, covering a 210×210×100 mm^3 field of view (FOV) for mGRE measurements and a 210×210×90 mm^3 FOV for MS TSE measurements. The total scan time was 47 minutes for Fat DESPOT$_m$ and 34 min for Fat DESPOT$_c$. The additional scan time for the reference measurement for PDFF was 5.6 min.

in vivo data acquisition

To compare the magnitude and complex approaches in vivo, a series of pilot measurements were conducted in the lower leg of a volunteer (healthy male, age 24) using the same 3 T MRI scanner as the phantom measurement and an 8-channel extremity coil, and following the same acquisition protocol as the phantom measurements, excluding the PDFF reference measurement. FAs were reoptimized to better represent the R_1 range of human tissue, 0.56-3.33 s^{-1}, as used in recent work by our group [20]. This resulted in FAs of θ=[3°, 8°, 19°, 45°] for Fat DESPOT$_m$ and θ=[4°, 10°, 22°, 51°] for Fat DESPOT$_c$. To reduce acquisition time, a smaller FOV (192.5×160.4×100 mm^3) and larger voxel size (2.00×2.00×5.00 mm^3) were selected. All other parameters were preserved from the acquisition protocol for phantom measurements, including the number of averages and the absence of parallel imaging. in vivo, the total scan time was 36 min for Fat DESPOT$_m$ and 25 min for the complex approach.

Parameter	Lower Limit	Upper Limit
S0	0.00001	1×10^{15}
PDFF (%)	GC PDFF - 5	GC PDFF +5
R_2^* (s^{-1})	0	1000
R_{1f} (s^{-1})	0	10
R_{1w} (s^{-1})	1/3	10
Phi_{0f} (rad)	0	2π
Phi_{0w} (rad)	0	2π

Table 3.4: Lower and upper bounds for fitting parameters used in Fat DESPOT$_m$ and Fat DESPOT$_c$.

Data processing

The mGRE data underwent several preprocessing steps before Fat DESPOT fitting. For Fat DESPOT$_m$, the two acquisitions taken at each FA were recombined into a single data set by alternating echoes in increasing echo order. A relative B_1 map was then constructed from the dual angle MS TSE acquisition and used to scale the nominal FA for each voxel [26]. For the in vivo experiment, all images including B_1 maps were registered to the 3° MGRE Fat DESPOT acquisition using rigid registration (function *imregtform* with default parameters, MATLAB 2023).

Next, using the graph cut (GC) algorithm for fat-water separation [15], initial guess maps of PDFF and R_2* were obtained for both approaches to Fat DESPOT, and two additional initial guess maps for the initial phase of fat and water (ϕ_{0f} and ϕ_{0w}) were obtained for Fat DESPOT$_c$ along with FA-specific B_0 maps ($B_{0\theta}$) which were used as fixed parameters in the subsequent fitting algorithm. The initial guesses maps of R_2^*, PDFF , ϕ_{0f} and ϕ_{0w} were

obtained from the 3° FA data. While the R_2^* map is provided directly from the GC output, the PDFF, and ϕ_{0f} and ϕ_{0w} maps were calculated from the fat-water separated complex signal maps. For Fat DESPOT$_c$, the separate $B_{0\theta}$ maps were obtained directly from a GC fitting at each FA. Finally, maps of the joint R_1 of fat and water, $R_{1global}$, were calculated using a VFA approach with data from the first echo. In both approaches to Fat DESPOT, the resulting $R_{1global}$ for each voxel was used as the initial guess of R_{1f} for GC estimates of PDFF $> 50\%$ and R_{1w} for GC estimates of PDFF $< 50\%$, and otherwise a fixed initial guess of 4 s^{-1} and 1 s^{-1} for R_{1f} and R_{1w} respectively.

Following this pre-processing, The Fat DESPOT$_m$ and Fat DESPOT$_c$ signal models were fit to their respective mGRE data using a non-linear least-squares algorithm (function *lsqnonlin* using the *trust-region-reflective* algorithm, MATLAB 2023). The same six-peak chemical shift spectrum used to simulate the peanut oil spectrum in simulations was used in the Fat DESPOT fitting of the phantom. For the in-vivo acquisition, a six peak spectrum based on the fat spectrum of skeletal muscle with ω=[5.3 ppm, 4.13 ppm, 2.78 ppm. 2.24 ppm, 1.3 ppm, 0.9 ppm] and a=[0.066, 0.035, 0.011, 0.052, 0.077, 0.047, 0.598, 0.089] was used [27]. Upper and lower bounds for PDFF were set to be within 5% of the PDFF initial guess. All other parameter bounds are displayed in Table 3.4.

The PDFF from the reference measurement was measured from the GC output, as described above.

Statistical analysis

For quantitaive measurements and statistical analysis of PDFF, R_2^*, R_{1f}, and R_{1w}, regions of interest (ROIs) were selected (Figure 3.1). In the phantom, manually drawn circular ROIs with matched volumes (number voxels = 243) were selected to fit within the cross-sectional area of each tube, while in vivo, circular ROIs were selected for the bone marrow and muscle and a rectangular ROI for the subcutaneous fat layer. Due to the size and shape of the bone marrow and subcutaneous tissue, a geometrical ROI could not be used alone without significantly reducing the number of voxels included in the quantitative analysis or including voxels from other tissues. Hence, semi-automatic ROIs were created by including voxels with PDFF $>$ 70% from a larger selection area to ensure that the voxels included in the analysis were representative of the tissue of interest. All ROIs were measured over three slices selected centrally to the imaging volume.

Means, standard deviations, and coefficients of variance were calculated in MATLAB. Comparisson of means was conducted using a two-way ANOVAS for all experiments (function anova2, MATLAB 2023). Inter-technique means were then compared using a one-way ANOVA (function *anova*, MATLAB 2023) and a p-value of 0.05 was used to determine significance. To compare standard deviations between approaches, a two-sample F-test for equal variance (function *vartest2* MATLAB 2023) with a 0.05 significance threshold was used. In order to compare standard deviations, they were averaged across ROIs for each approach following equation 3.6, where n is the number of standard

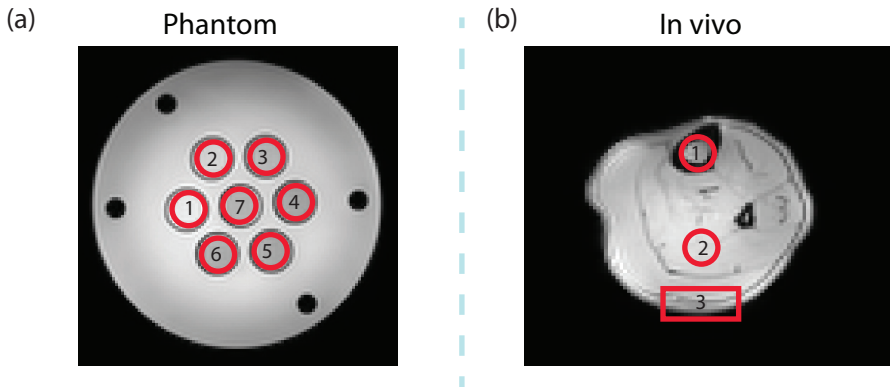

Figure 3.1: Regions of interest for Fat DESPOT$_m$ and Fat DESPOT$_c$ of (a) the variable fat fraction phantom and (b) a human lower leg. In the phantom, ROIs 1-7 correspond to nominal fat fractions of 0%, 5%, 25%, 50%, 60%, 75%, and 100% respectively. In the lower leg, ROIs 1-3 correspond to tubular bone marrow, skeletal calf muscle, and subcutaneous fat. Bone marrow and subcutaneous fat voxels of interest within the ROI were selected based on a fat fraction <70%. All ROIs were measured over 3 slices of the acquired image.

deviations being combined, w is the sample size, and std is the standard deviation.

$$std_{combined} = \sqrt{\sum_{i=1}^{n} \frac{std_n^2}{w_n}} \tag{3.6}$$

Results

Simulation Results

When the ground truth initial phase of the simulated fat and water signals were equal ($\phi_{0f} = \phi_{0w} = 0.5\pi$), Fat DESPOT$_m$ had a slightly higher accuracy, though both approaches were highly accurate. Conversly, when the initial phase of the fat and water signal componentswere different, Fat DESPOT$_m$ resulted in large errors in estimates while Fat DESPOT$_c$ retained a high accuracy.

In the case of identical initial phases, the mean relative error remained low for all parameters. Fat DESPOT$_c$ had a lower mean relative error on R_{1w}, while Fat DESPOT$_m$ had a lower mean relative error on PDFF, R_2^*, and R_{1f}. Indeed, for Fat DESPOT$_m$ the mean relative error for PDFF, R_2^*, R_{1f}, and R_{1w} was 0.43±1.18%, 0.030±0.040%, 0.57±1.40%, and 0.41±1.11% respectively. Likewise, the mean relative error of Fat DESPOT$_c$ for PDFF, R_2^*, R_{1f}, and R_{1w} was 1.3±2.7%, 0.16±0.12%, 0.75±1.12%, and 0.36±0.55%. Fat DESPOT parameter estimates were accurate over a broad range of PDFFs, though PDFF, R_{1f}, and R_{1w} saw steep increases in relative error at ground truth

values of PDFF< 10%, PDFF> 90% and PDFF< 10% respectively. Results for this simulation case are displayed in the top row of Figure 3.2.

In the case where the ground truth initial phase of fat and water signal components was different ($\phi_{0f} = 0.8\pi$ and $\phi_{0w} = 0.5\pi$), the relative error using the Fat DESPOT$_m$ approach increased drastically. In contrast, the relative error remained relatively low for Fat DESPOT$_c$. Indeed, in this case, the mean relative error for PDFF, R_2^*, R_{1f}, and R_{1w} is 3.4±3.8%, 6.0±1.7%, 18±18%, and 123±18% respectively for Fat DESPOT$_m$. Except R_2^*, the error was highest near PDFF=50%. This was a markedly different trend from the simulated results for ϕ_{0f}=ϕ_{0w}. Conversely, the error for Fat DESPOT$_c$ followed the same trend in both ϕ_0 cases, and remaining low overall, with values of 0.56±1.39, 0.1±0.10%, 0.37±0.61%, and 0.31±0.67% for PDFF, R_2^*, R_{1f}, and R_{1w} respectively.

Precision was high and followed similar trends in both initial phase scenarios explored in simulations. Fat DESPOT$_m$ returned more precise estimates for all parameters when the initial phases of the fat and water components of the simulated signal were identical and for R_2^* and $R·1w$ when initial phases were different, while Fat DESPOT$_c$ had more precise estimates of PDFF and R_{1f} when initial phases were different. Specifically, when fat and water shared an initial phase, the mean coefficients of variation of Fat DESPOT$_m$ outputs were 2.0×10^{-4}%, 5.6 $\times10^{-4}$ %, 3.5×10^{-3} %, and 4.5×10^{-3} % for PDFF, R_2^*, R_{1f}, and R_{1w} respectively, while the mean coefficients of variation of Fat DESPOT$_c$ outputs were 2.5×10^{-4} %, 1.4×10^{-3} %, 8.8×10^{-3} %, and 1.4×10^{-2} % for the same parameters. When

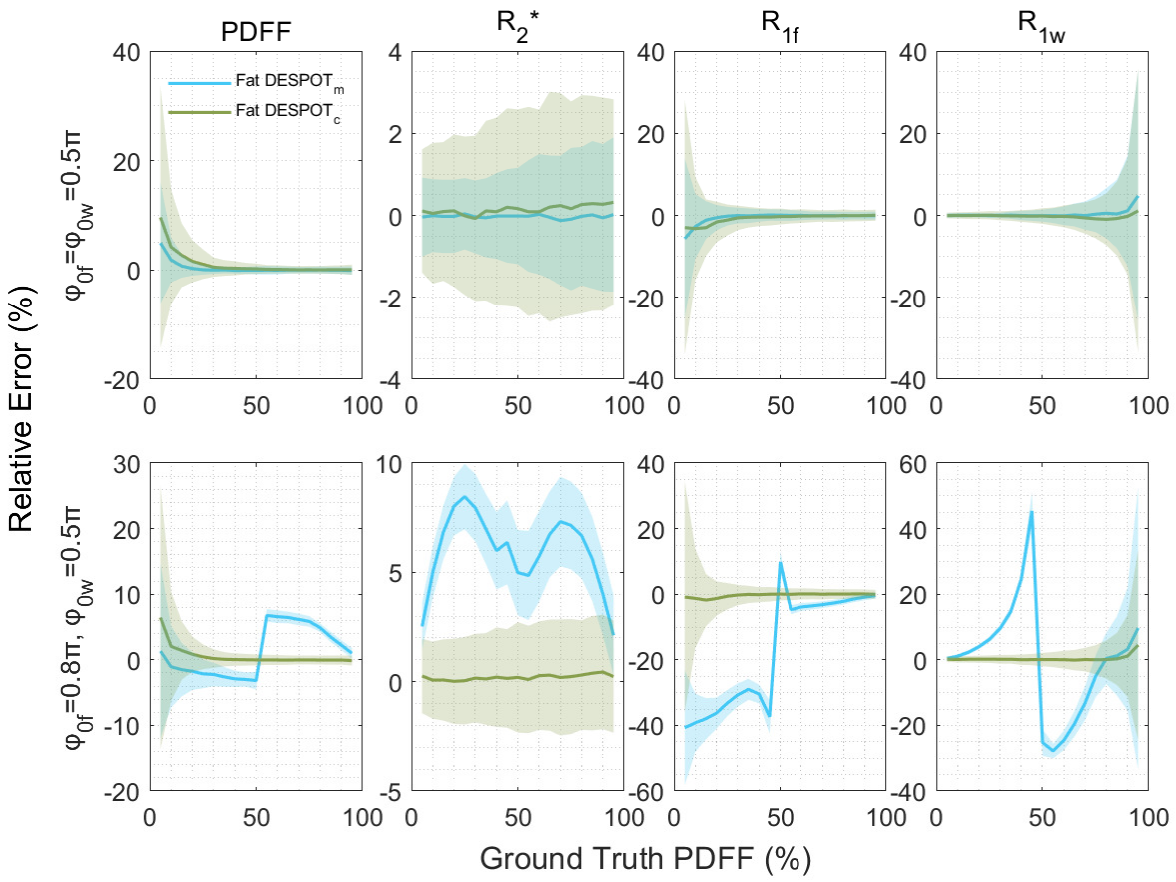

Figure 3.2: Relative error of Fat DESPOT$_m$ and Fat DESPOT$_c$ output parameters compared to the ground truth with SNR=100 for PDFF values between 5% and 95% in the case where fat and water signals have the same initial phase (top row) and in the case where fat and water signals have different initial phases (bottom row).

the initial phases of fat and water were different, the mean coefficients of variation from Fat DESPOT$_m$ were 4.0×10^{-4} %, 6.0 ×10^{-4} %, 6.8×10^{-3} %, and 7.8×10^{-3} % for PDFF, R_2^*, R_{1f}, and R_{1w} respectively, while the mean coefficients of variation of Fat DESPOT$_c$ outputs were 1.8×10^{-4} %, 1.8×10^{-3} %, 6.1×10^{-3} %, and 1.4×10^{-2} % for the same parameters. This is a slight decrease in precision for Fat DESPOT$_m$ and a slight increase in precision for Fat DESPOT$_c$ compared to the identical initial phase case. In both cases, precision was high over a wide range of PDFF values, but reduced drastically for PDFF and R$_1f$ at ground truth PDFF $< 10\%$ and for R_{1w} for ground truth PDFF $> 90\%$, while R_2^* remained fairly constant

Phantom results

Multiparametric maps of PDFF, R_2^*, R_{1f}, and R_{1w} obtained from Fat DESPOT$_m$ and Fat DESPOT$_c$ fitting (Figure 3.3) are fairly uniform within the emulsion tubes. Both approaches to Fat DESPOT returned high-quality fits in all tubes, with an average R^2 value of 0.96 for Fat DESPOT$_m$ and 0.98 for Fat DESPOT$_c$. The lowest average R^2 value using both approaches was 0.90 for Fat DESPOT$_m$ and 0.98 for Fat DESPOT$_c$, corresponding to the tube with a nominal fat fraction of 50%. Artifacts in the R_{1f} maps located in the water compartment and 0% nominal fat fraction tube are due to the Fat DESPOT equation fitting a non-existent fat signal rendering them meaningless. Artifacts also appeared in the R$_2^*$ maps of both approaches to Fat DESPOT, likely due to strong B_0 field inhomogeneity from the

styrofoam support in the phantom not sufficiently accounted for by the model fit.

Examples of initial guess maps from GC and DESPOT$_1$ are presented in Figure S1 of the supplementary materials. Notably, the GC outputs for the phases of fat and water are drastically different, suggesting that these should be distinct free parameters in the Fat DESPOT$_c$ model. An example of Fat DESPOT$_m$ and Fat DESPOT$_c$ voxelwise fits can also be found in the Supplementary materials, Figure S2.

Fat DESPOT$_m$ and Fat DESPOT$_c$ showed similar trends for all parameters versus fat fraction. Notably, R_{1f} and R_{1w} appear to be stable across fat fractions while R_2^* is highest in the tube with a nominal fat fraction of 50% (ROI 4) and lower in both pure water and fat. However, Fat DESPOT$_m$ and Fat DESPOT$_c$ returned significantly different parametric estimates ($p<0.05$), excluding PDFF in the 75% nominal fat fraction tube (ROI 6) and R_{1w} in the 50% nominal fat fraction tube (ROI 4). Indeed, the mean absolute differences between approaches weres 1.4±1.9%, 13.1±4.7 s^{-1}, 0.55±1.39 s^{-1}, and 1.4±1.1 s^{-1} for PDFF, R_2^*, R_{1f}, R_{1w} respectively. This corresponds to relative differences of 20±19%, 25±12%, 15±42%, and 34±25%. It should be noted that while the R_1 of fat and water return a relatively consistent bias between techniques, the difference in R_2^* values is greatest for the 50% and 60% nominal fat fraction ROIs. The dispersion of the voxel-wise multiparametric fit results are displayed in Figure 3.4. ROIs are shown in Figure 3.1.a.

PDFF estimates were significantly different from the reference measurement for both Fat DESPOT techniques. However, the absolute error for both approaches was below 5% for

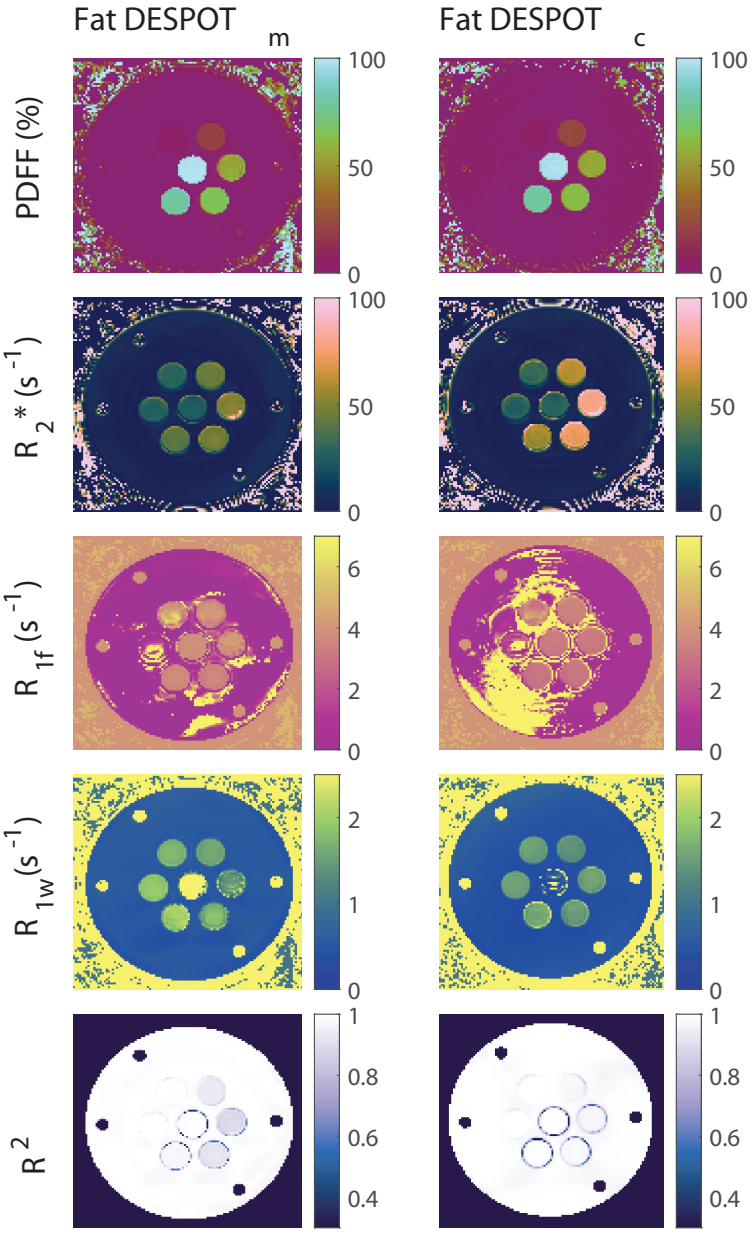

Figure 3.3: Multiparametric maps for PDFF, R_2^*, R_{1f}, R_{1w}, and R2 using the complex and magnitude approaches to Fat DESPOT. To reduce noise in the R_{1f} image, voxels with PDFF<3% were masked. All images are displayed with perceptually uniform colour maps from the crameri library [28, 29].

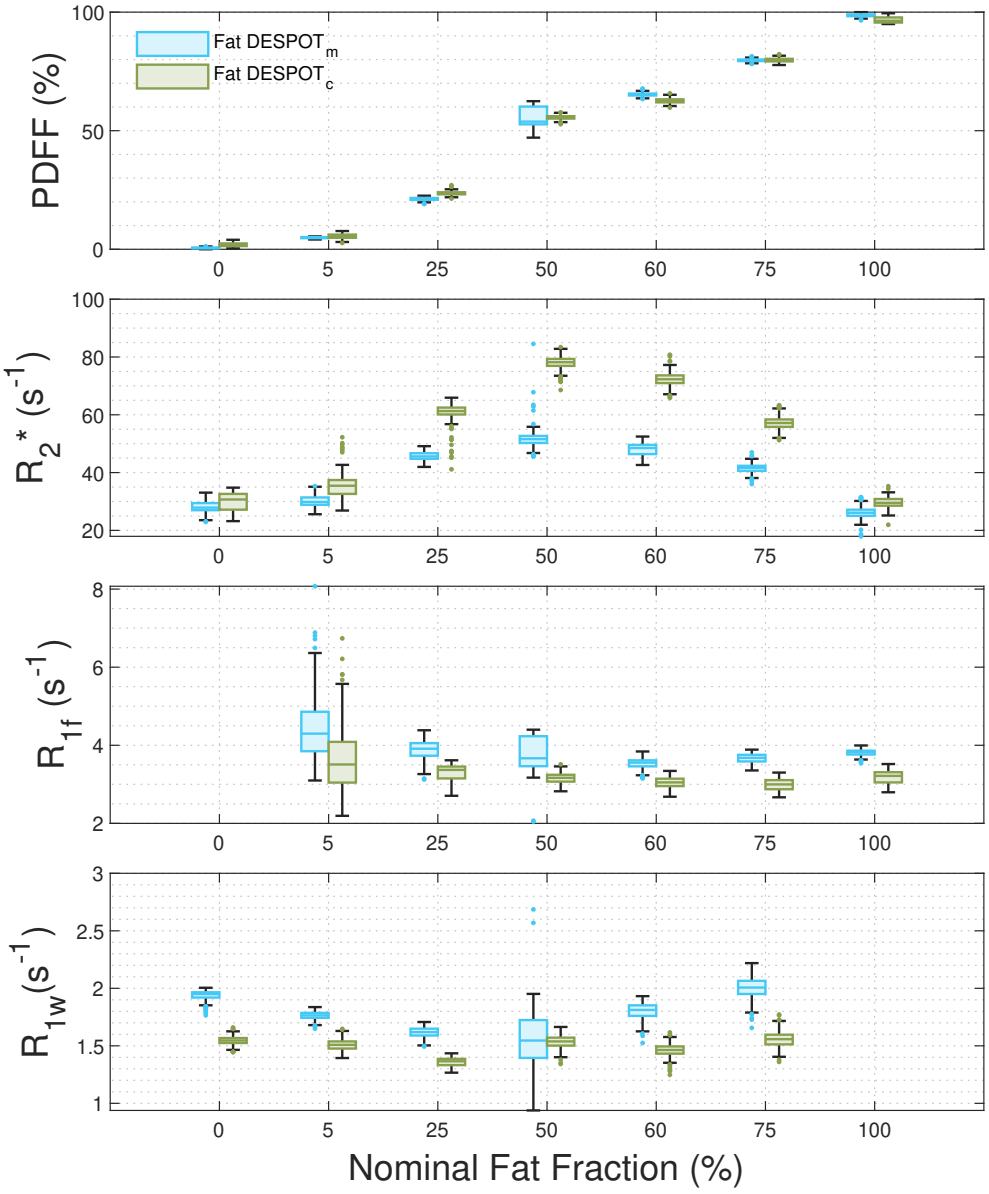

Figure 3.4: Distribution of voxel-wise estimates of PDFF, R_2^*, R_{1f}, and R_{1w}, using the complex and magnitude approaches to Fat DESPOT. Box = interquartile range, horizontal line = median, feathers= data range, dots= outliers. Fat DESPOT $_m$ and Fat DESPOT$_c$ return significantly different parametric estimates ($p<0.05$), excluding PDFF in ROI 6 and R_{1w} in ROI 4. All inter-group variances are significantly different ($p<0.05$) excluding R_2^* in the 100% nominal fat fraction tube, R_{1f} in the 5% and 60% nominal fat fraction tubes, and R_{1w} in 10% nominal fat fraction tube.

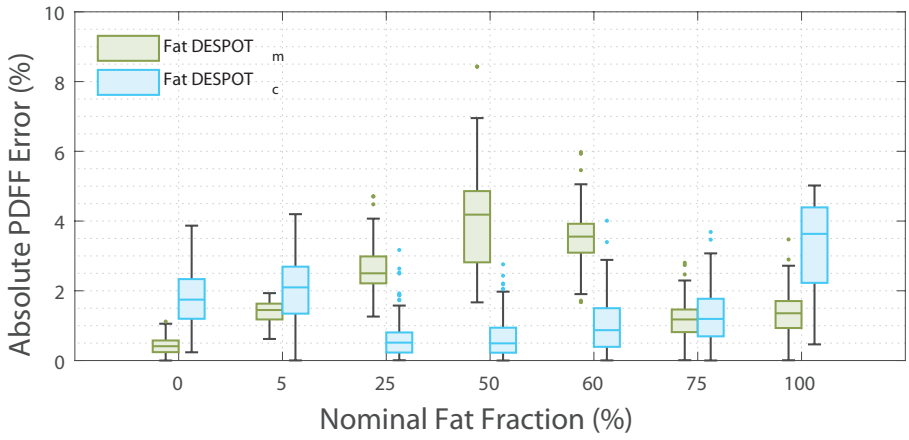

Figure 3.5: Distribution of the absolute error on the PDFF using the complex and magnitude Fat DESPOT approaches compared to a reference measurement. Box = interquartile range, horizontal line = median, feathers= data range, dots= outliers. Error is significantly different ($p<0.05$) between approaches in all ROIs excluding the 75% nominal fat fraction.

all measurements (figure 3.5). This being said, Fat DESPOT$_m$ and Fat DESPOT$_c$ returned significantly different PDFF absolute error values ($p<0.05$) for all ROIs excluding the 75% nominal fat fraction. Fat DESPOT$_m$ exhibited a higher mean absolute error of 2.1±1.4% compared to 1.5±1.2% for Fat DESPOT$_c$.

Overall, Fat DESPOT$_c$ results in higher precision measurements for PDFF, R_{1f}, and R_{1w}, and a smaller range of standard deviations across all Fat DESPOT output parameters compared to Fat DEPSOT$_m$, suggesting an overall more precise and stable fit. Indeed, standard deviations were significantly different between Fat DESPOT approaches ($p<0.05$) for all ROIs excluding R_2^* in the 100% nominal fat fraction tube (ROI 7), R_{1f} in the 5% and

Approach	Fat DESPOt$_m$		Fat DESPOT$_c$	
Parameter	Mean	Range	Mean	Range
PDFF (%)	0.27	3.8	0.015	0.29
R_2^* (s−1)	0.35	2.9	0.47	2.1
R_{1f} (s^{-1})	0.060	3.0	0.052	2.8
R_{1w} (s^{-1})	0.016	0.26	0.0070	0.040

Table 3.5: The mean and range of the standard deviations of Fat DESPOT$_m$ and Fat DESPOT$_c$ across ROIs 1-7 in the variable fat fraction phantom, assessing the stability of multiparametric fits across PDFF 0-100%.

50% nominal fat fraction tubes (ROI 2 and ROI 5), and R_{1w} in the 0% nominal fat fraction tube (ROI 1). The standard deviation of R_{1f} increases significantly for both approaches to Fat DESPOT in the tube with a nominal fat fraction of 5% (ROI 6), agreeing with simulations that show a loss of precision at low-fat fractions. A summary of mean standard deviations and standard deviation ranges is displayed in table 3.5.

In vivo results

In vivo Fat DESPOT$_m$ and Fat DESPOT$_c$ multiparametric maps of the lower leg (3.6) display key anatomical features, including the muscle, bone marrow from the tibia, the fibula, and the subcutaneous fat layer with distinct combinations of Fat DESPOT output values. A gradient artifact is visible in the R_{1w} maps of both Fat DESPOT$_m$ and Fat DESPOT$_c$. This artifact is likely due to the lack of image uniformity corrections in this in vivo dataset.

As was the case in the phantom, while both approaches returned high-quality fits, Fat

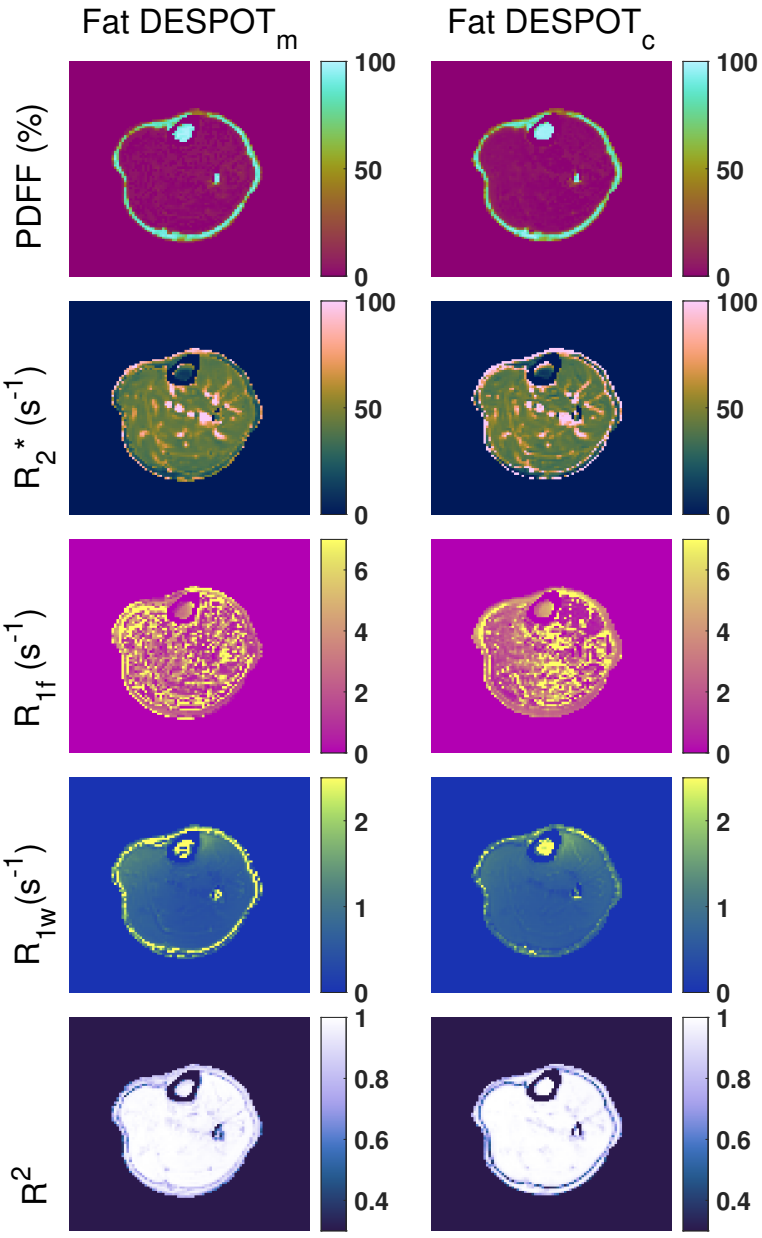

Figure 3.6: Multiparametric maps of a cross-section of the lower leg for PDFF, R2*, R1f, R1w, and R2 using the complex and magnitude approaches to Fat DESPOT. To reduce noise in the R_{1f} image, voxels with PDFF<2% were masked. All images are displayed with perceptually uniform colour maps from the crameri library [28, 29].

DESPOT$_c$ performed better with average R^2 above 0.92 compared to 0.88 for Fat DESPOT$_m$. The two approaches to Fat DESPOT returned significantly different parametric estimates ($p<0.05$) with the exception of R_2^* for muscle, PDFF in all tissues. PDFF showed the best agreement between approaches on average across all regions of interest. Here, muscle has the highest relative difference in PDFF where Fat DESPOT$_m$ estimated 2.8% and Fat DESPOT$_c$ estimated 1.8%, an absolute difference of only 1±1.6%, but a relative difference of 42±140%. Though precision for both techniques is low, on average, Fat DESPOT$_c$ has a higher precision for R_2^*, R_{1f}, and R_{1w}, while the mean precision of both techniques was equal for PDFF. Specifically, mean standard deviations were 0.73% 2.1 s^{-1}, 1.4 s^{-1}, and 0.37 s^{-1} for PDFF, R_2*, R_{1f}, and R_{1w} respectively with Fat DESPOT$_m$ and 0.73%, 1.6 s^{-1}, 1.2 s^{-1} and 0.23 s^{-1} for the same parameters with Fat DESPOT$_c$,. The mean value and standard deviation of Fat DESPOT output parameters are displayed in table 3.6, along with the percent difference between techniques.

Discussion

While reducing imaging time by approximately 30%, Fat DEPOT$_c$ generally returned parametric estimates with higher precision, accuracy, and stability over a range of fat fractions than Fat DESPOT$_m$. In phantoms, Fat DESPOT$_c$ had a smaller mean error on PDFF, a smaller mean standard deviation for PDFF, R_{1f}, and R_{1w} and a smaller range of standard deviation on all parameters, suggesting greater stability of fits across fat

ROI	Parameter	Mean(±*std.*)		% Difference (±*std.*)
		Fat DESPOT$_m$	Fat DESPOT$_c$	
Bone Marrow	PDFF (%)	94(±6)	95(±4)	2(±10)
# Voxels =143	R_2^* (s^{-1})	34(±25)	47(±4)	33(±221)*
	R_{1f} (s^{-1})	2.9(±1.4)	3.8(±1.3)	26.49(±83.29)*
	R_{1w} (s^{-1})	4.8(±4.0)	3.5(±2.5)	33(±64)*
	R^2	0.88(±0.27)	0.92(±0.18)	–
Muscle	PDFF (%)	2.8(±2.0)	1.8(±1.2)	42(±140)
# Voxels =243	R_2^* (s^{-1})	46(±10)	46(±9)	1.4(±43.2)
	R_{1f} (s^{-1})	1.1(±0.7)	1.7(±0.8)	43(±99)*
	R_{1w} (s^{-1})	0.49(±0.05)	0.59(±0.03)	18(±1)*
	R^2	0.99(±0.0069)	0.99(±0.007)	–
Subcutaneous fat	PDFF (%)	85(±6)	86(±8)	0.42(±16.93)
# Voxels =150	R_2^* (s^{-1})	26(±13)	21(±18)	21(±13)*
	R_{1f} (s^{-1})	2.3(±0.6)	2.6(±0.5)	11(±4)*
	R_{1w} (s^{-1})	1.9(±2.0)	1.3(±1.2)	39(±199)*
	R^2	0.88(±0.27)	0.92(±0.18)	–

Table 3.6: Mean value and relative difference of Fat DESPOT$_c$ and Fat DESPOT$_m$ output parameters PDFF, R_2*, R_{1f}, and R_{1w} and mean R^2 for ROIs in the subcutaneous fat, bone marrow, and muscle of a human lower leg. The asterix designates a significant difference ($p<0.05$)

fractions. In vivo, Fat DESPOT$_c$ returned smaller standard deviations in nearly all instances, while returning parameter estimates similar to published values.

In phantom, both Fat DESPOT PDFF estimates were highly accurate, with error $< 5\%$ using both approaches. Nonetheless, on average, Fat DESPOT$_c$ was more accurate than Fat DESPOT$_m$. *In vivo*, relative accuracy was difficult to assess, as measurements were very similar and a reference measurement was not taken. This said, both Fat DESPOT PDFF estimates were similar to published values, though slightly higher for bone marrow [30] and muscle [31, 32] and lower for subcutaneous fat [33, 34].

Comparison of the relaxation parameter values measured in phantom presented in this work with the literature is complicated by contradictory trends in prior publications, and few reports of both R_{1w} and R_{1f}. Indeed, some groups found that R_{1w} in gel phantoms was independent of fat fractions [35, 36], a behaviour consistent with our observations. Others, however, found that both R_{1f} and R_{1w} were fat fraction dependant [37]. However, measurement approach and phantom construction, including the use of agar or agarose and their respective concentrations, vary between studies, making comparison difficult.

In vivo measurements were further challenged by a lack of literature specific to our anatomical region for imaging and inter-subject variations. This said, R_{1f} estimated with both approaches showed reasonable agreement with reports of bone marrow R_{1f} in the spine [10] and showed fairly good agreement with $R_{1global}$ estimates in subcutaneous fat [38, 39], which should be dominated by the fat signal. Our Fat DESPOT R_{1w} estimates

in bone marrow were larger than published values [10], but showed fairly good agreement with $R_{1global}$ in muscle, which should be dominated by the water signal [40, 41]. In the bone marrow, R_2^* estimates were markedly different between Fat DESPOT approaches and Fat DESPOT$_c$ agreed more closely with published values [42]. In muscle, Fat DESPOT$_m$ and Fat DESPOT$_c$ estimates of R_2^* were significantly higher than published values [41, 43], while they show fairly good agreement with published values of R_2^* for subcutaneous fat [44].

In phantoms and in vivo, Fat DESPOT$_m$ and Fat DESPOT$_c$ most often returned significantly different results. While there was no discernable trend to the difference in vivo, in phantom, Fat DESPOT$_c$ returned higher R_2^* and lower R_{1f} and R_{1w} compared to Fat DESPOT$_m$. Several factors may impact the accuracy of these two techniques and their agreement. First, due to sequence timing constraints, the TR for Fat DESPOT$_c$ is longer compared to Fat DESPOT$_m$, and echo times between approaches were also different. Imperfect refocusing or spoiling can cause the R_2^* decay curve to deviate from the expected exponential model. The effect of this deviation on the fit is in part dictated by TE and TR selection [45]. Likewise, in mixed fat-water voxels, the selection of echo times may impact fitting, as chemical-shift-based models rely on measuring the signal at several different relative phases [46]. Imperfect spoiling has also been shown to affect T$_1$ estimates in other VFA experiments and may affect estimates in the Fat DESPOT approach [47, 48]. Flip angles were also different between approaches, optimized for the highest precision given their respective TRs. The judicious selection of flip angles is key to T$_1$ fitting [21] and may

also introduce bias in one measurement relative to the other.

Simulations may also offer insights into the disagreement between approaches. Assigning different initial phases to the fat and water components of the simulated signal increased the error in the Fat DESPOT$_m$ measurement, by up to 40% in the case of R_{1f} and R_{1w}, peaking at intermediate fat fractions. In phantoms, R^2 values of the Fat DESPOT$_m$ fitting were lowest for intermediate fat fractions, suggesting that the model may be struggling to accommodate for a difference in the initial phase. R_2^*, which has the greatest difference in values between approaches at intermediate nominal frat fractions, may be absorbing some error due to phase differences in the Fat DESPOT$_m$ approach. The relative phase of fat and water may also be responsible for Fat DESPOT$_m$ having a lower precision than Fat DESPOT$_c$ in phantoms and in vivo, as initial phases were not constant across the imaged volume (FigureS1 of the supplementary materials).

Integrating the complex signal into the Fat DESPOT approach was expected to result in estimates of PDFF, R_2^*, R_{1w} and R_{1f} similar in precision and accuracy to the magnitude approach in a shorter scan time. Fat DESPOT$_c$ showed overall improvements in precision and accuracy. However, there are some remaining limitations to Fat DESPOT. Notably, both approaches to Fat DESPOT appear vulnerable to B_0 field inhomogeneity artifacts and effects from the lack of non-uniformity correction. To reduce these issues, alternative initial parameter estimation techniques could be explored and uniformity corrections should be included in future measurements. Acquisition time remains a disadvantage in

this implementation of the Fat DESPOT approach. However, all acquisitions in this work used 8 signal averages and no parallel imaging. Fat DESPOT has been found to perform well at an SNR above 63 [1]. Reduction of the number of averages, while keeping above this SNR threshold will allow for gains in the acquisition time without reduced fit quality. Furthermore, the number of FAs acquired and used in the fitting algorithm could be reduced [1]. Finally, while the lower leg provided a straightforward site for the initial comparison of approaches in vivo, a further comparison should be conducted in sites with a broader diversity of tissues, such as the abdomen, where the liver is of particular interest, given the emerging role of multiparametric mapping in the diagnosis of liver disease [4, 5]. This potential application will require careful consideration of motion issues.

Conclusion

The complex approach to Fat DESPOT offers higher precision and accuracy for phantom and in vivo measurements. Furthermore, the time gains obtained by using the complex approach reduce the risk of motion artifacts and increase the feasible FOV or resolution of images. Hence, the complex approach to Fat DESPOT represents a valuable advancement for multiparametric mapping with potential applications in fatty liver disease, and solid tumour imaging, where measures of R_2*, PDFF, and R_1 are of particular value.

Acknowledgements

The authors acknowledge the developers of the ISMRM fat-water toolbox (http://www.ismrm.org/workshops/FatWater12/data.htm), Norma Ybarra for technical assistance in phantom building and the MR Methods Research Group (McGill University) for useful discussion. This work was funded by the Research Institute of the McGill University Health Centre, the *Fond de Recherche Québec - Santé* (FRQS), and a Discovery Grant from the Natural Sciences and Engineering Research Council of Canada (NSERC). RC Bider acknowledges support from NSERC (CGS-M award).

Supporting Figures and Tables

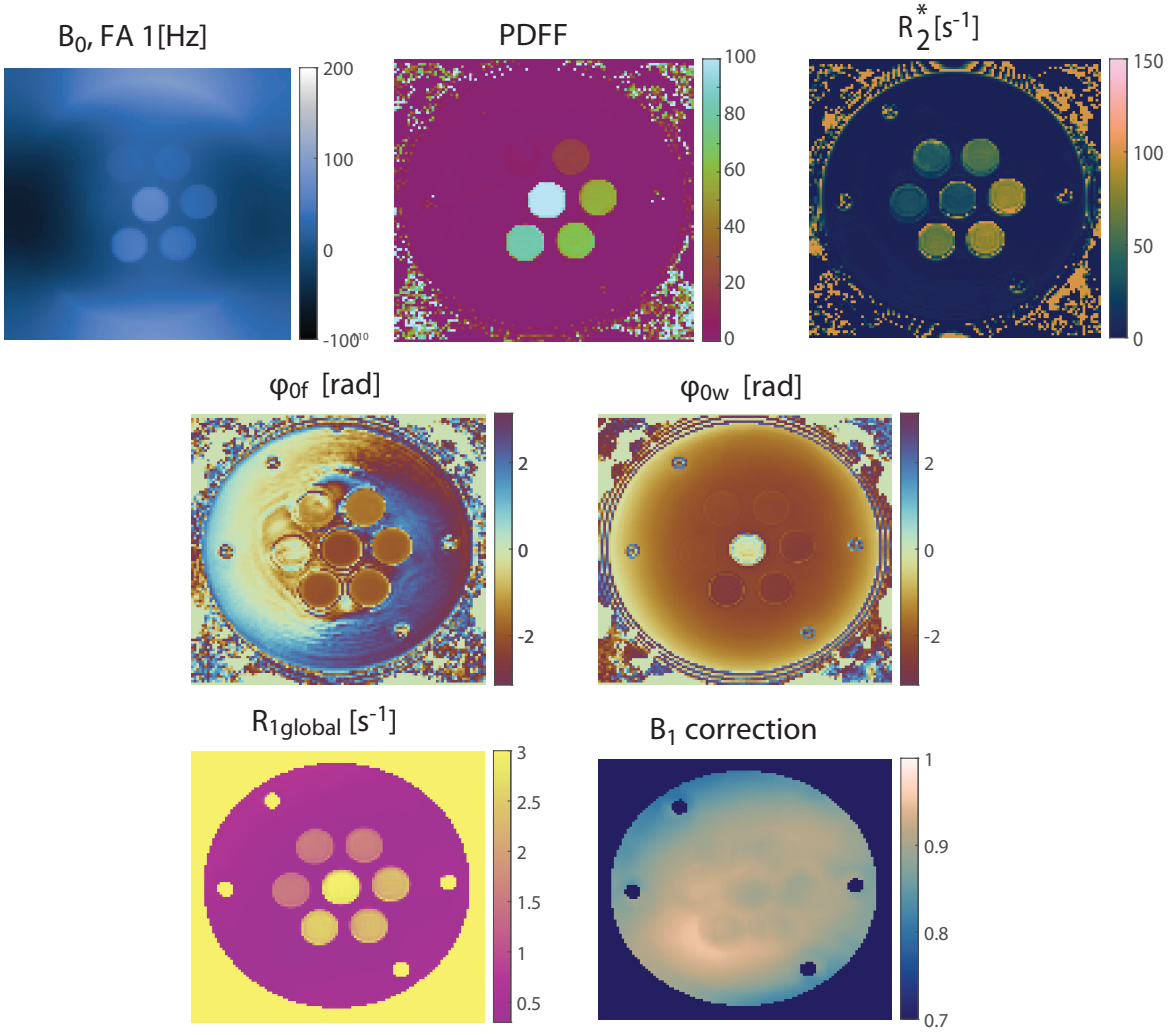

Figure S1: Examples of initial guess maps for the variable fat fraction phantom (8-echo acquisition) and of the B_1 correction map. Estimates from the upper and lower rows were obtained from the Graph Cut algorithm. The displayed B_0 map is for the first Flip angle (3°) The B_1 map was obtained from a 2-angle B_1 estimation and $R_{1global}$ map was obtained from a DESPOT$_1$ algorithm on the lower left. All images are displayed with perceptually uniform colour maps from the crameri library [28, 29]

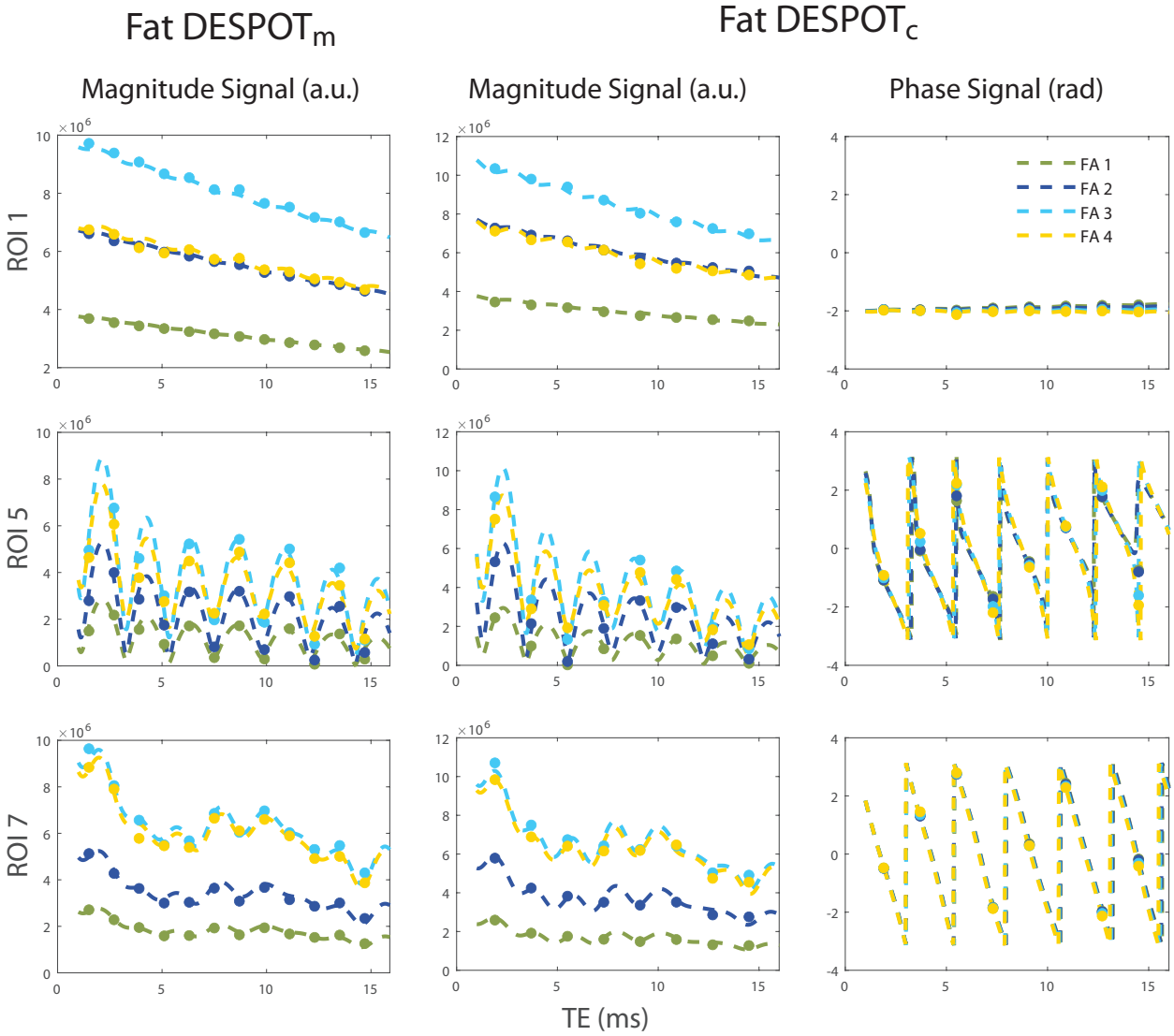

Figure S2: Examples of voxel-wise fits for the central pixel of each ROI in the variable fat fraction phantom. The left column shows the magnitude of the mGRE data (points) and the Fat DESPOT$_m$ fits (dashed line). The central column and right column show the magnitude of the mGRE data (points) and the Fat DESPOT$_c$ fit, and the phase of the mGRE data(points) and the Fat DESPOT$_c$ fit respectively. Flip angles 1-4 are 3°, 6°, 15° and 34° respectively for Fat DESPOT$_m$ and 3°, 7°, 19° and 45° for Fat DESPOT$_c$.

Bibliography

[1] V. Fortier and I. R. Levesque, "MR-oximetry with fat DESPOT," *Magnetic Resonance Imaging*, vol. 97, pp. 112–121, Apr. 2023.

[2] C. D. Pfeifer, B. P. Schoennagel, R. Grosse, Z. J. Wang, J. Graessner, P. Nielsen, G. Adam, R. Fischer, and J. Yamamura, "Pancreatic iron and fat assessment by MRI-R2* in patients with iron overload diseases," *Journal of Magnetic Resonance Imaging*, vol. 42, no. 1, pp. 196–203, 2015. _eprint: https://onlinelibrary.wiley.com/doi/pdf/10.1002/jmri.24752.

[3] M. F. Santarelli, A. Meloni, D. De Marchi, L. Pistoia, A. Quarta, A. Spasiano, L. Landini, A. Pepe, and V. Positano, "Estimation of pancreatic R2* for iron overload assessment in the presence of fat: a comparison of different approaches," *Magnetic Resonance Materials in Physics, Biology and Medicine*, vol. 31, pp. 757–769, Dec. 2018.

[4] J. J. Schaapman, M. E. Tushuizen, M. J. Coenraad, and H. J. Lamb, "Multiparametric MRI in Patients With Nonalcoholic Fatty Liver Disease," *Journal of Magnetic Resonance Imaging*, vol. 53, no. 6, pp. 1623–1631, 2021. _eprint: https://onlinelibrary.wiley.com/doi/pdf/10.1002/jmri.27292.

[5] R. Banerjee, M. Pavlides, E. M. Tunnicliffe, S. K. Piechnik, N. Sarania, R. Philips, J. D. Collier, J. C. Booth, J. E. Schneider, L. M. Wang, D. W. Delaney, K. A. Fleming, M. D. Robson, E. Barnes, and S. Neubauer, "Multiparametric magnetic resonance for

the non-invasive diagnosis of liver disease," *Journal of Hepatology*, vol. 60, pp. 69–77, Jan. 2014.

[6] M. Pavlides, R. Banerjee, J. Sellwood, C. J. Kelly, M. D. Robson, J. C. Booth, J. Collier, S. Neubauer, and E. Barnes, "Multiparametric magnetic resonance imaging predicts clinical outcomes in patients with chronic liver disease," *Journal of Hepatology*, vol. 64, pp. 308–315, Feb. 2016.

[7] O. Jaubert, C. Arrieta, G. Cruz, A. Bustin, T. Schneider, G. Georgiopoulos, P.-G. Masci, C. Sing-Long, R. M. Botnar, and C. Prieto, "Multi-parametric liver tissue characterization using MR fingerprinting: Simultaneous T1, T2, T2*, and fat fraction mapping," *Magnetic Resonance in Medicine*, vol. 84, no. 5, pp. 2625–2635, 2020. _eprint: https://onlinelibrary.wiley.com/doi/pdf/10.1002/mrm.28311.

[8] T. J. Arai, D. M. Yang, J. W. Campbell, T. Chiu, X. Cheng, S. Stojadinovic, P. Peschke, and R. P. Mason, "Oxygen-Sensitive MRI: A Predictive Imaging Biomarker for Tumor Radiation Response?," *International journal of radiation oncology, biology, physics*, vol. 110, pp. 1519–1529, Aug. 2021.

[9] C. Le Ster, J. Lasbleiz, S. Kannengiesser, R. Guillin, G. Gambarota, and H. Saint-Jalmes, "A fast method for the quantification of fat fraction and relaxation times: Comparison of five sites of bone marrow," *Magnetic Resonance Imaging*, vol. 39, pp. 157–161, June 2017.

[10] C. Le Ster, G. Gambarota, J. Lasbleiz, R. Guillin, O. Decaux, and H. Saint-Jalmes, "Breath-hold MR measurements of fat fraction, T1, and T2* of water and fat in vertebral bone marrow," *Journal of Magnetic Resonance Imaging*, vol. 44, no. 3, pp. 549–555, 2016. _eprint: https://onlinelibrary.wiley.com/doi/pdf/10.1002/jmri.25205.

[11] Q. Wan, H. Peng, J. Lyu, F. Liu, C. Chuanli, Y. Qiao, J. Deng, H. Zheng, Y. Wang, C. Zou, and X. Liu, "Water Specific MRI T1 Mapping for Evaluating Liver Inflammation Activity Grades in Rats With Methionine-Choline-Deficient Diet-Induced Nonalcoholic Fatty Liver Disease," *Journal of Magnetic Resonance Imaging*, vol. 56, Feb. 2022.

[12] F. C. Michelotti, Y. Kupriyanova, T. Mori, T. Küstner, G. Heilmann, M. Bombrich, C. Möser, M. Schön, O. Kuss, M. Roden, and V. B. Schrauwen-Hinderling, "An Empirical Approach to Derive Water T1 from Multiparametric MR Images Using an Automated Pipeline and Comparison With Liver Stiffness," *Journal of Magnetic Resonance Imaging*, vol. 59, no. 4, pp. 1193–1203, 2024. _eprint: https://onlinelibrary.wiley.com/doi/pdf/10.1002/jmri.28906.

[13] F. Colliez, M.-A. Neveu, J. Magat, T. T. Cao Pham, B. Gallez, and B. F. Jordan, "Qualification of a Noninvasive Magnetic Resonance Imaging Biomarker to Assess Tumor Oxygenation," *Clinical Cancer Research*, vol. 20, pp. 5403–5411, Oct. 2014.

[14] D. Hernando, Z.-P. Liang, and P. Kellman, "Chemical shift–based water/fat separation: A comparison of signal models," *Magnetic*

Resonance in Medicine, vol. 64, no. 3, pp. 811–822, 2010. _eprint: https://onlinelibrary.wiley.com/doi/pdf/10.1002/mrm.22455.

[15] D. Hernando, C. D. G. Hines, H. Yu, and S. Reeder, "Addressing phase errors in fat-water imaging using a mixed magnitude/complex fitting method," *Magnetic Resonance in Medicine*, vol. 67, no. 3, pp. 638–644, 2012. _eprint: https://onlinelibrary.wiley.com/doi/pdf/10.1002/mrm.23044.

[16] X. Wang, T. J. Colgan, L. A. Hinshaw, N. T. Roberts, L. C. H. Bancroft, G. Hamilton, D. Hernando, and S. B. Reeder, "T1-Corrected Quantitative Chemical Shift Encoded Magnetic Resonance Imaging," *Magnetic resonance in medicine*, vol. 83, pp. 2051–2063, June 2020.

[17] D. P. O'Regan, M. F. Callaghan, M. Wylezinska-Arridge, J. Fitzpatrick, R. P. Naoumova, J. V. Hajnal, and S. A. Schmitz, "Liver Fat Content and T2*: Simultaneous Measurement by Using Breath-hold Multiecho MR Imaging at 3.0 T—Feasibility," *Radiology*, vol. 247, pp. 550–557, May 2008. Publisher: Radiological Society of North America.

[18] G. Hamilton, M. S. Middleton, J. C. Hooker, W. M. Haufe, N. I. Forbang, M. A. Allison, R. Loomba, and C. B. Sirlin, "In vivo breath-hold 1H MRS simultaneous estimation of liver proton density fat fraction, and T1 and T2 of water and fat, with a multi-TR,

multi-TE sequence," *Journal of Magnetic Resonance Imaging*, vol. 42, no. 6, pp. 1538–1543, 2015. _eprint: https://onlinelibrary.wiley.com/doi/pdf/10.1002/jmri.24946.

[19] A. Triay Bagur, C. Hutton, B. Irving, M. L. Gyngell, M. D. Robson, and M. Brady, "Magnitude-intrinsic water–fat ambiguity can be resolved with multipeak fat modeling and a multipoint search method," *Magnetic Resonance in Medicine*, vol. 82, no. 1, pp. 460–475, 2019. _eprint: https://onlinelibrary.wiley.com/doi/pdf/10.1002/mrm.27728.

[20] C. Ciobanu, "Evaluation of complex fitting for longitudinal relaxation mapping in fat with magnetic resonance imaging," 2022. Publisher: McGill University.

[21] S. C. Deoni, B. K. Rutt, and T. M. Peters, "Rapid combined T1 and T2 mapping using gradient recalled acquisition in the steady state," *Magnetic Resonance in Medicine*, vol. 49, no. 3, pp. 515–526, 2003. _eprint: https://onlinelibrary.wiley.com/doi/pdf/10.1002/mrm.10407.

[22] H.-L. M. Cheng and G. A. Wright, "Rapid high-resolution T1 mapping by variable flip angles: Accurate and precise measurements in the presence of radiofrequency field inhomogeneity," *Magnetic Resonance in Medicine*, vol. 55, no. 3, pp. 566–574, 2006. _eprint: https://onlinelibrary.wiley.com/doi/pdf/10.1002/mrm.20791.

[23] E. C. Bush, A. Gifford, C. L. Coolbaugh, T. F. Towse, B. M. Damon, and E. B. Welch, "Fat-Water Phantoms for Magnetic Resonance Imaging Validation: A Flexible and Scalable Protocol," *Journal of Visualized Experiments : JoVE*, p. 57704, Sept. 2018.

[24] Q. Duan, J. H. Duyn, N. Gudino, J. A. d. Zwart, P. v. Gelderen, D. K. Sodickson, and R. Brown, "Characterization of a dielectric phantom for high-field magnetic resonance imaging applications," *Medical Physics*, vol. 41, Oct. 2014. Publisher: American Association of Physicists in Medicine.

[25] F. Franconi, L. Lemaire, H. Saint-Jalmes, and P. Saulnier, "Tissue oxygenation mapping by combined chemical shift and T1 magnetic resonance imaging," *Magnetic Resonance in Medicine*, vol. 79, no. 4, pp. 1981–1991, 2018. _eprint: https://onlinelibrary.wiley.com/doi/pdf/10.1002/mrm.26857.

[26] M. Boudreau, C. L. Tardif, N. Stikov, J. G. Sled, W. Lee, and G. B. Pike, "B1 mapping for bias-correction in quantitative T1 imaging of the brain at 3T using standard pulse sequences," *Journal of Magnetic Resonance Imaging*, vol. 46, no. 6, pp. 1673–1682, 2017. _eprint: https://onlinelibrary.wiley.com/doi/pdf/10.1002/jmri.25692.

[27] W. T. Triplett, C. Baligand, S. C. Forbes, R. J. Willcocks, D. J. Lott, S. DeVos, J. Pollaro, W. D. Rooney, H. L. Sweeney, C. G. Bönnemann, D.-J. Wang, K. Vandenborne, and G. A. Walter, "Chemical shift-based MRI to measure fat fractions

in dystrophic skeletal muscle," *Magnetic Resonance in Medicine*, vol. 72, no. 1, pp. 8–19, 2014. _eprint: https://onlinelibrary.wiley.com/doi/pdf/10.1002/mrm.24917.

[28] C. Green, "Crameri perceptually uniform scientific colormaps," 2022.

[29] F. Crameri, "Geodynamic diagnostics, scientific visualisation and StagLab 3.0," *Geoscientific Model Development*, vol. 11, pp. 2541–2562, June 2018. Publisher: Copernicus GmbH.

[30] C. M. J. de Bazelaire, G. D. Duhamel, N. M. Rofsky, and D. C. Alsop, "MR Imaging Relaxation Times of Abdominal and Pelvic Tissues Measured in Vivo at 3.0 T: Preliminary Results," *Radiology*, vol. 230, pp. 652–659, Mar. 2004. Publisher: Radiological Society of North America.

[31] A. Fischmann, S. Kaspar, J. Reinhardt, M. Gloor, C. Stippich, and D. Fischer, "Exercise might bias skeletal-muscle fat fraction calculation from Dixon images," *Neuromuscular Disorders*, vol. 22, pp. S107–S110, Oct. 2012.

[32] M. A. Fischer, C. W. A. Pfirrmann, N. Espinosa, D. A. Raptis, and F. M. Buck, "Dixon-based MRI for assessment of muscle-fat content in phantoms, healthy volunteers and patients with achillodynia: comparison to visual assessment of calf muscle quality," *European Radiology*, vol. 24, pp. 1366–1375, June 2014.

[33] C. Held, D. Junker, M. Wu, L. Patzelt, L. A. Mengel, C. Holzapfel, M. N. Diefenbach, M. R. Makowski, H. Hauner, and D. C. Karampinos, "Intraindividual difference between supraclavicular and subcutaneous proton density fat fraction is associated with cold-induced thermogenesis," *Quantitative Imaging in Medicine and Surgery*, vol. 12, pp. 2877–2890, May 2022.

[34] D. Franz, D. Weidlich, F. Freitag, C. Holzapfel, T. Drabsch, T. Baum, H. Eggers, A. Witte, E. J. Rummeny, H. Hauner, and D. C. Karampinos, "Association of proton density fat fraction in adipose tissue with imaging-based and anthropometric obesity markers in adults," *International Journal of Obesity*, vol. 42, pp. 175–182, Feb. 2018.

[35] N. T. Roberts, D. Tamada, Y. Muslu, D. Hernando, and S. B. Reeder, "Confounder-corrected T1 mapping in the liver through simultaneous estimation of T1, PDFF, R2*, and B1+ in a single breath-hold acquisition," *Magnetic Resonance in Medicine*, vol. 89, no. 6, pp. 2186–2203, 2023. _eprint: https://onlinelibrary.wiley.com/doi/pdf/10.1002/mrm.29590.

[36] L. D. Garrison, C. Levick, M. Pavlides, T. Marjot, F. Mozes, L. Hodson, S. Neubauer, M. D. Robson, and C. T. Rodgers, "Water-Only Look-Locker Inversion recovery (WOLLI) T1 mapping," Jan. 2022. Pages: 2022.01.28.478209 Section: New Results.

[37] H. H. Hu and K. S. Nayak, "Change in the proton T1 of fat and water in mixture," *Magnetic Resonance in Medicine*, vol. 63, no. 2, pp. 494–501, 2010. _eprint:

https://onlinelibrary.wiley.com/doi/pdf/10.1002/mrm.22205.

[38] J. P. O'Connor, J. H. Naish, A. Jackson, J. C. Waterton, Y. Watson, S. Cheung, D. L. Buckley, D. M. McGrath, G. A. Buonaccorsi, S. J. Mills, C. Roberts, G. C. Jayson, and G. J. Parker, "Comparison of normal tissue R1 and R modulation by oxygen and carbogen," *Magnetic Resonance in Medicine*, vol. 61, no. 1, pp. 75–83, 2009. _eprint: https://onlinelibrary.wiley.com/doi/pdf/10.1002/mrm.21815.

[39] E. Tadamura, H. Hatabu, W. Li, P. V. Prasad, and R. R. Edelman, "Effect of oxygen inhalation on relaxation times in various tissues," *Journal of Magnetic Resonance Imaging*, vol. 7, no. 1, pp. 220–225, 1997. _eprint: https://onlinelibrary.wiley.com/doi/pdf/10.1002/jmri.1880070134.

[40] G. E. Gold, E. Han, J. Stainsby, G. Wright, J. Brittain, and C. Beaulieu, "Musculoskeletal MRI at 3.0 T: Relaxation Times and Image Contrast," *American Journal of Roentgenology*, vol. 183, pp. 343–351, Aug. 2004. Publisher: American Roentgen Ray Society.

[41] Y. Ding, R. P. Mason, R. W. McColl, Q. Yuan, R. R. Hallac, R. D. Sims, and P. T. Weatherall, "Simultaneous measurement of tissue oxygen level-dependent (TOLD) and blood oxygenation level-dependent (BOLD) effects in abdominal tissue oxygenation level studies," *Journal of Magnetic Resonance Imaging*, vol. 38, no. 5, pp. 1230–1236, 2013. _eprint: https://onlinelibrary.wiley.com/doi/pdf/10.1002/jmri.24006.

[42] A. Meloni, L. Pistoia, G. Restaino, M. Missere, V. Positano, A. Spasiano, T. Casini, A. Cossu, L. Cuccia, A. Massa, F. Massei, and F. Cademartiri, "Quantitative T2* MRI for bone marrow iron overload: normal reference values and assessment in thalassemia major patients," *La radiologia medica*, vol. 127, pp. 1199–1208, Nov. 2022.

[43] C. Zaeske, G.-P. Brueggemann, S. Willwacher, D. Maehlich, D. Maintz, and G. Bratke, "The behaviour of T2* and T2 relaxation time in extrinsic foot muscles under continuous exercise: A prospective analysis during extended running," *PLoS ONE*, vol. 17, p. e0264066, Feb. 2022.

[44] H. Yu, A. Shimakawa, C. A. McKenzie, E. Brodsky, J. H. Brittain, and S. B. Reeder, "Multi-Echo Water-Fat Separation and Simultaneous R2* Estimation with Multi-Frequency Fat Spectrum Modeling," *Magnetic resonance in medicine : official journal of the Society of Magnetic Resonance in Medicine / Society of Magnetic Resonance in Medicine*, vol. 60, pp. 1122–1134, Nov. 2008.

[45] R. D. Dortch, "Quantitative T2 and T2* Mapping," in *Advances in Magnetic Resonance Technology and Applications*, vol. 1, pp. 47–64, Elsevier, 2020.

[46] J. Berglund, L. Johansson, H. Ahlström, and J. Kullberg, "Three-point dixon method enables whole-body water and fat imaging of obese subjects," *Magnetic Resonance in Medicine*, vol. 63, no. 6, pp. 1659–1668, 2010. _eprint: https://onlinelibrary.wiley.com/doi/pdf/10.1002/mrm.22385.

[47] C. Preibisch and R. Deichmann, "Influence of RF spoiling on the stability and accuracy of T1 mapping based on spoiled FLASH with varying flip angles," *Magnetic Resonance in Medicine*, vol. 61, no. 1, pp. 125–135, 2009. _eprint: https://onlinelibrary.wiley.com/doi/pdf/10.1002/mrm.21776.

[48] N. Stikov, M. Boudreau, I. R. Levesque, C. L. Tardif, J. K. Barral, and G. B. Pike, "On the accuracy of T1 mapping: Searching for common ground," *Magnetic Resonance in Medicine*, vol. 73, no. 2, pp. 514–522, 2015. _eprint: https://onlinelibrary.wiley.com/doi/pdf/10.1002/mrm.25135.

Chapter 4

Discussion

Results presented in the methods section of Chapter 3 suggest that Fat DESPOT$_c$ is a promising candidate for multiparametric mapping, increasing precision and accuracy compared to Fat DESPOT$_m$ while offering the potential for shorter acquisition times or increased FOV or resolution within a clinically acceptable time frame. The increased performance of Fat DESPOT$_c$ compared to Fat DESPOT$_m$ also has implications for the feasibility of Fat DESPOT as a tool for MR oximetry. Indeed, measurement precision contributes to the achievable sensitivity of the technique, while acquisition time, FOV, and resolution have implications for the patient experience and the type of tumour that can be investigated.

4.1 Fat DESPOT Precision and MR Oximetry

The sensitivity of Fat DESPOT approaches to oxygen-induced changes in R_1 and R_2^* depends on measurement precision. For a carbogen gas challenge on a variety in murine prolactinomas and human PC3 prostate xenografts, Burrell *et al.* noted a change in R_2^* on the order of 100 s^{-1} for R_2^* and 0.3 s^{-1} for $R_{1global}$ for responsive tissue [66]. Studying response to an oxygen challenge in a murine renal cell carcinoma model, Little *et al.*, noted a change in R_2^* up to 40 s^{-1} and in R_1 up to 0.5 s^{-1} in responsive areas and a change in R_2^* up to -80 s^{-1} and in R_1 up to -0.1 s^{-1} in unresponsive tissue [67]. In murine xenografts of glioblastoma and non-small cell lung cancer, Featherstone *et al.* created voxel clusters based on R_1 responsiveness to an oxygen challenge, which they associated with different levels of hypoxia. These clusters were differentiated by $\Delta R_{1global}$ differences between 0.2 and 0.4 s^{-1} [83]. While results vary widely from study to study, likely in part due to different cancer models being studied and gas challenge implementation, they suggest a conservative estimate of the expected change in relaxation rate in response to a gas challenge around 50 s^{-1} for R_2^* and on the order of 0.2 s^{-1} for R_1. These expected changes can guide our estimate of the necessary precision for Fat DESPOT.

Power analysis provides a measure of the required sample size to detect a change given a desired level of significance. In our case this would correspond to a minimum number of voxels to determine whether a change in R_2^*, R_{1f} or R_{1w} has occcured in response to an oxygen challenge. To measure a change in a single voxel, the sample size from the power analysis

could guide the minimum number of repetitions required. A power analysis was conducted assuming a 95% confidence that a change on the order of the previously mentioned estimates can been detected (using the function *sampsizepwr*, MATLAB 2023, with default parameters and power=0.95). In phantom, the maximum standard deviation of R_2^* was 3.88 s^{-1} for Fat DESPOT$_m$ and 3.79 s^{-1} for Fat DESPOT$_c$. Detection of 50 s^{-1} change in R_2^* would require a sample size of 3 for Fat DESPOT$_m$ and Fat DESPOT$_c$. The same analysis to detect a change of 0.2 s^{-1} for R_{1w}, for the maximum standard deviation of R_{1w} (0.09 s^{-1} for Fat DESPOT$_m$ and 0.071 s^{-1} for Fat DESPOT$_c$) returns a sample size of 5 for both approaches. For R_{1f}, the largest standard deviation was 3.57 s^{-1} for Fat DESPOT$_m$ and 2.86 s^{-1} for Fat DESPOT$_c$ corresponding to the 5% fat fraction vial. Detecting a change of 0.2 s^{-1} for R_{1f}, would require a sample size of 4143 and 2660 for Fat DESPOT$_m$ and Fat DESPOT$_c$, far beyond a reasonable sample size for our measurements. However, the standard deviation for R_{1f} is much higher for the 5% nominal fat fraction vial than the others. Taking the second-largest standard deviation for each approach (0.80 s^{-1} for Fat DESPOT$_m$ and 0.79 s^{-1} for Fat DESPOT$_c$) returns a much smaller sample size of 210 and 205 for Fat DESPOT$_m$ and Fat DESPOT$_c$, respectively. While this sample size is still unreasonably large for repeat measurements or as a minimum detectable hypoxic volume, R_{1f} sensitivity to oxygen is greater than R_{1w} and $R_{1global}$ [23, 25], such that a lower precision is likely required.

These results suggest that R_2^* and R_{1w} obtained with both approaches to Fat DESPOT are reasonable for MR oximetry. They also suggest a PDFF threshold for MR oximetry

using R_{1f} between 5% and 25%, though additional measurements with fat fractions in this range and a comprehensive study of expected R_{1f} changes in response to a gas challenge in tumours would need to be completed to determine this limit.

While the phantom data suggests reasonable requirements for sample sizes in phantom, this is a highly simplified model and in vivo, standard deviations are larger for all measured tissues compared to phantom measurements. This is partly expected, given that tissue homogeneity in the ROI is difficult to achieve. Bone marrow is heterogeneously vascularized with a central arteriole surrounded by capillaries [84]. Likewise, while intermuscular fascia itself does not appear on MRI, it is often lined with a thin layer of fat which produces a signal [85] and is consistent with our observation of a "marbling" of the muscle with slightly elevated PDFF, elevated R_2^*, and lower R^2 (likely due to the fascia) in the multiparametric maps of the lower leg cross-section. The subcutaneous fat layer of the lower leg is relatively thin and fringe voxels likely contain partial volumes with surrounding muscular and epithelial tissues. These inhomogeneities likely increase the standard deviation of estimates in the bone marrow, muscle, and subcutaneous tissue ROI. Hence, they do not offer an accurate depiction of the expected precision of measurements in each voxel. This being said the smaller standard deviation of the Fat DESPOT$_c$ approach in most instances suggests that this technique would render more precise oximetry results.

To measure the true consistency of measurements and estimate the required sample size or repeat measurements for hypoxia measurements, several consecutive Fat DESPOT

measurements should be taken such that a voxel-specific standard deviation can be observed. Given published Fat DESPOT acquisition times, this has not been done so far but would be possible paired with acceleration techniques, such as those presented in the appendix section 6.3.

4.2 Acquisition time and feasibility of gas challenges

A typical gas challenge protocol includes one baseline measurement with the patient breathing room or medical air, exposure to a hyperoxic or hypoxic gas mixture for approximately 5 minutes to ensure an equilibrium pO_2 is reached [86], and a repeat measurement [87]. Hence, acquisition time is an important consideration as both measurements must fit within a clinically feasible time frame and exposure to gas mixtures with high or low oxygen should be limited. The Fat DESPOT$_m$ method as used in our previous publication and presented in this work, including B_1 mapping, takes 32.36 min, while our Fat DESPOT$_c$ protocol takes 25.2 min for a 192×192×100 mm^3 FOV, with 4.6 mins dedicated to B_1 mapping. Even if B_1 mapping was only completed once, this is well above reasonable measurement times. However, our group has explored several acceleration strategies to reduce acquisition time, namely reducing the number of signal averages (NSA) used and reducing the number of FAs (Véronique Fortier, PhD, personal communication).

The published measurement protocol involves taking 8 NSA for each acquisition. Taking a single signal average would reduce measurement time to 3.47 min for the magnitude approach

and 2.57 min for the complex approach, excluding B_1 mapping. This puts both approaches within a reasonable range for gas challenges. Furthermore, preliminary measurements using 1 NSA suggest that this does not reduce measurement precision, as demonstrated in Appendix 6.3, Figure 6.5. These shorter acquisition times also make breath-hold imaging for anatomies such as the liver realistic. Assuming a 20 s breath hold and the in-plane FOV and voxel size presented in the methods section of this work, 6 slices could be covered in a single breath-hold for Fat DESPOT$_m$ and 9 slices for Fat DESPOT$_c$. Parallel imaging could be used to decrease the scan time further, at a well-understood cost in SNR [88].

In Fat DESPOT, four FAs are measured to cover a range of R_1 values. Removing one FA acquisition reduces Fat DESPOT scan time by 25%. While angle selection affects bias in the resulting R_{1f} and R_{1w} measurement, Cheng *et al.* found that using three FAs maintained precision [89]. Fortier *et al.* showed good agreement between the 4 FA and 2 FA fat DESPOT R_1 values at a fat fraction above 25% for R_{1f} and all measured fat fractions for R_{1w}, while the 14% fat fraction measurement was biased [25]. A consistent bias will not likely affect measurements of ΔR_{1f} or ΔR_{1w} under a gas challenge. In preliminary measurements with Fat DESPOT$_c$, also in Appendix 6.3, Figure 6.5, reducing the measurement from 4 to 3 FAs (without re-optimization of the angles) again did not reduce precision.

The combined effect of removing signal averaging and one FA would result in Fat DESPOT$_m$ measurements taking 2.60 min and Fat DESPOT$_c$ measurements taking 1.92 min. Not only does this bring Fat DESPOT acquisition time into a realistic range for gas

challenges but it also opens the possibility for dynamic imaging where tumor hypoxia could be assessed at several time points in the gas challenge or during repeated gas challenges. Alternatively, a shorter acquisition per voxel allows for greater FOVs to be covered or increased resolution while staying within a clinically feasible imaging time. By this logic, the 30% time reduction of Fat DESPOT$_c$ compared to Fat DESPOT$_m$ can be translated to a 30% increase in FOV or resolution for the same imaging time.

Alternative B_1 mapping techniques could also be explored to further reduce acquisition time. Boudreau *et al.* obtain whole-brain coverage with and echo planar imaging double-angle (EPI-DA) approach with scan time below 2 minutes using standard available sequences [90]. Voltz *et al.* presented a FLASH-based B_1 mapping with whole brain coverage (FOV approximately 200×200×150 mm^3) with reasonable resolution in only 46 s [91]. A modified version of the saturation-prepared turbo FLASH (SatTFL) approach has also showed promise at 7 T with whole brain B_1 imaging in 20 s [92].

4.3 Potential applications of Fat DESPOT in hypoxia imaging

As discussed in section 2.1.4 of the background chapter of this thesis, hypoxia has been correlated with poor treatment outcomes in a number of cancers including those of the head and neck, breast , prostate , and pancreas , and metastatic liver tumours. Fat DESPOT R_{1f}

is of particular interest due to its increased sensitivity to oxygen changes compared to R_{1w} and $R_{1global}$ [23–25]. However, our simulation and phantom experiments suggest a steep loss of R_{1f} precision at fat fractions below 10%. This being said, several solid cancers have a significant fat fraction which might benefit from R_{1f} measurement. Notably, Agarwal *et al.* measured mean fat fractions in breast cancer at 17% [93], Martin *et al.* measured average lymphoma fat fraction of 26±12.2% [94], and Sun *et al.* measured average fat fraction of lymphnode metastases of esophageal cancer at 17% [95]. Furthermore, case studies by Skorpi *et al.* and Yasuda *et al.* measure high fat fractions in liposarcomas (11-21%) [96] and pancreatic carcinomas (27.44%) [97] respectively. And outside of applications in cancer, Fat DESPOT is also a promising tool for investigating hypoxia's role in fatty liver disease where fat fractions are often above 5% and can reach up to 30% [98].

This being said both Fat DESPOT approaches discussed in this thesis likely have acceptable R_{1w} precision and R_{1w} measurements could be used in isolation or conjunction with R_{1f} for tumors with lower fat fractions, expanding the scope of possible imaging sites. To truly assess Fat DESPOT's ability to capture oxygen-induced changes in R_{1w}, R_{1f}, and R_2*, gas challenge pilot measurements should be conducted in these areas of interest. Due to their simple immobilization, range of fat fractions, and the recorded link between hypoxia and treatment outcomes for these cancers, prostate and head and neck cancers would be ideal initial candidates.

Chapter 5

Conclusion

5.1 Summary

This thesis compared the conventional magnitude-based Fat DESPOT$_m$ with the complex Fat DESPOT$_c$ approach, assessing them as multiparametric mapping tools and for their potential applicability to MR oximetry. Though both Fat DESPOT techniques have potential in these areas, the higher precision and accuracy of Fat DESPOT$_c$ paired with shorter acquisition times increase the possible applications of this approach.

In simulations, Fat DESPOT$_c$ was shown to have a greater resistance to differences in the initial phase of fat and water. Fat DESPOT$_m$ and Fat DESPOT$_c$ were compared in two simulated scenarios. In the first, the initial phases of the fat and water signal components shared a single phase. In the second, fat and water were given separate phases, based on

values obtained in experiments. While Fat DESPOT$_m$ had an overall higher precision and accuracy in the first scenario, this approach was strongly affected by a phase difference, demonstrating large error and standard deviation at intermediate fat fraction ranges. The complex model, which has separate parameters for the fat and water initial phases improved in precision when a phase difference was introduced.

In phantom experiments, Fat DESPOT$_c$ had a smaller average standard deviation for all parameters except R_2^*, though this difference had a minimal impact on the subsequent power analysis. Fat DESPOT also had a lower average error in PDFF. Comparison of R_2^*, R_{1f} and R_{1w} to literature was not straightforward, but both Fat DESPOT approaches were self-consistent and agreed with some published reports. The lower precision of Fat DESPOT$_m$ compared to Fat DESPOT$_c$ may have been due to phase differences, as suggested by simulations. This is further supported by lower R^2 values for Fat DESPOT$_m$, especially for intermediate fat fractions.

In vivo, both approaches to Fat DESPOT generally agreed with published values of PDFF, R_2^*, R_{1f}, and R_{1w}, while Fat DESPOT$_c$ once again tended to have smaller standard deviations. However, comparison to literature was once again made difficult by the lack of anatomy-specific data and measurements of fat-water separated R_1.

5.2 Future Work

While Fat DESPOT$_c$ shows potential for multiparametric and hypoxia mapping, as mentioned in the discussion sections of the manuscript, additional experiments could be beneficial for a more direct comparison to existing literature. Namely, deploying both Fat DESPOT approaches in the liver would allow for comparison to a wider body of quantitative MRI work. Furthermore, repeated in vivo measurements combined with acceleration techniques could help assess the repeatability of both approaches in feasible acquisition times.

Results from GC showed that initial phases of fat and water are not identical. This raises questions on the Fat DESPOT$_m$ assumption that the initial phase of fat and water can be modeled by a single parameter and the effect of this assumption on the Fat DESPOT$_m$ output estimates. Indeed, simulations suggested that the Fat DESPOT$_m$ model is susceptible to error when a phase difference is introduced. Including separate initial phases for fat and water may increase the accuracy of Fat DESPOT$_m$, though fitting an additional parameter may also affect the stability of the fit. Nonetheless, further developing and optimizing Fat DESPOT$_m$ has the potential to increase precision and accuracy and should be investigated.

Finally, the true test of the Fat DESPOT approaches for MR oximetry is to use these approaches in a gas challenge in healthy participants or patients, assessing the sensitivity and reliability with which they detect changes in oxygenation. These measurements could also be paired in point measurements using a polarographic probe in animal studies, comparing the

change detected with MR to the true change in oxygenation. As proposed in the Discussion chapter, cancers of the prostate and of the head and neck would be ideal initial assessment sites.

Chapter 6

Appendices

6.1 Appendix 1: Phantom construction

A phantom was constructed to compare the accuracy of the magnitude Fat DESPOT compared to the complex Fat DESPOT approaches in experimental data. Two iterations of the phantom were constructed, each containing seven 50 ml vials of agar-based fat-water emulsions. These were created following a modified version of the methodology outlined by Bush *et al.* [99].

To prepare the agar-water solution, 9.0 g of agar powder (MilliporeSigma Canada Ltd) was added to 300 ml of distilled water in a 1L beaker, set on a hot plate at approximately 300 °C with a stir bar set to approximately 1000 rpm. Then, 0.3 g of sodium benzoate (MilliporeSigma Canada Ltd), a preservative, was added to the solution to increase the

phantom's longevity. Finally, 0.6 mL of Polyethylene glycol sorbitan monolaurate (Tween 20, MilliporeSigma Canada Ltd) was added as a surfactant to improve the stability of the oil-water emulsion. In the first iteration of the phantom, x ml of a 20 mM Gadobutrol (Gadovist, Bayer Healthcare) solution was added to increase the relaxation rate of water. In the first iteration of the phantom, the final gadobutrol concentration was 1.5 mM; however, this led to very high values of R_{1w}. Hence, in the second iteration of the phantom, the final concentration of gadobutrol was selected to be 0.2 mM. The solution was covered to reduce evaporation and increase the heating rate until it had exceeded 80°C and the agar powder had completely dissolved.

To prepare the oil solution, 300 mL of peanut oil (JVF Canada inc) was placed in a 1 L beaker, and heated to approximately 300°C with a stir bar set to approximately 1000 rpm, as with the water. 2 mL of sorbitane monooleate (Span 80 MilliporeSigma Canada Ltd) was added as a surfactant. The solution was mixed and heated for a minimum of 10 minutes or until it exceeded 80°C.

In the first iteration of the phantom, a single hot plate was used, such that oil and water solutions had to be interchanged to maintain equivalent temperatures. In the second iteration of the phantom, two hotplates were used, such that oil and water solutions could be warmed simultaneously. This made for more consistent temperatures, leading to higher success rates for emulsions and extending the range of possible PDFFs.

For each fat fraction, 100 ml of solution was prepared. Using an electric pipette, the water

fraction was first added to a 500 mL beaker with a stir bar. This solution was maintained at a temperature between 70°C and 90°C to ensure the agar remained liquid while preventing evaporation with the stir-bar set to approximately 1000 rpm. The temperature-matched oil fraction was then slowly added to the water using an electric pipette, ensuring that the fat was incorporated progressively into the water. The solution was then mixed for 5 min, regularly monitoring the temperature to maintain it in the acceptable range.

The emulsion was then slowly decanted into a 50 mL polypropylene centrifuge tube (Corning® 50 mL centrifuge tubes). To remove any remaining bubbles, the tubes were tapped on the bench top. Any remaining space was filled with additional emulsion to avoid large air bubbles at the top of the phantom. In the first iteration of the phantom, two vials were filled with a gadobutrol-water solution at two different concentrations to create 100% water fractions with different relaxation times, while in the second version of the phantom, the agar-water solution was used for this purpose. Nominal fat fractions for each phantom iteration are given in table 6.1.

Tubes were suspended on a plastic and polystyrene rig placed in a cylindrical acrylic container (Magphan ®SMR170, The Phantom Laboratories, Salem, USA). The container was filled with a solution of water, sodium chloride (Windsor Salt Ltd) ([NaCl]=24 mM) to reduce B0 field inhomogeneity, and gadobutrol ([Gd^+]=0.3 mM). Between uses, the phantom was stored in a 4°C refrigerator and returned to room temperature before measurements.

Iteration	1	2
Vial	Nominal Fat Fraction (%)	
1	0	0
2	6	5
3	25	25
4	50	50
5	60	60
6	0	75
7	100	100

Table 6.1: Nominal fat fraction of the 1^{st} and 2^{nd} iterations of the variable fat fraction phantom.

6.2 Appendix 2: Refining the complex approach to Fat DESPOT

Three versions of the complex approach to Fat DESPOT were evaluated during this thesis. The final version is presented in the manuscript presented in Chapter 3.

Our group previously modified the magnitude Fat DESPOT model to create a complex model [3,25]. In the first version of Fat DESPOT$_c$ model was used with the same processing steps as Fat DESPOT$_m$ outlined in In preprocessing, a relative B1 map was generated to

correct FAs in the Fat DESPOT fit. Initial guesses were then calculated for PDFF, T_1, and R_2^*. To obtain initial guesses of PDFF, a 3-point Dixon fat-water separation was then accomplished on the first three echoes of the dataset from the smallest echo. An R_2^* map was then calculated using the monoexponential fit to the even echoes with the smallest FA. Data from the 3° FA acquisitions was then processed through a non-linear DESPOT1 with B_1 correction to obtain a joint fat and water R_1 estimate, $R_{1,global}$. This was used as an initial guess for the dominant species in each via, based on the initial estimate of the PDFFl. The complex Fat DESPOT model outlined in equation 2.27 was then fit to the data. Initial guesses of ΔB_0 were obtained from the 3-point DIXON while the initial guess of Φ_0 was 0 rad.

With this initial version of Fat DESPOT$_c$, fitting the entire phantom was not possible, as solutions were not reached in some areas of the phantom water compartment. Assessing the emulsion tubes only showed a high degree of inhomogeneity and poor goodness of fit in some areas (Figure 6.3, column 1). Quantitative analysis showed large standard deviations, a large number of outlier voxels, and inconsistent trends in R_2^*, R_{1f}, and R_{1w}. The distribution of multiparametric estimates for this and subsequent s of the Fat DESPOT$_c$ approach is displayed in Figure 6.4.

A second version of the Fat DESPOT approach was developed after the initial assessment of results, modifying the processing pipeline. Given the susceptibility of 3-point DIXON fat-water separation to fat-water swaps, the graph cuts (GC) fat-water separation algorithm [82],

using all FAs and echoes, was incorporated into the complex workflow to provide initial guesses for PDFF. The GC algorithm returns a separated complex signal for fat and water, R_2^* maps, and ΔB_0. The PDFF was obtained from the magnitude of the fat-water separated complex signals as well as the initial phase of the fat, water, and combined initial phase. These initial guesses were used in the complex Fat DESPOT model for signal fitting using equation 2.27.

While goodness of fit and homogeneity within the tubes was improved using the GC initial guesses, multiparametric maps of the second version of Fat DESPOT$_c$ (Figure 6.3, column 2) revealed reduced goodness of fit at the intermediate fat fractions and areas of very poor fitting in the water compartment that corresponded to artifacts in the R_2^* and R_{1w} maps. Though dwarfed by the outlier values of the first version of Fat DESPOT$_c$, the quantitative assessment of multiparametric estimates revealed once again irregular trends in the R_{1w} compartment, which was markedly lower for intermediate fat fractions compared to the higher or lower extremes, and a much lower value of R_{1w} at 5% nominal fat fraction compared to the other fat fractions.

Following this assessment of the second version of the fitting method and given the additional information available from the GC algorithm, a third version of the Fat DESPOT$_c$ approach was developed, modifying the signal model itself. This new model included separate parameters for fat and water Φ_0, reflecting experimental results showing that initial phases were different. Example maps of the phase of fat and water, obtained from the GC output

of their respective complex signal components. are displayed in Figure 6.1. ΔB_0 obtained from GC also revealed that in some measurements, the value of ΔB_0 changed between FAs. An example of these ΔB_0 maps is presented in Figure 6.2. An angle specific ΔB_0, $\Delta B_{0\theta}$ was therefore included in the updated fat DESPOT model. These observations resulted in a modified complex Fat DESPOT model, equation 6.1. For fitting, initial guesses for PDFF, R_2^*, ϕ_{0f}, and ϕ_{0w} were obtained from GC. $B_{0\theta}$ was also obtained from a GC fitting of mGRE data from each FA and used as a fixed parameter in the Fat DESPOT equation. $R_{1global}$ estimates were obtained from the DESPOT$_1$ fitting, as in the original processing pipeline, and attributed to either R_{1f} or R_{1w} according to which signal component was dominant according to the PDFF estimate.

$$S_{meas}(TE,TR,\alpha) = S_0\left[(1-f)We^{-i\Phi_{0W}} + fF\sum_{n=1}^{N} A_n e^{-i\Delta w_n TE}e^{-i\Phi_{0f}}\right]e^{R_2^* TE}e^{-i(2\pi\gamma\Delta B_0 TE)} \tag{6.1}$$

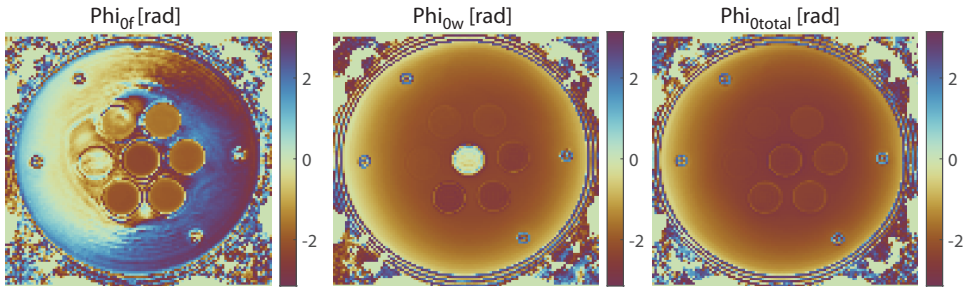

Figure 6.1: Example of fat, water, and total signal initial phase maps, calculated from the complex fat-water separated signal obtained using the GC algorithm. Fat and water initial phases are noticeably different. All images are displayed with perceptually uniform colour maps from the crameri library [4, 5]

The third version of Fat DESPOT$_c$ returned smooth multiparametric maps (Figure 6.3, column 2), though minor artifacts remained in the R_{1w} and R_2* maps, in the water compartment. These artifacts have been discussed previously in the phantom and in vivo results section of Chapter 3 of this thesis. The goodness of fit was high in all tubes. Furthermore, in quantitative analysis, standard deviations were on par or smaller than previous versions, and trends appeared consistent throughout the ROIs. This version of the Fat DESPOT$_c$ approach was selected for comparison to Fat DESPOT$_m$ in the work presented in Chapter 3 of this thesis.

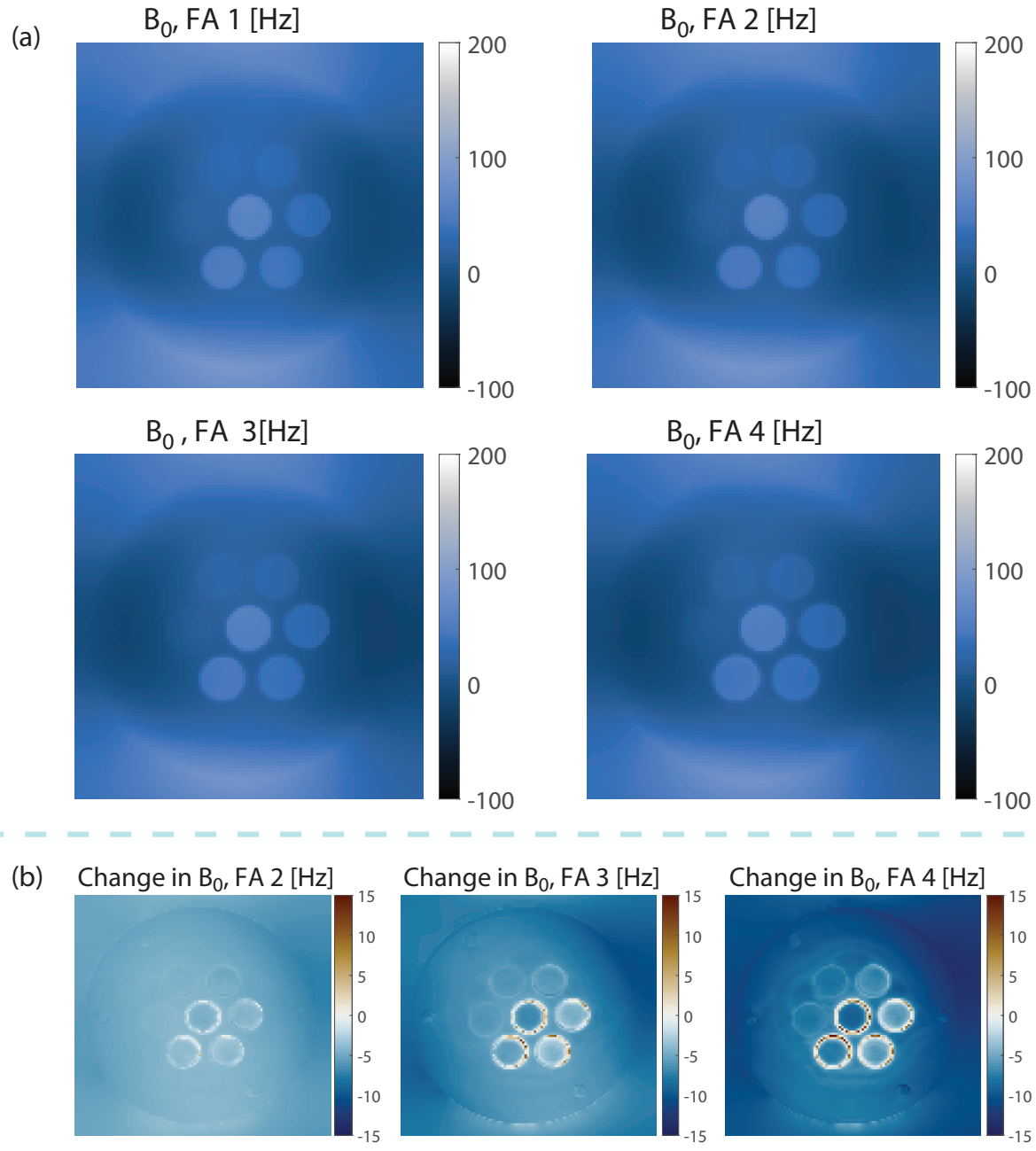

Figure 6.2: (a) Examples of the FA-specific B_0 maps obtained by applying the GC algorithm to an mGRE acquisition of the multi-variable fat fraction phantom and (b) difference B_0 maps taken between the second, third, and fourth FA acquisitions with respect to the first FA. All images are displayed with perceptually uniform colour maps from the crameri library [4, 5]

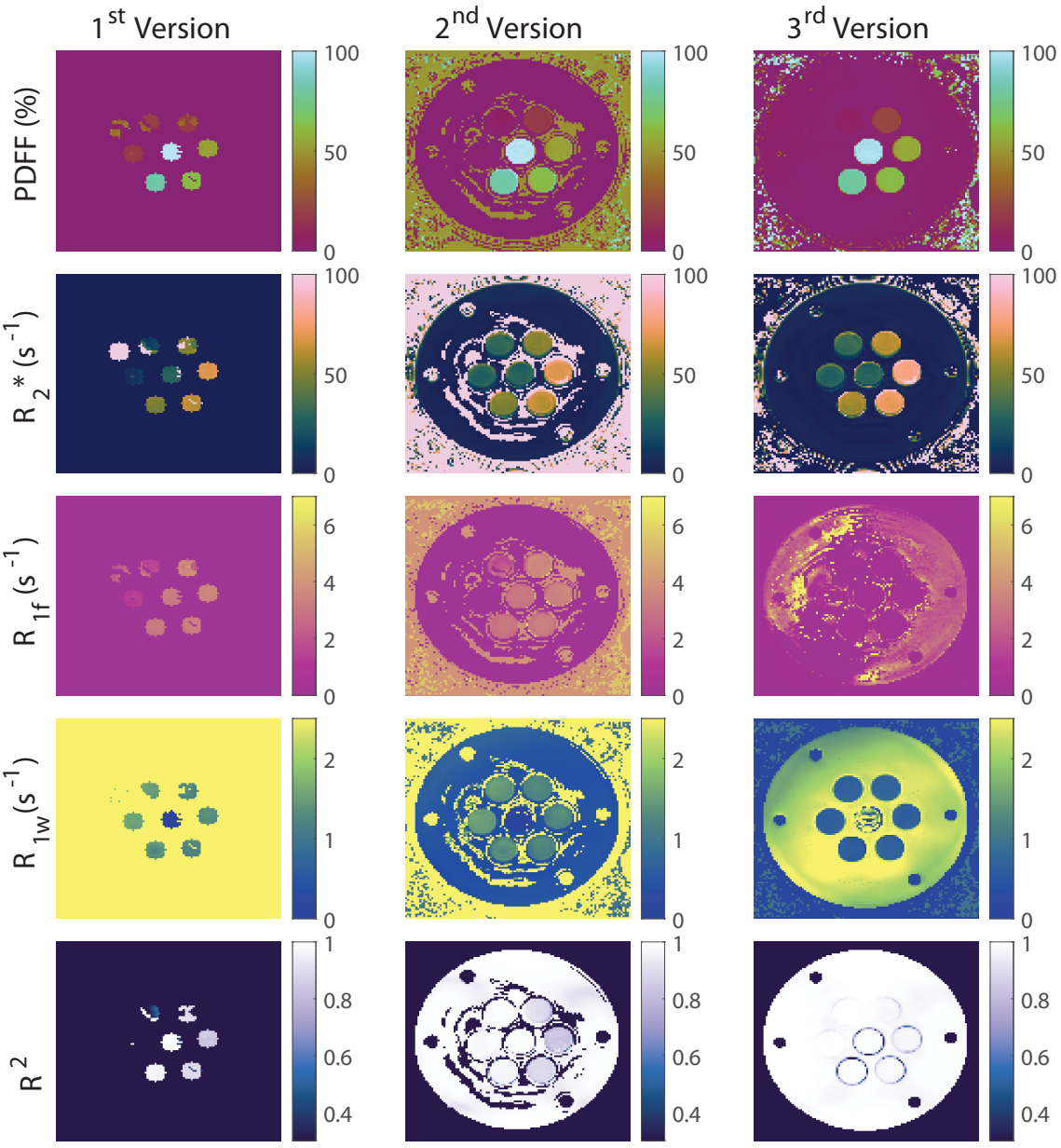

Figure 6.3: Multiparametric maps of the variable fat fraction phantom using the three versions of the Fat DESPOT$_c$ approach. The 1^{st} version is masked to show only the manually selected ROIs, as a poor fit was observed in some of the water compartments. All images are displayed with perceptually uniform colour maps from the crameri library [4, 5]

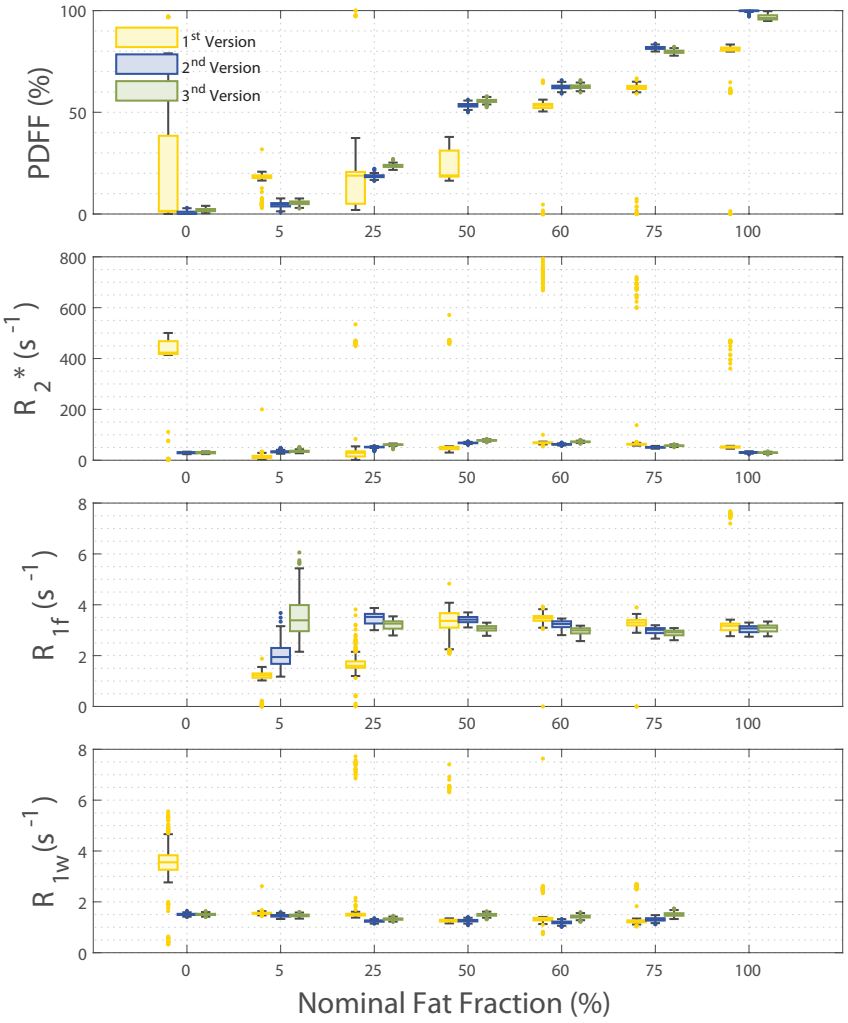

Figure 6.4: Distribution of voxel-wise estimates of PDFF, R_2^*, R_{1f}, and R_{1w} in the variable fat fraction phantom using the three versions of the Fat DESPOT$_c$ approach.

6.3 Appendix 3: Further work in accelerating acquisitions

All results presented in this thesis use 8 NSA in each mGRE acquisition and a VFA approach with four FAs. Signal averaging increases the SNR [44]; however, Fat DESPOT has been reported to achieve good fits with SNR > 63 [25]. Hence, the NSA could likely be reduced. A series of mGRE acquisitions were collected following the sequence parameters for Fat DESPOT$_c$ displayed in table 3.3, but with 1 NSA, and processed in the same way as the 8 NSA data. Each acquisition took 5.15 minutes, as opposed to the 8 NSA acquisition which took 51 min.

Chen *et al.* have suggested that using three FAs rather than 4 in VFA approaches to T_1 mapping is the most efficient for accuracy and precision [89]. FA reduction was also used in our group's previous Fat DESPOT work [25]. Retrospective fitting of our data was therefore conducted using the 1st, 3rd, and 4th FA for the 8 NSA and 1 NSA acquisitions for the Fat DESPOT$_c$ approach, nominally reducing the acquisition time by 25%.

The change in NSA and FA seemed to bias R_1 results, but precision is not affected (Figure 6.5). The stable precision suggests that using these acceleration techniques with Fat DESPOT may be appropriate for MR hypoxia mapping, where the change in R_1 may be more relevant than the actual value of R_1. VFA angle optimization aims at maximizing precision rather than accuracy and the bias in the 3 FA results compared to the 4 FA results was

likely due to the impact of FA selection on the accuracy of R_1 estimates [89]. However, the bias in the 1 NSA acquisition compared to the 8 NSA acquisition remains an open question.

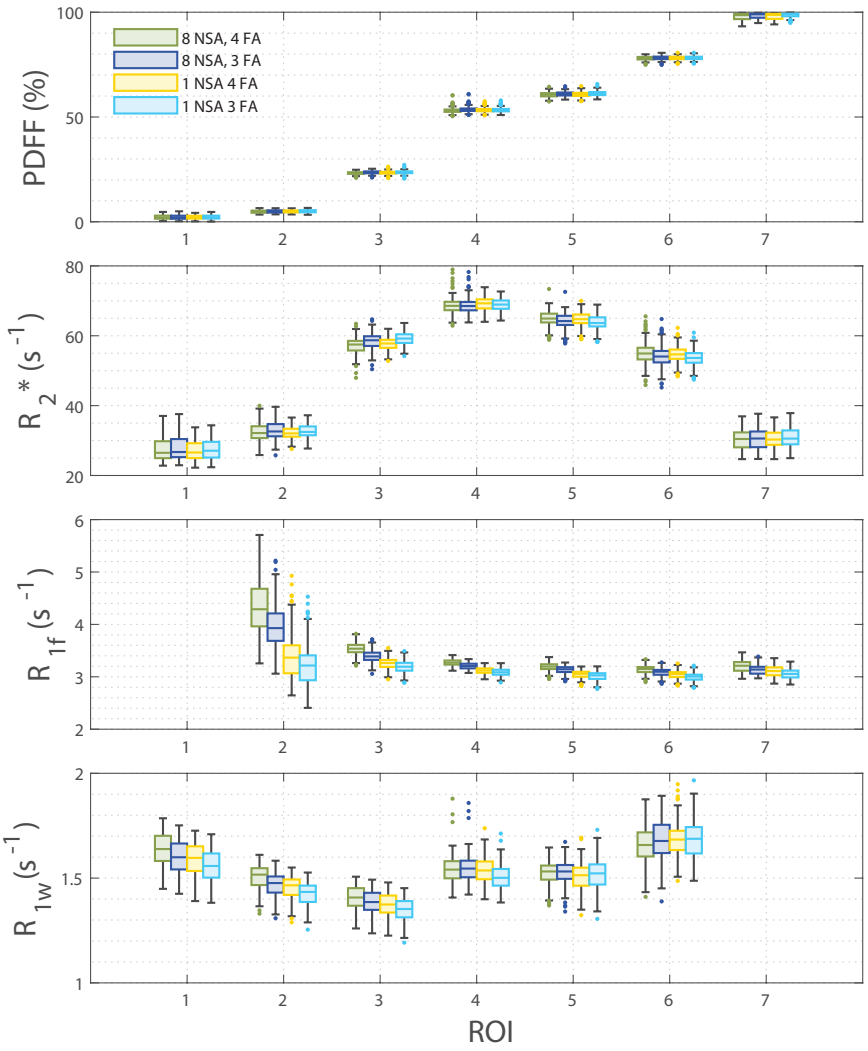

Figure 6.5: Distribution of voxel-wise estimates of PDFF, R_2^*, R1f, and R_{1w} from the Fat DESPOT$_c$ approach using 8 NSA and 4 FA, using 8 NSA and 3 FAs (FA 1, 3, 4), using 1 NSA 4 FA, and using 1 NSA and 3 FA (FA 1, 3, 4).

Bibliography

[1] M. H. Ahmed, M. S. Ghatge, and M. K. Safo, "Hemoglobin: structure, function and allostery," *Sub-cellular biochemistry*, vol. 94, pp. 345–382, 2020.

[2] I. R. Levesque, "Nuclear Magnetic Resonance," 2022. (PDF document). MDPH 607. McGill University.

[3] C. Ciobanu, "Evaluation of complex fitting for longitudinal relaxation mapping in fat with magnetic resonance imaging," 2022. Publisher: McGill University.

[4] C. Green, "Crameri perceptually uniform scientific colormaps," 2022.

[5] F. Crameri, "Geodynamic diagnostics, scientific visualisation and StagLab 3.0," *Geoscientific Model Development*, vol. 11, pp. 2541–2562, June 2018. Publisher: Copernicus GmbH.

[6] M. Pavlides, R. Banerjee, J. Sellwood, C. J. Kelly, M. D. Robson, J. C. Booth, J. Collier, S. Neubauer, and E. Barnes, "Multiparametric magnetic resonance imaging predicts clinical outcomes in patients with chronic liver disease," *Journal of Hepatology*, vol. 64, pp. 308–315, Feb. 2016.

[7] Q. Wan, H. Peng, J. Lyu, F. Liu, C. Chuanli, Y. Qiao, J. Deng, H. Zheng, Y. Wang, C. Zou, and X. Liu, "Water Specific MRI T1 Mapping for Evaluating Liver Inflammation

Activity Grades in Rats With Methionine-Choline-Deficient Diet-Induced Nonalcoholic Fatty Liver Disease," *Journal of Magnetic Resonance Imaging*, vol. 56, Feb. 2022.

[8] S.-B. Catrina and X. Zheng, "Hypoxia and hypoxia-inducible factors in diabetes and its complications," *Diabetologia*, vol. 64, pp. 709–716, Apr. 2021.

[9] P. Vaupel and A. Mayer, "Hypoxia in cancer: significance and impact on clinical outcome," *Cancer and Metastasis Reviews*, vol. 26, pp. 225–239, June 2007.

[10] X. Sun, G. Niu, N. Chan, B. Shen, and X. Chen, "Tumor Hypoxia Imaging," *Molecular Imaging and Biology*, vol. 13, pp. 399–410, June 2011.

[11] J. C. Walsh, A. Lebedev, E. Aten, K. Madsen, L. Marciano, and H. C. Kolb, "The Clinical Importance of Assessing Tumor Hypoxia: Relationship of Tumor Hypoxia to Prognosis and Therapeutic Opportunities," *Antioxidants & Redox Signaling*, vol. 21, pp. 1516–1554, Oct. 2014.

[12] J. M. Brown, "Tumor Hypoxia in Cancer Therapy," in *Methods in Enzymology*, vol. 435 of *Oxygen Biology and Hypoxia*, pp. 295–321, Academic Press, Jan. 2007.

[13] D. R. Collingridge, W. K. Young, B. Vojnovic, P. Wardman, E. M. Lynch, S. A. Hill, and D. J. Chaplin, "Measurement of Tumor Oxygenation: A Comparison between Polarographic Needle Electrodes and a Time-Resolved Luminescence-Based Optical Sensor," *Radiation Research*, vol. 147, pp. 329–334, Mar. 1997.

[14] M. W. Dewhirst and S. R. Birer, "Oxygen-Enhanced MRI Is a Major Advance in Tumor Hypoxia Imaging," *Cancer Research*, vol. 76, pp. 769–772, Feb. 2016.

[15] K. R. Thulborn, J. C. Waterton, P. M. Matthews, and G. K. Radda, "Oxygenation dependence of the transverse relaxation time of water protons in whole blood at high field," *Biochimica et Biophysica Acta (BBA) - General Subjects*, vol. 714, pp. 265–270, Feb. 1982.

[16] Y. Ohno and H. Hatabu, "Basics concepts and clinical applications of oxygen-enhanced MR imaging," *European Journal of Radiology*, vol. 64, pp. 320–328, Dec. 2007.

[17] R. R. Hallac, H. Zhou, R. Pidikiti, K. Song, S. Stojadinovic, D. Zhao, T. Solberg, P. Peschke, and R. P. Mason, "Correlations of noninvasive BOLD and TOLD MRI with pO2 and relevance to tumor radiation response," *Magnetic Resonance in Medicine*, vol. 71, no. 5, pp. 1863–1873, 2014. _eprint: https://onlinelibrary.wiley.com/doi/pdf/10.1002/mrm.24846.

[18] T. J. Arai, D. M. Yang, J. W. Campbell, T. Chiu, X. Cheng, S. Stojadinovic, P. Peschke, and R. P. Mason, "Oxygen-Sensitive MRI: A Predictive Imaging Biomarker for Tumor Radiation Response?," *International journal of radiation oncology, biology, physics*, vol. 110, pp. 1519–1529, Aug. 2021.

[19] E. Bluemke, A. Bertrand, K.-Y. Chu, N. Syed, A. G. Murchison, R. Cooke, T. Greenhalgh, B. Burns, M. Craig, N. Taylor, K. Shah, F. Gleeson, and D. Bulte,

"Using Variable Flip Angle (VFA) and Modified Look-Locker Inversion Recovery (MOLLI) T1 mapping in clinical OE-MRI," *Magnetic Resonance Imaging*, vol. 89, pp. 92–99, June 2022.

[20] D. M. Yang, T. J. Arai, J. W. Campbell, J. L. Gerberich, H. Zhou, and R. P. Mason, "Oxygen-Sensitive MRI Assessment of Tumor Response to Hypoxic Gas Breathing Challenge," *NMR in biomedicine*, vol. 32, p. e4101, July 2019.

[21] E. K. Englund and M. C. Langham, "Quantitative and Dynamic MRI Measures of Peripheral Vascular Function," *Frontiers in Physiology*, vol. 11, 2020.

[22] B. F. Jordan, J. Magat, F. Colliez, E. Ozel, A.-C. Fruytier, V. Marchand, L. Mignion, C. Bouzin, P. D. Cabi, C. Vandeputte, O. Feron, N. Delzenne, U. Himmelreich, V. Denolin, T. Duprez, and B. Gallez, "Mapping Hypoxia in Renal Carcinoma with Oxygen-enhanced MRI: Comparison with Intrinsic Susceptibility MRI and Pathology | Radiology," *Magnetic Resonance in Medicine*, vol. 70, no. 3, pp. 732–744, 2012.

[23] F. Colliez, M.-A. Neveu, J. Magat, T. T. Cao Pham, B. Gallez, and B. F. Jordan, "Qualification of a Noninvasive Magnetic Resonance Imaging Biomarker to Assess Tumor Oxygenation," *Clinical Cancer Research*, vol. 20, pp. 5403–5411, Oct. 2014.

[24] F. Franconi, L. Lemaire, H. Saint-Jalmes, and P. Saulnier, "Tissue oxygenation mapping by combined chemical shift and T1 magnetic resonance imaging,"

Magnetic Resonance in Medicine, vol. 79, no. 4, pp. 1981–1991, 2018. _eprint: https://onlinelibrary.wiley.com/doi/pdf/10.1002/mrm.26857.

[25] V. Fortier and I. R. Levesque, "MR-oximetry with fat DESPOT," *Magnetic Resonance Imaging*, vol. 97, pp. 112–121, Apr. 2023.

[26] C. Le Ster, G. Gambarota, J. Lasbleiz, R. Guillin, O. Decaux, and H. Saint-Jalmes, "Breath-hold MR measurements of fat fraction, T1, and T2* of water and fat in vertebral bone marrow," *Journal of Magnetic Resonance Imaging*, vol. 44, no. 3, pp. 549–555, 2016. _eprint: https://onlinelibrary.wiley.com/doi/pdf/10.1002/jmri.25205.

[27] C. Paternostro, E. David, E. Novo, and M. Parola, "Hypoxia, angiogenesis and liver fibrogenesis in the progression of chronic liver diseases," *World Journal of Gastroenterology : WJG*, vol. 16, pp. 281–288, Jan. 2010.

[28] K.-U. Eckardt, C. Rosenberger, J. S. Jürgensen, and M. S. Wiesener, "Role of Hypoxia in the Pathogenesis of Renal Disease," *Blood Purification*, vol. 21, pp. 253–257, June 2003.

[29] R. Lall, R. Mohammed, and U. Ojha, "Full article: What are the links between hypoxia and Alzheimer's disease?," *Neuropsychiatric disease and treatment*, pp. 1343–1354, 2019.

[30] S. Cannito, C. Paternostro, C. Busletta, C. Bocca, S. Colombatto, A. Miglietta, E. Novo, and M. Parola, "Hypoxia, hypoxia-inducible factors and fibrogenesis in chronic liver diseases," *Histology and Histopathology*, no. 29, pp. 33–44, 2013.

[31] R. Chaudhry, J. H. Miao, and A. Rehman, "Physiology, Cardiovascular," in *StatPearls*, Treasure Island (FL): StatPearls Publishing, 2024.

[32] R. N. Pittman, "The Circulatory System and Oxygen Transport," in *Regulation of Tissue Oxygenation*, Morgan & Claypool Life Sciences, 2011.

[33] A. S. Popel, "Theory of Oxygen Transport to Tissue," *Critical reviews in biomedical engineering*, vol. 17, no. 3, pp. 257–321, 1989.

[34] B. S. Sørensen and M. R. Horsman, "Tumor Hypoxia: Impact on Radiation Therapy and Molecular Pathways," *Frontiers in Oncology*, vol. 10, 2020.

[35] J. C. Forster, W. M. Harriss-Phillips, M. J. Douglass, and E. Bezak, "A review of the development of tumor vasculature and its effects on the tumor microenvironment," *Hypoxia*, vol. 5, pp. 21–32, Apr. 2017. Publisher: Dove Medical Press _eprint: https://www.tandfonline.com/doi/pdf/10.2147/HP.S133231.

[36] M. C. Brahimi-Horn, J. Chiche, and J. Pouysségur, "Hypoxia and cancer," *Journal of Molecular Medicine*, vol. 85, pp. 1301–1307, Dec. 2007.

[37] J. A. Nagy, S.-H. Chang, S.-C. Shih, A. M. Dvorak, and H. F. Dvorak, "Heterogeneity of the Tumor Vasculature," *Seminars in Thrombosis and Hemostasis*, vol. 36, pp. 321–331, Apr. 2010.

[38] J. Zhou, T. Schmid, S. Schnitzer, and B. Brüne, "Tumor hypoxia and cancer progression," *Cancer Letters*, vol. 237, pp. 10–21, June 2006.

[39] H. Doktorova, J. Hrabeta, M. A. Khalil, and T. Eckschlager, "Hypoxia-induced chemoresistance in cancer cells: The role of not only HIF-1," *Biomedical Papers*, vol. 159, pp. 166–177, June 2015.

[40] R. C. Perez, D. Kim, A. W. P. Maxwell, and J. C. Camacho, "Functional Imaging of Hypoxia: PET and MRI," *Cancers*, vol. 15, p. 3336, Jan. 2023. Number: 13 Publisher: Multidisciplinary Digital Publishing Institute.

[41] P. Bonnitcha, S. Grieve, and G. Figtree, "Clinical imaging of hypoxia: Current status and future directions," *Free Radical Biology and Medicine*, vol. 126, pp. 296–312, Oct. 2018.

[42] J. R. Brender, Y. Saida, N. Devasahayam, M. C. Krishna, and S. Kishimoto, "Hypoxia Imaging As a Guide for Hypoxia-Modulated and Hypoxia-Activated Therapy," *Antioxidants & Redox Signaling*, vol. 36, pp. 144–159, Jan. 2022. Publisher: Mary Ann Liebert, Inc., publishers.

[43] Z.-P. Liang and P. C. Lauterbur, *Principles of Magnetic Resonance Imaging: A Signal Processing Perspective | IEEE eBooks | IEEE Xplore*. Wiley-IEEE Press, 2000.

[44] D. G. Nishimura, *Principles of Magnetic Resonance Imaging*. Stanford, Califoria, USA: Standford University, 1 ed., 1996.

[45] E. Tiesinga, P. J. Mohr, D. B. Newell, and B. Taylor, N, "The 2022 CODATA Recommended Values of the Fundamental Physical Constants," *(Web Version 9.0). Database developed by J. Baker, M. Douma, and S. Kotochigova. Available at https://physics.nist.gov/constants, National Institute of Standards and Technology, Gaithersburg, MD 20899*, 2024.

[46] R. Hu, D. Kleimaier, M. Malzacher, M. A. Hoesl, N. K. Paschke, and L. R. Schad, "X-nuclei imaging: Current state, technical challenges, and future directions," *Journal of Magnetic Resonance Imaging*, vol. 51, no. 2, pp. 355–376, 2020. _eprint: https://onlinelibrary.wiley.com/doi/pdf/10.1002/jmri.26780.

[47] B. A. Jung and M. Weigel, "Spin echo magnetic resonance imaging," *Journal of Magnetic Resonance Imaging*, vol. 37, no. 4, pp. 805–817, 2013. _eprint: https://onlinelibrary.wiley.com/doi/pdf/10.1002/jmri.24068.

[48] K. L. Wright, J. I. Hamilton, M. A. Griswold, V. Gulani, and N. Seiberlich, "Non-Cartesian parallel imaging reconstruction," *Journal of Magnetic*

Resonance Imaging, vol. 40, no. 5, pp. 1022–1040, 2014. _eprint: https://onlinelibrary.wiley.com/doi/pdf/10.1002/jmri.24521.

[49] R. W. Brown, Y.-C. N. Cheng, E. M. Haacke, M. R. Thompson, and R. Venkatesan, *Magnetic Resonance Imaging: Physical Principles and Sequence Design*. John Wiley & Sons, June 2014. Google-Books-ID: Z45SAwAAQBAJ.

[50] N. Stikov, M. Boudreau, I. R. Levesque, C. L. Tardif, J. K. Barral, and G. B. Pike, "On the accuracy of T1 mapping: Searching for common ground," *Magnetic Resonance in Medicine*, vol. 73, no. 2, pp. 514–522, 2015. _eprint: https://onlinelibrary.wiley.com/doi/pdf/10.1002/mrm.25135.

[51] N. Jin, J. S. Da Silveira, M.-P. Jolly, D. N. Firmin, G. Mathew, N. Lamba, S. Subramanian, D. J. Pennell, S. V. Raman, and O. P. Simonetti, "Free-breathing myocardial T2* mapping using GRE-EPI and automatic Non-rigid motion correction," *Journal of Cardiovascular Magnetic Resonance*, vol. 17, p. 113, Jan. 2015.

[52] G. Zaharchuk, A. J. Martin, G. Rosenthal, G. T. Manley, and W. P. Dillon, "Measurement of cerebrospinal fluid oxygen partial pressure in humans using MRI," *Magnetic Resonance in Medicine*, vol. 54, no. 1, pp. 113–121, 2005. _eprint: https://onlinelibrary.wiley.com/doi/pdf/10.1002/mrm.20546.

[53] J. D. Winter, M. Estrada, and H.-L. M. Cheng, "Normal Tissue Quantitative T1 and T2 MRI Relaxation Time Responses to Hypercapnic and Hyperoxic Gases," *Academic Radiology*, vol. 18, pp. 1159–1167, Sept. 2011.

[54] G. B. Chavhan, P. S. Babyn, B. Thomas, M. M. Shroff, and E. M. Haacke, "Principles, Techniques, and Applications of T2*-based MR Imaging and Its Special Applications," *Radiographics*, vol. 29, pp. 1433–1449, Sept. 2009.

[55] O. Bane, C. Besa, M. Wagner, N. Oesingmann, H. Zhu, M. I. Fiel, and B. Taouli, "Feasibility and reproducibility of BOLD and TOLD measurements in the liver with oxygen and carbogen gas challenge in healthy volunteers and patients with hepatocellular carcinoma," *Journal of Magnetic Resonance Imaging*, vol. 43, no. 4, pp. 866–876, 2016. _eprint: https://onlinelibrary.wiley.com/doi/pdf/10.1002/jmri.25051.

[56] D. A. White, Z. Zhang, L. Li, J. Gerberich, S. Stojadinovic, P. Peschke, and R. P. Mason, "Developing Oxygen-Enhanced Magnetic Resonance Imaging as a Prognostic Biomarker of Radiation Response," *Cancer letters*, vol. 380, pp. 69–77, Sept. 2016.

[57] H. Zhou, S. Chiguru, R. R. Hallac, D. Yang, G. Hao, P. Peschke, and R. P. Mason, "Examining correlations of oxygen sensitive MRI (BOLD/TOLD) with [18F]FMISO PET in rat prostate tumors," *American Journal of Nuclear Medicine and Molecular Imaging*, vol. 9, pp. 156–167, Apr. 2019.

[58] D. Zhao, J. Pacheco-Torres, R. R. Hallac, D. White, P. Peschke, S. Cerdán, and R. P. Mason, "Dynamic Oxygen Challenge Evaluated by NMR T1 and T2* – insights into tumor oxygenation," *NMR in biomedicine*, vol. 28, pp. 937–947, Aug. 2015.

[59] B. Haddock, H. B. W. Larsson, A. E. Hansen, and E. Rostrup, "Measurement of brain oxygenation changes using dynamic T1-weighted imaging," *NeuroImage*, vol. 78, pp. 7–15, Sept. 2013.

[60] D. M. McGrath, J. H. Naish, J. P. B. O'Connor, C. E. Hutchinson, J. C. Waterton, C. J. Taylor, and G. J. M. Parker, "Oxygen-induced changes in longitudinal relaxation times in skeletal muscle," *Magnetic Resonance Imaging*, vol. 26, pp. 221–227, Feb. 2008.

[61] J. P. O'Connor, A. Jackson, G. A. Buonaccorsi, D. L. Buckley, C. Roberts, Y. Watson, S. Cheung, D. M. McGrath, J. H. Naish, C. J. Rose, P. M. Dark, G. C. Jayson, and G. J. Parker, "Organ-specific effects of oxygen and carbogen gas inhalation on tissue longitudinal relaxation times," *Magnetic Resonance in Medicine*, vol. 58, no. 3, pp. 490–496, 2007. _eprint: https://onlinelibrary.wiley.com/doi/pdf/10.1002/mrm.21357.

[62] A. Salem, R. A. Little, A. Latif, A. K. Featherstone, M. Babur, I. Peset, S. Cheung, Y. Watson, V. Tessyman, H. Mistry, G. Ashton, C. Behan, J. C. Matthews, M.-C. Asselin, R. G. Bristow, A. Jackson, G. J. M. Parker, C. Faivre-Finn, K. J. Williams, and J. P. B. O'Connor, "Oxygen-enhanced MRI Is Feasible, Repeatable, and Detects Radiotherapy-induced Change in Hypoxia in Xenograft Models and in Patients with

Non–small Cell Lung Cancer | Clinical Cancer Research | American Association for Cancer Research," *Clinical Cance*, vol. 23, no. 13, pp. 3811–3829, 2019.

[63] J. P. B. O'Connor, J. H. Naish, G. J. M. Parker, J. C. Waterton, Y. Watson, G. C. Jayson, G. A. Buonaccorsi, S. Cheung, D. L. Buckley, D. M. McGrath, C. M. L. West, S. E. Davidson, C. Roberts, S. J. Mills, C. L. Mitchell, L. Hope, N. C. Ton, and A. Jackson, "Preliminary Study of Oxygen-Enhanced Longitudinal Relaxation in MRI: A Potential Novel Biomarker of Oxygenation Changes in Solid Tumors," *International Journal of Radiation Oncology*Biology*Physics*, vol. 75, pp. 1209–1215, Nov. 2009.

[64] A. McCabe, S. Martin, S. Rowe, J. Shah, P. S. Morgan, D. Borys, and R. Panek, "Oxygen-enhanced MRI assessment of tumour hypoxia in head and neck cancer is feasible and well tolerated in the clinical setting," *European Radiology Experimental*, vol. 8, p. 27, Mar. 2024.

[65] M. J. Dubec, D. L. Buckley, M. Berks, A. Clough, J. Gaffney, A. Datta, D. J. McHugh, N. Porta, R. A. Little, S. Cheung, C. Hague, C. L. Eccles, P. J. Hoskin, R. G. Bristow, J. C. Matthews, M. van Herk, A. Choudhury, G. J. M. Parker, A. McPartlin, and J. P. B. O'Connor, "First-in-human technique translation of oxygen-enhanced MRI to an MR Linac system in patients with head and neck cancer," *Radiotherapy and Oncology*, vol. 183, p. 109592, June 2023.

[66] J. S. Burrell, S. Walker-Samuel, L. C. Baker, J. K. Boult, Y. Jamin, J. Halliday, J. C. Waterton, and S. P. Robinson, "Exploring R2* and R1 as imaging biomarkers of tumor oxygenation," *Journal of Magnetic Resonance Imaging*, vol. 38, no. 2, pp. 429–434, 2013. _eprint: https://onlinelibrary.wiley.com/doi/pdf/10.1002/jmri.23987.

[67] R. A. Little, Y. Jamin, J. K. R. Boult, J. H. Naish, Y. Watson, S. Cheung, K. F. Holliday, H. Lu, D. J. McHugh, J. Irlam, C. M. L. West, G. N. Betts, G. Ashton, A. R. Reynolds, S. Maddineni, N. W. Clarke, G. J. M. Parker, J. C. Waterton, S. P. Robinson, and J. P. B. O'Connor, "Mapping Hypoxia in Renal Carcinoma with Oxygen-enhanced MRI: Comparison with Intrinsic Susceptibility MRI and Pathology," *Radiology*, vol. 288, pp. 739–747, Sept. 2018. Publisher: Radiological Society of North America.

[68] S. C. Beeman, Y.-B. Shui, C. J. Perez-Torres, J. A. Engelbach, J. J. H. Ackerman, and J. R. Garbow, "O2-sensitive MRI distinguishes brain tumor versus radiation necrosis in murine models," *Magnetic Resonance in Medicine*, vol. 75, no. 6, pp. 2442–2447, 2016. _eprint: https://onlinelibrary.wiley.com/doi/pdf/10.1002/mrm.25821.

[69] E. Bluemke, D. Bulte, A. Bertrand, B. George, R. Cooke, K.-Y. Chu, L. Durrant, V. Goh, C. Jacobs, S. M. Ng, V. Y. Strauss, M. A. Hawkins, and R. Muirhead, "Oxygen-enhanced MRI MOLLI T1 mapping during chemoradiotherapy in anal squamous cell carcinoma," *Clinical and Translational Radiation Oncology*, vol. 22, pp. 44–49, May 2020.

[70] E. Bluemke, A. Bertrand, K.-Y. Chu, N. Syed, A. G. Murchison, R. Cooke, T. Greenhalgh, B. Burns, M. Craig, N. Taylor, K. Shah, F. Gleeson, and D. Bulte, "Oxygen-enhanced MRI and radiotherapy in patients with oropharyngeal squamous cell carcinoma," *Clinical and Translational Radiation Oncology*, vol. 39, p. 100563, Mar. 2023.

[71] L. Jiang, P. T. Weatherall, R. W. McColl, D. Tripathy, and R. P. Mason, "Blood oxygenation level-dependent (BOLD) contrast magnetic resonance imaging (MRI) for prediction of breast cancer chemotherapy response: A pilot study," *Journal of Magnetic Resonance Imaging*, vol. 37, no. 5, pp. 1083–1092, 2013. _eprint: https://onlinelibrary.wiley.com/doi/pdf/10.1002/jmri.23891.

[72] A. Belfatto, D. A. White, R. P. Mason, Z. Zhang, S. Stojadinovic, G. Baroni, and P. Cerveri, "Tumor radio-sensitivity assessment by means of volume data and magnetic resonance indices measured on prostate tumor bearing rats," *Medical Physics*, vol. 43, pp. 1275–1284, Mar. 2016.

[73] J. Zhong, M. Kobus, P. Maitre, A. Datta, C. Eccles, M. Dubec, D. McHugh, D. Buckley, A. Scarsbrook, P. Hoskin, A. Henry, and A. Choudhury, "MRI-guided Pelvic Radiation Therapy: A Primer for Radiologists," *RadioGraphics*, vol. 43, p. e230052, Nov. 2023. Publisher: Radiological Society of North America.

[74] H. F. Bennett, H. M. Swartz, R. D. I. Brown, and S. H. Koenig, "Modification of Relaxation of Lipid Protons by Molecular Oxygen and Nitroxides," *Investigative Radiology*, vol. 22, p. 502, June 1987.

[75] F. Del Grande, F. Santini, D. A. Herzka, M. R. Aro, C. W. Dean, G. E. Gold, and J. A. Carrino, "Fat-Suppression Techniques for 3-T MR Imaging of the Musculoskeletal System," *Radiographics : a review publication of the Radiological Society of North America, Inc*, vol. 34, no. 1, pp. 217–233, 2014.

[76] E. M. Delfaut, J. Beltran, G. Johnson, J. Rousseau, X. Marchandise, and A. Cotten, "Fat Suppression in MR Imaging: Techniques and Pitfalls," *RadioGraphics*, vol. 19, pp. 373–382, Mar. 1999.

[77] D. C. Karampinos, H. Yu, A. Shimakawa, T. M. Link, and S. Majumdar, "Chemical shift-based water/fat separation in the presence of susceptibility-induced fat resonance shift," *Magnetic Resonance in Medicine*, vol. 68, no. 5, pp. 1495–1505, 2012. _eprint: https://onlinelibrary.wiley.com/doi/pdf/10.1002/mrm.24157.

[78] S. B. Reeder, A. R. Pineda, Z. Wen, A. Shimakawa, H. Yu, J. H. Brittain, G. E. Gold, C. H. Beaulieu, and N. J. Pelc, "Iterative decomposition of water and fat with echo asymmetry and least-squares estimation (IDEAL): Application with fast spin-echo imaging," *Magnetic Resonance in Medicine*, vol. 54, no. 3, pp. 636–644, 2005. _eprint: https://onlinelibrary.wiley.com/doi/pdf/10.1002/mrm.20624.

[79] J. Berglund, L. Johansson, H. Ahlström, and J. Kullberg, "Three-point dixon method enables whole-body water and fat imaging of obese subjects," *Magnetic Resonance in Medicine*, vol. 63, no. 6, pp. 1659–1668, 2010. _eprint: https://onlinelibrary.wiley.com/doi/pdf/10.1002/mrm.22385.

[80] J. Ma, "Dixon techniques for water and fat imaging," *Journal of Magnetic Resonance Imaging*, vol. 28, no. 3, pp. 543–558, 2008. _eprint: https://onlinelibrary.wiley.com/doi/pdf/10.1002/jmri.21492.

[81] D. Hernando, P. Kellman, J. P. Haldar, and Z.-P. Liang, "Robust water/fat separation in the presence of large field inhomogeneities using a graph cut algorithm," *Magnetic Resonance in Medicine*, vol. 63, no. 1, pp. 79–90, 2010. _eprint: https://onlinelibrary.wiley.com/doi/pdf/10.1002/mrm.22177.

[82] D. Hernando, C. D. G. Hines, H. Yu, and S. Reeder, "Addressing phase errors in fat-water imaging using a mixed magnitude/complex fitting method," *Magnetic Resonance in Medicine*, vol. 67, no. 3, pp. 638–644, 2012. _eprint: https://onlinelibrary.wiley.com/doi/pdf/10.1002/mrm.23044.

[83] A. K. Featherstone, J. P. O'Connor, R. A. Little, Y. Watson, S. Cheung, M. Babur, K. J. Williams, J. C. Matthews, and G. J. Parker, "Data-driven mapping of hypoxia-related tumor heterogeneity using DCE-MRI and OE-MRI,"

Magnetic Resonance in Medicine, vol. 79, no. 4, pp. 2236–2245, 2018. _eprint: https://onlinelibrary.wiley.com/doi/pdf/10.1002/mrm.26860.

[84] M. Hendriks and S. K. Ramasamy, "Blood Vessels and Vascular Niches in Bone Development and Physiological Remodeling," *Frontiers in Cell and Developmental Biology*, vol. 8, p. 602278, Nov. 2020.

[85] T. Kirchgesner, X. Demondion, M. Stoenoiu, P. Durez, A. Nzeusseu Toukap, F. Houssiau, C. Galant, S. Acid, F. Lecouvet, J. Malghem, and B. Vande Berg, "Fasciae of the musculoskeletal system: normal anatomy and MR patterns of involvement in autoimmune diseases," *Insights into Imaging*, vol. 9, pp. 761–771, Oct. 2018. Number: 5 Publisher: SpringerOpen.

[86] Y. Ding, R. P. Mason, R. W. McColl, Q. Yuan, R. R. Hallac, R. D. Sims, and P. T. Weatherall, "Simultaneous measurement of tissue oxygen level-dependent (TOLD) and blood oxygenation level-dependent (BOLD) effects in abdominal tissue oxygenation level studies," *Journal of Magnetic Resonance Imaging*, vol. 38, no. 5, pp. 1230–1236, 2013. _eprint: https://onlinelibrary.wiley.com/doi/pdf/10.1002/jmri.24006.

[87] F. C. Moreton, K. A. Dani, C. Goutcher, K. O'Hare, and K. W. Muir, "Respiratory challenge MRI: Practical aspects," *NeuroImage : Clinical*, vol. 11, pp. 667–677, May 2016.

[88] A. Deshmane, V. Gulani, M. A. Griswold, and N. Seiberlich, "Parallel MR imaging," *Journal of Magnetic Resonance Imaging*, vol. 36, no. 1, pp. 55–72, 2012. _eprint: https://onlinelibrary.wiley.com/doi/pdf/10.1002/jmri.23639.

[89] H.-L. M. Cheng and G. A. Wright, "Rapid high-resolution T1 mapping by variable flip angles: Accurate and precise measurements in the presence of radiofrequency field inhomogeneity," *Magnetic Resonance in Medicine*, vol. 55, no. 3, pp. 566–574, 2006. _eprint: https://onlinelibrary.wiley.com/doi/pdf/10.1002/mrm.20791.

[90] M. Boudreau, C. L. Tardif, N. Stikov, J. G. Sled, W. Lee, and G. B. Pike, "B1 mapping for bias-correction in quantitative T1 imaging of the brain at 3T using standard pulse sequences," *Journal of Magnetic Resonance Imaging*, vol. 46, no. 6, pp. 1673–1682, 2017. _eprint: https://onlinelibrary.wiley.com/doi/pdf/10.1002/jmri.25692.

[91] S. Volz, U. Nöth, A. Rotarska-Jagiela, and R. Deichmann, "A fast B1-mapping method for the correction and normalization of magnetization transfer ratio maps at 3 T," *NeuroImage*, vol. 49, pp. 3015–3026, Feb. 2010.

[92] J. L. Kent, I. Dragonu, L. Valkovič, and A. T. Hess, "Rapid 3D absolute B1+ mapping using a sandwiched train presaturated TurboFLASH sequence at 7 T for the brain and heart," *Magnetic Resonance in Medicine*, vol. 89, no. 3, pp. 964–976, 2023. _eprint: https://onlinelibrary.wiley.com/doi/pdf/10.1002/mrm.29497.

[93] K. Agarwal, U. Sharma, S. Mathur, V. Seenu, R. Parshad, and N. R. Jagannathan, "Study of lipid metabolism by estimating the fat fraction in different breast tissues and in various breast tumor sub-types by in vivo 1H MR spectroscopy," *Magnetic Resonance Imaging*, vol. 49, pp. 116–122, June 2018.

[94] S. S. Martin, R. Czwikla, J. L. Wichmann, M. H. Albrecht, L. Lenga, R. H. Savage, C. Arendt, R. Hammerstingl, T. J. Vogl, and B. Kaltenbach, "Dual-energy CT-based iodine quantification to differentiate abdominal malignant lymphoma from lymph node metastasis," *European Journal of Radiology*, vol. 105, pp. 255–260, Aug. 2018.

[95] X. Sun, S. Ozawa, J. Endo, and J. Hashimoto, "Detecting lymph node metastasis of esophageal cancer on dual-energy computed tomography - Xuyang Sun, Tetsu Niwa, Soji Ozawa, Jun Endo, Jun Hashimoto, 2022," *Acta Radiologica*, vol. 63, no. 1, pp. 3–10, 2022.

[96] M. Skorpil, H. Rydén, J. Wejde, E. Lidbrink, O. Brosjö, and J. Berglund, "The effect of radiotherapy on fat content and fatty acids in myxoid liposarcomas quantified by MRI," *Magnetic Resonance Imaging*, vol. 43, pp. 37–41, Nov. 2017.

[97] M. Yasuda and W. R. Bloor, "Lipid Content of Tumors," *Journal of Clinical Investigation*, vol. 11, pp. 677–682, July 1932.

[98] H. S. Leitão, C. Paulino, D. Rodrigues, S. I. Gonçalves, C. Marques, M. Carvalheiro, C. F. Geraldes, and F. Caseiro-Alves, "MR Fat Fraction Mapping," *Academic Radiology*, vol. 20, pp. 957–961, Aug. 2013.

[99] E. C. Bush, A. Gifford, C. L. Coolbaugh, T. F. Towse, B. M. Damon, and E. B. Welch, "Fat-Water Phantoms for Magnetic Resonance Imaging Validation: A Flexible and Scalable Protocol," *Journal of Visualized Experiments : JoVE*, p. 57704, Sept. 2018.